DEVELOPMENT AND CHARACTERIZATION OF EFFICIENT PLASMA ACTUATORS

By

PENGFEI ZHAO

A DISSERTATION PRESENTED TO THE GRADUATE SCHOOL
OF THE UNIVERSITY OF FLORIDA IN PARTIAL FULFILLMENT
OF THE REQUIREMENTS FOR THE DEGREE OF
DOCTOR OF PHILOSOPHY

UNIVERSITY OF FLORIDA

2015

To my Mom, parents in law and my wife, for all the trust and support on me

ACKNOWLEDGMENTS

First and foremost, I would like to thank to my supervisor and committee chair, Dr. Subrata Roy for providing me a precious opportunity to do my graduate research in Applied Physics Research Group (APRG) over last five years. His willingness to motivate me contributed tremendously to this project. I also would like to thank him for his abundantly help and invaluable assistance, support and guidance.

Then, I am thankful to all my committee members for their support. I deeply appreciate the opportunity to work and consult with them. Specially, I would like to thank Dr. Lawrence Ukeiley for his help on the PIV analysis and Dr. Robert Moore for his help and kindness.

Furthermore, I also would like to thank colleagues in APRG for their helpful discussion and kindness during past years. Thank you, Dr. Ankush Bhatia, Ariel Blanco, Arnob Das Gupta, Moses Divaker, Dr. Ryan Durshcer, Tomas Houba, Dr. Navya Mastanaiah, Sherlie Portugal, Dr. Mark Riherd and Dr. Chin-Cheng Wang.

Lastly, I would like to thank my family. I would like to thank my mom, Peixian Liu, and my parents in law, Xinxia Shi and Jianxin Lu, for all the love and support they gave me. I would like to thank my wife, Lu Lu, for her love, trust and support behind this work.

TABLE OF CONTENTS

page

LIST OF TABLES

LIST OF FIGURES

LIST OF ABBREVIATIONS

CPU	Central Processing Unit
DBD	Dielectric Barrier Discharge
DC / AC	Direct Current / Alternating Current
eV	Electronvolt (unit of energy, equal to 1.6×10^{-19} J)
HV	High Voltage
IC	Integrated Circuit
IR	Infrared
LED	Light-Emitting Diode
LTE	Local Thermodynamic (or Thermal) Equilibrium
PIV	Particle Image Velocimetry

Abstract of Dissertation Presented to the Graduate School
of the University of Florida in Partial Fulfillment of the
Requirements for the Degree of Doctor of Philosophy

DEVELOPMENT AND CHARACTERIZATION OF EFFICIENT PLASMA ACTUATORS

By

Pengfei Zhao

December 2015

Chair: Subrata Roy
Major: Aerospace Engineering

The objective of presented work is to conduct an in depth study for efficient low power plasma actuators for various applications. Needle corona discharge within a channel electrodes configuration was employed to design the efficient low power plasma actuators. Compared to traditional dielectric barrier discharge (DBD) plasma actuators, corona discharge based efficient plasma actuators can increase the energy conversion efficiency from 0.7% to 2.8 %.

Studies on flow structure and power consumption have been done by analyzing data from PIV and electrical parameter measurement. Investigation on the input signals with different voltage and polarity shows an influence on the actuators, with positive polarity yielding better energy conversion efficiency. Then the mechanism of this influence is also studied through comparing velocity profiles between cases with different polarity. Capabilities of efficient cooling and vortices generation have also been observed.

Furthermore, parameters of needle actuator configuration, including needle height, tip size and number of needles, were investigated on its surface cooling performance. A Glauert-like wall jet is generated by the needle-plate actuator to

enhance the forced convection on the hot surface. The wall jet velocity increases with the increasing voltage and/or the decreasing radius of curvature. And the needle location also plays an important role in the flow generation. Vortices can also be generated with two or more needle actuators promoting mixing of air near a surface.

CHAPTER 1
INTRODUCTION

Atmospheric plasma driven active flow control devices have been extensively studied in recent years. Applications of these devices range from the control of the laminar to turbulent transition (Riherd & Roy, 2013) to the drag reduction (Jukes, 2007). The advantages of dielectric barrier discharge (DBD) driven plasma actuators include lack of moving parts, fast response, small scale, surface compliance, and ease of construction and application. Major disadvantage of these devices is that their energy conversion efficiencies are extremely low, only one tenth of a percent (Moreau, 2007; Riherd & Roy, 2012). This is because of a large amount of energy loss in light emission as well as heating of both dielectric material and plasma. Also the momentum injection to the neighboring flow is largely limited due to high viscous losses encountered in traditional DBD wall jets. As compared to DBD, direct current (DC) corona discharge only generates minimal glow near the surface of powered electrode without using any dielectric material. Thus, the energy loss mentioned above can be avoided. However, the energy conversion efficiencies of DC corona devices remain less than 1% (Colas, Ferret, Pai, Lacoste, & Laux, 2010; Moreau, 2007). This is again due to excessive viscous loss from the thin wall shear layer or/and discharge loss near the wire surface. In contrast, the channel configuration (Campbell & Roy, 2014) with needle electrode can be employed to minimize the ionization loss and the viscous loss from flow induced by plasma body force.

Typically, atmospheric DC corona discharge devices consist of a powered electrode and a grounding electrode separated by air. The powered electrode usually has a sharp tip or round edge with a minute radius of curvature. The grounding

electrode often has a large smooth surface. Application of high-voltage DC signal to the powered electrode forms a surface corona discharge around the sharp tip or the round edge where the maximum electric field is generated. The grounding electrode is placed some distance away to generate desired electric field to induce the ions formed by impact ionization. Then, collisional momentum transfer between ions and neutral particles occurs in the space between the electrodes. Both positive and negative DC voltages can be used to induce flow with slightly different mechanisms (Moreau, 2007). For the positive corona, ionization region is generated by anode electron avalanche near the electrode. Then, the Coulomb force repels positive ions toward the cathode. In the case of negative corona, negative ions are created by electron attachment and then repelled toward the anode.

This study experimentally explores a class of DC corona needle actuation devices that has been developed to generate moderate directed airflow with extremely low power consumption, and thus improving the energy conversion efficiency by an order of magnitude than its DBD counterpart. Particular electrode arrangements for these devices showed great benefits for cooling and vortex generation applications.

The goal of this study is to exploring the capability of corona discharge plasma actuators and their performance on different conditions. The contents of this document can be broken into several sections.

In chapter 2, fundamental concepts of plasma actuators including definition and classification are discussed. The desired type of plasma actuators is specified and compared with others. Furthermore, comprehensive physical characteristics on corona

discharge plasma and electric wind induced by corona discharge based actuators are described.

Experimental investigation is conducted to analyze the performance of the needle actuation devices under many different conditions in chapter 3. Electrical properties and velocity field of the airflow induced are obtained from the experiment. Results are presented demonstrating huge increase in energy conversion efficiency.

In chapter 4 and 5, experimental analyses on applications of needle actuation devices are addressed. The surface cooling performance and vortices generation using newly designed actuators will be investigated.

Finally, a summary of highlights in this the study is presented in chapter 6, along with the recommendations for the future work.

CHAPTER 2
PHYSICS OF EFFICIENT PLASMA ACTUATORS

An actuator, by definition, is a type of motor that is responsible for moving or controlling a mechanism or system. Particularly, actuators mentioned in this work are referring to the devices which can move the working gas fluid in desired manor. Generally, researchers develop these actuators to manipulate flow to affect desired change in thermal and/or fluid systems. For example, efficient actuators could modify the laminar–turbulent transition (Riherd & Roy, 2012) inside the boundary layer to reduce the drag and to enhance the lift of airfoils. Also these actuators could be used to adding or removing heat flux from any surface (Go, Maturana, Fisher, & Garimella, 2008). This is of large technological importance for industries where thermal and/or fluid system are involved, and more specifically for mechanical and aerospace engineering.

Among all the actuation methods, a new and original technology using non-thermal plasmas is in full expansion. Indeed, although mechanical devices may be effective, they have many drawbacks. In particular, they are complicated, add significant amount of weight, have volume and are sources of noise and vibration. Moreover, they are composed of mechanical parts that wear away and that may break down. Consequently, plasma actuators are now in full expansion because they do not exhibit all these drawbacks.

The main advantage of plasma actuator is that it directly converts electric energy into kinetic energy without involving moving mechanical parts. Thus it may be considered to be a very simple MEMS. Secondly, its response time is very short and enables a real-time control at high frequency.

This chapter reviews the research status of the plasma actuators. The emphasis in this chapter is on the definition, classification and physical description of the plasma actuators, especially ones with corona discharge.

2.1 Plasma Actuators

Generally, the plasma actuator is composed of at least two electrodes mounted near the wall between which a high voltage is applied, resulting in a non-thermal plasma region. In most of the cases, plasma actuators can generate the discharge-induced gas flow jet to modify the properties of boundary layer and then to actively manipulate the airflow. The gas flow jet induced by discharged gas in electric field also can be called as electric wind. Figure 2-1 shows a manipulated airflow along a flat plate with a plasma actuator.

In this section, definition and classification of plasma actuators will be described and discussed. Different types of plasma actuators will be compared. Then, this comparison will be used to design more efficient plasma actuators.

2.1.1 Definition of Plasma Actuators

The plasma actuators discussed in this section refer to the plasma-based devices. Such devices can generate secondary airflow, usually called electric wind or ionic wind, in atmospheric condition. In order to induce the secondary airflow in ambient air, plasma actuators should create both an atmospheric pressure plasma and a strong electric field through the plasma region. Usually, plasma is also generated by the strong electric field. Consequently, all charge particles inside plasma will be accelerated by the strong electric field. This process can also be described as the effect of body force, which can be expressed approximately as:

$$\vec{F} = q\vec{E}, \tag{2-1}$$

where $\vec{E}$ is the electric field generated by plasma actuators and q represents the net total charge of the particles in the electric field $\vec{E}$. Then, due to the collision between neutral particles and accelerated charged particles, momentum will be transferred from fast-moving charged particles to slow-moving neutral particles. In the momentum transfer process, since the mass of electrons can be neglected in comparison with ions, the acceleration time of electrons is much shorter than that of ions which is at least 2000 times heavier. Thus, majority momentum gained by neutral particles comes from ions, both positive and negative. Eventually, airflow generated consists of both neutral particles and charged particles at approximately the same velocity.

2.1.2 Classification of Plasma Actuators

Generally, the plasma actuators work in atmospheric condition because most application needs this. Thus, classification is done on this kind of actuators. Many different types of plasma actuators working in atmospheric pressure condition have been developed and tested in past years. These actuators can be classified by their discharge mechanism and geometry design. Based on discharge physics, plasma actuators can be divided into three groups, DBD plasma actuator, corona plasma actuator and other plasma actuator. In each group, plasma discharge along with electrical body force can be generated near the surface or in space depending on the geometry design of these actuators.

According to the statement above, the majority of plasma actuators studied is based on atmospheric pressure plasma. Over the past few decades, atmospheric pressure plasmas have been studied for numerous industrial applications such as

ozone generation, pollutant removal and surface treatment. Several papers and books give a complete review of this type of discharge (J. Reece Roth, 1995; Schutze et al., 1998). Due to the density of air at atmospheric pressure, the atmospheric pressure plasma is non-thermal, which means that the ion temperature is not as high as the electron temperature. These non-thermal plasmas may be produced by a variety of electrical discharges and have very low energy cost in comparison to thermal plasma. This is due to the fact that the majority of the input electrical energy goes into the production of energetic electrons, instead of heating the surrounding gas.

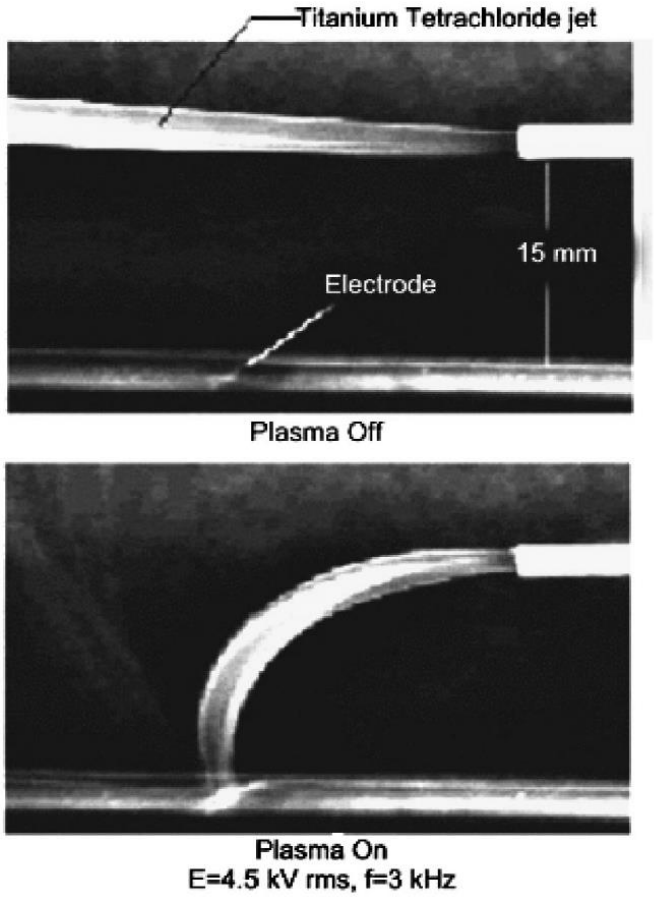

Figure 2-1. Titanium dioxide smoke jet illustrates that paraelectric neutral gas flow is induced by a low pressure region associated a DBD plasma actuator (J. R. Roth, 2003).

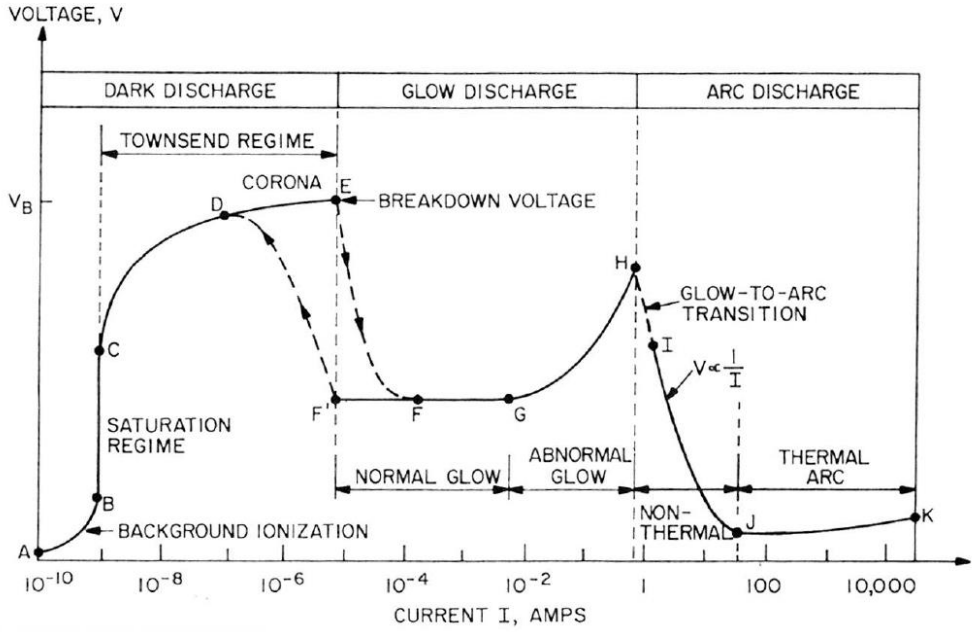

Figure 2-2. Voltage and current characteristic for a DC discharge in a low pressure discharge tube. Taken from(J. Reece Roth, 1995).

Generally, the gas discharge may be classified into three main types based on delivered current: dark discharge, glow discharge, and arc discharge. Figure 2-2 displays the three regimes in a DC voltage-current (VI) plot. The dark discharge, also called Townsend discharge, is characterized by very little light emission. In this regime, the electron generated from other source (cosmic ray or photoionization, (Howatson, 1976)) is accelerated by the electric field. For a constant electric field, the energetic electron can ionize neutral particles to multiple the electron number density. This phenomenon is called electron avalanche (Raizer, 1991). Thus, the discharge is self-sustained through electron avalanche. After the current starts to increase, the breakdown of the gas occurs. During this process, some neutral particles get excited by the energetic electrons and emits photons. Thus, the plasma starts to become luminous. The breakdown voltage of the gas is found to have a function of the ambient

working gas pressure (p) and discharge gap (d) according to Paschen's law. The breakdown voltage, V_B, of a working gas can be calculated by (A. A. Fridman, 2008)

$$V_B = \frac{B(pd)}{\ln(pd) + C}, C = \ln\frac{A}{\ln(1/\gamma + 1)}. \quad (2\text{-}2)$$

where A and B are gas dependent constants and γ is the secondary electron coefficient for the cathode. Table 2-1 provides A and B values for air.

Table 2-1. Coeffiecents, *A* and *B*, used to calculate the breakdown voltage of air based on Paschen's Law (A. A. Fridman, 2008).

Gas	$A\ (\frac{1}{cm\ Torr})$	$B\ (\frac{1}{cm\ Torr})$
Air	15	365

After this breakdown happens, the plasma is said to enter the glow discharge regime. In this regime, positive ions also gain a high speed towards cathode. When the heavy ions collide with cathode, it can give electrons on the cathode surface enough energy to escape. This phenomenon is called secondary electron emission, which is the primarily sustaining mechanism for the glow discharge (Howatson, 1976). If the current through plasma is allowed to increase furthermore, the glow-to-arc transition eventually occurs with a significant drop in voltage. The voltage drop is due to the reduction in resistance inside the plasma region. Generally, hot cathode and hot plasma are accompanied with high current arc discharge. These phenomena consume large amount of energy and may also causes damage.

Briefly, the formation of steady discharge under atmospheric pressure is mainly based on the electron avalanche or secondary electron emission. The discharge mechanisms used for plasma actuators are usually atmospheric pressure corona discharges (dark discharge) and dielectric barrier discharges (special form of glow

discharge). Their characteristics are typically as follows: high voltage of a few kV to several tens of kV with DC or AC excitation, with a frequency from 50 Hz to 50 kHz (only for AC or pulsed DC), electrical current from a few nA to a few mA. In these conditions, the density of charged species is between 10^9 and 10^{13} cm^{-3} and the electron temperature is a few eV.

The first studies of plasma actuators generating airflow by electrical discharges dealt with DC corona discharges. For example, it is demonstrated that the transition point on a flat plate could be changed by the application of an electric field (Velkoff & Godfrey, 1979; Velkoff & Ketcham, 1968). In this application, the plasma actuator with four wire electrodes is placed above the surface of a flat plate and powered with HV DC signal. No grounded electrode is used in this application. Thereafter, corona discharges are widely implemented into many different plasma actuators for different applications.

There are two main advantages of the corona discharge based plasma actuators. First, DC input signal maintains a constant strong electric field to accelerate charged particles. Second, very small amount of power is needed to maintain the corona discharge. On the other hand, its disadvantage is the corona-to-arc transition when current is high.

In order to prevent corona-to-arc transition, a dielectric barrier can be placed in the discharge gap, which stops the electric current between electrodes and prevents arc discharge formation. Such discharge is called DBD. Because of the charge accumulation on the dielectric barrier, HV DC signal cannot be used to generate plasma. Then DBDs are usually excited by AC or pulsed DC signals, with frequencies between 50 Hz and 500 kHz (A. Fridman, Chirokov, & Gutsol, 2005). The plasma is

generated in the electrode gap with consecutive micro-discharges. These micro-discharges, also called streamers, are distributed in time and space in a random manner. Generally, these streamers have a diameter of about 100μm and a lifetime of a few nanoseconds (with velocity of these streamers in the range of 10^7–10^8 ms^{-1}).

In the middle of the 1990s, Roth's group developed a novel glow discharge actuator working at atmospheric pressure. It was a surface DBD actuator. This kind of actuator consists of at least two electrodes mounted asymmetrically on the two sides of a dielectric plate. It is shown that a secondary airflow of several ms^{-1} tangentially to the wall is driven by the discharge. Meanwhile, when the applied voltage reaches 30 kV_{pp}, the reaction force of the airflow can be as high as 11 mN. It is also demonstrate that this secondary airflow can modify the boundary layer of the free stream, with a drag modification as the result. After this original work, DBD based plasma actuators are extensively studied. The main advantage of DBD based plasma actuators is that they can generate strong steady glow discharge. Its disadvantages include joule heating in plasma (Tirumala et al., 2014) and saturation effect (Durscher, Stanfield, & Roy, 2012).

For both corona discharge and DBD mechanism, electrodes configuration can be designed to generate surface plasma or volumetric plasma. For example, Figure 2-3 shows different corona discharge plasma actuators examined in literatures. Actuators displayed in Figure 2-3A - 2-3D generate volumetric plasma between electrodes while surface plasma sheet are created by actuators in Figure 2-3E - 2-3H. The airflow generated by volumetric and surface plasma source shows different characteristics. Since airflow induced by surface plasma actuators are close to the surface, viscous shear stress will play an important role in this kind of configuration. On the other hand,

both volumetric and surface plasma actuators are designed according to the needs of applications.

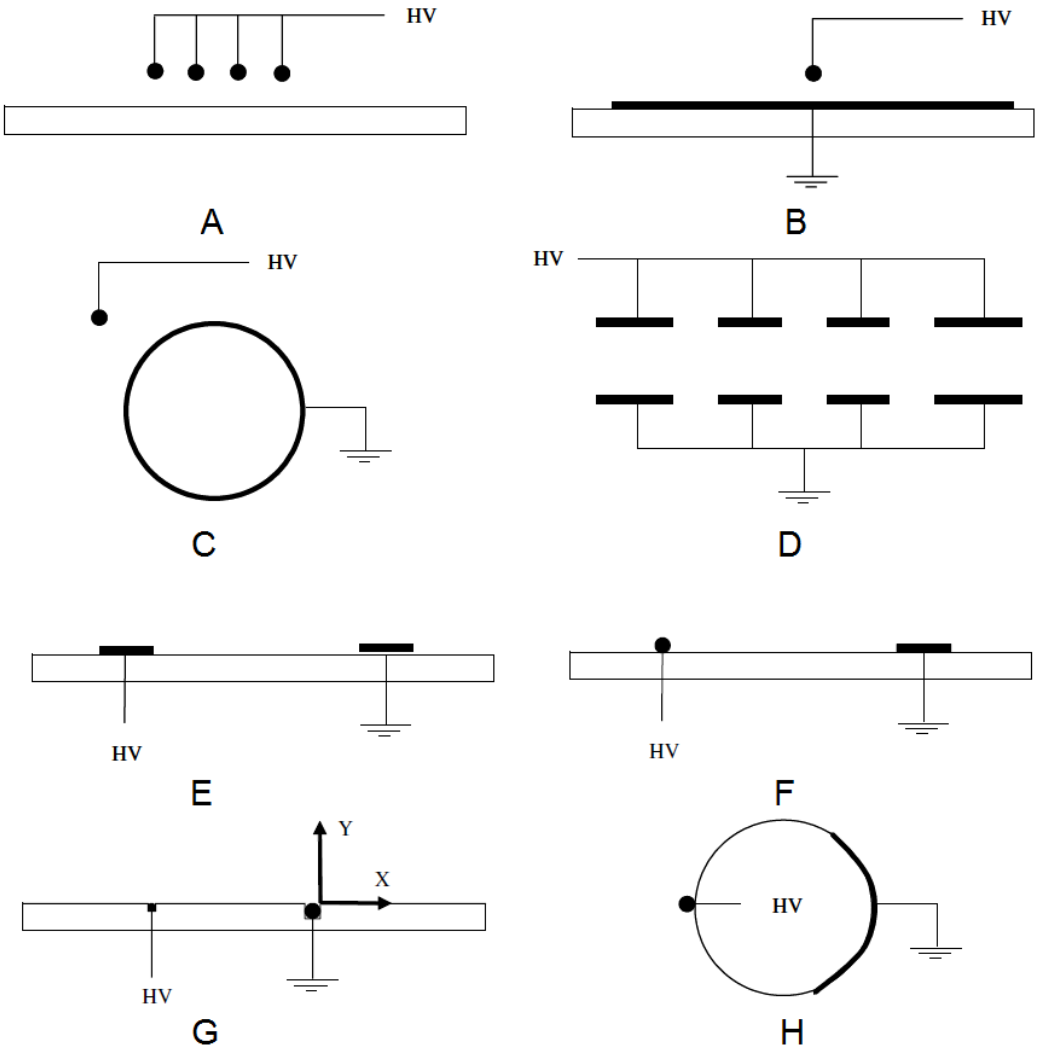

Figure 2-3. Different electrode geometrical configurations found in the literature as dc plasma actuators: A) Volumetric multiple wire. B) Volumetric wire-to-plate in plane configuration. C) Volumetric wire-to-plate in cylindrical configuration. D) Volumetric multi-hole plate-to-plate configuration. E) Surface plate-to-plate. F) Surface wire-to-plate. G) Surface wire-to-wire. H) Surface wire-to-plate or point-to-plate in cylindrical configuration (Moreau, 2007).

In summary, atmospheric pressure plasma actuators can be classified by their discharge mechanism as well as the geometry of their electrodes configuration. In

comparison with DBD plasma actuators, corona discharge plasma actuators only generate plasma near the sharp electrodes. And volumetric plasma actuators can avoid the viscous shear stress near the wall. In order to design a more efficient plasma actuator, corona discharge and volumetric electrodes configuration will be investigated further in the following section.

2.2 Corona Discharge Based Plasma Actuators

As discussed in the precious section, corona discharge based plasma actuators only generate plasma corona near the sharp electrodes while maintaining a constant strong electric field between electrodes. In the process of inducing airflow, energy used to heat and light is negligible. These characteristics make this type of plasma actuator great potential to improve their efficiency and to be used in industrial applications.

In this section, the focus is on the plasma actuators based on corona discharge. In order to further understand the mechanism and characteristics of this type of plasma actuators, physics of corona discharge and previous work related to this type of plasma actuators will be reviewed.

2.2.1 Physics of Corona Discharge and Electric Wind

Plasma is a fully or partially ionized gas. It is defined as the fourth state of matter and constitutes more than 99% of the universe. Electrons, ions and neutral particles in fundamental and excited states are the particles in the plasma. From point of view at macroscopic level, plasma is electrically neutral in a certain volume. However, plasma also contains free charge carriers. Thus, it is electrically conductive.

A plasma is created by applying energy to a gas (Conrads & Schmidt, 2000) in order to break the electronic structure of the neutral particles (atoms, molecules) and to

generate electrons, excited neutral particles and ions. This energy can be thermal, or carried by either an electric current or electromagnetic radiations.

The atmospheric corona discharge plasmas described in this study are generated by the energy from electrical current. The electric field gives energy to the free electrons (which have the highest mobility among the charged particles) in gas. This energy carried by electrons can be then transferred to the neutral particles through collisions. These collisions (Braithwaite, 2000) follow probabilistic rules and can be divided in two distinguishable forms. The first form is elastic collisions. This kind of collisions only slightly raise their kinetic energy but does not change the internal energy of the neutral species. On the other side, when energy carried by electron is high enough, the collisions change the electronic structure of the target particles. Then, the excited particles or ions (if energy carried by electron is even higher) can be generated. This kind of collisions is called inelastic collisions.

Generally, another distinction of plasma can be made between plasmas at local thermodynamic (or thermal) equilibrium (LTE) and at Non-local thermodynamic equilibrium (non-LTE). They are also known as thermal plasmas (LTE plasmas) and cold plasmas (non-LTE plasmas). The primary property that distinguishes them is whether the electron temperature is the same as the heavy particle temperature or not. Detailed properties of LTE and non-LTE plasmas are listed in Table 2-2.

The LTE notion (Griem, 1962) is really important, especially for a spectroscopic study of the plasma, since the determination of the plasma parameters (electron, excitation, vibration temperatures and so on) is based on whether the plasma is in LTE or not.

Table 2-2. Main characteristics of LTE and non-LTE plasma (Claire, et al, 2006)

	LTE plasmas	Non-LTE plasmas
Current name	Thermal plasmas	Cold plasmas
Properties	$T_e = T_h$ High electron density: 10^{21}– $10^{26}\ m^{-3}$ Inelastic collisions between electrons and heavy particles create the plasma reactive species whereas elastic collisions heat the heavy particles (the electrons energy is thus consumed)	$T_e \gg T_h$ Lower electron density: $< 10^{19}\ m^{-3}$ Inelastic collisions between electrons and heavy particles induce the plasma chemistry. Heavy particles are slightly heated by a few elastic collisions (that is why the electrons energy remains very high)
Examples	Arc plasma (core) $T_e = T_h \approx 10{,}000\ K$	Glow discharges $T_e \approx 100,\ T_h \approx 10{,}000 - 100{,}000\ K$

Those rules for LTE are very strict. Thus, most of the plasmas are not in LTE, especially all types of low density plasma in laboratories. Apparently, the corona discharge plasmas discussed in this work is non-LTE plasma with a heavy particle temperature close to room temperature. In the non-LTE plasma, electrons with much higher temperature move much faster than heavy particles which can be considered static. Thus, the majority of collisions and transitions phenomena is governed by energetic electrons.

As a non-LTE plasma source, corona discharges are relatively low power electrical discharges that take place at or near atmospheric pressure. The corona is invariably generated by strong electric fields associated with small radius of curvature, such as small diameter wires, needles, or sharp edges of the electrode. The corona discharge looks like many filamentary discharges radiating outward from the powered electrode with small radius of curvature. Because the corona is relatively easy to create

in atmospheric condition, it has already been applied in a variety of industry and research areas.

Corona discharge is a non-LTE discharge with low current density and relatively high voltage. Depending on polarity of the input signal, corona discharge could be classified as a Townsend discharge or a negative glow discharge (Schutze, et al., 1998). Figure 2-4 shows a design of the standard point-to-plane corona discharge setup, which can create a strong electric field thus an ionization zone around the point where the high voltage is applied. For different polarity of the input signal, the mechanism is different to sustaining the continuous ionization near the high voltage electrode. If the point electrode is powered with negative HV signal, it is called a negative corona. If the point electrode is powered with positive HV signal, then it is a positive corona. The HV input signal can be continuous or pulsed DC signal or even AC signal. Typically, for the positive corona discharge operating with this point-to-plane configuration, the power and input DC voltage follow a relationship (Moreau, 2007):

$$P_{elec} = C_{pow} V^2 (V - V_0), \tag{2-3}$$

where P_{elec} is the time-average electrical power consumed, V the potential difference between electrodes, V_0 the ignition voltage of the corona discharge and C_{pow} a constant depending on the electrode gap (typically between 0.1 and 1 μA(kV)$^{-2}$ in air (Zouzou, Moreau, & Touchard, 2006)).

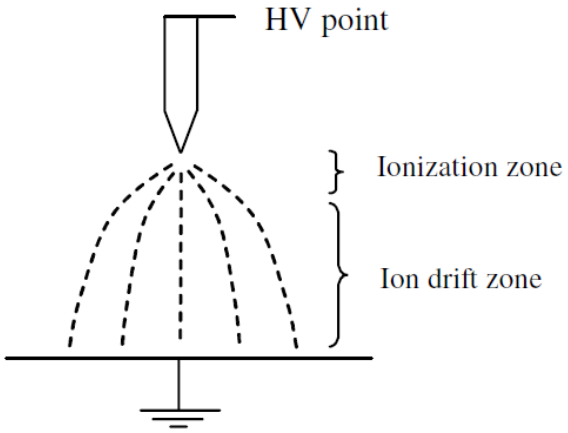

Figure 2-4. Schematic of a point-to-plate corona discharge configuration (Moreau, 2007).

Corona discharges can be classified in several forms, mainly depending on the polarity of the field and the electrode geometrical configurations. For positive corona in the needle-to-plate configuration, discharges start with burst pulse corona and proceed to the streamer corona, glow corona, and spark discharge while the applied voltage increases (Figure 2-5). For negative corona in the same geometry, the initial form will be the Trichel pulse corona, which is followed by a pulseless corona and then a spark discharge as the applied voltage increases. For a wire-pipe or wire-plate electrode configuration, corona generated at a positive wire electrode may appear as a tight ionization sheath around the powered electrode or as a streamer moving outward from the powered wire electrode. Corona generated at negative electrodes may take the form of a general, rapidly moving glow or it may be concentrated into small active spots. Negative corona generally propagates by impact ionization of the gas molecules. While positive corona depends more on photoionization for its propagation.

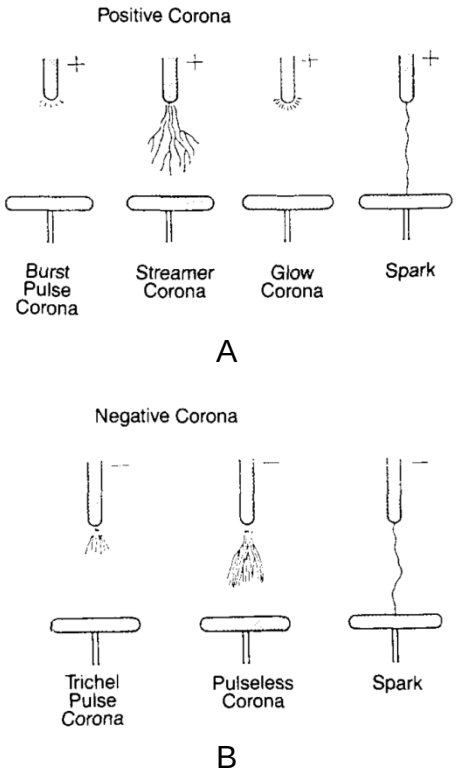

Figure 2-5. Schematic of corona discharges (Chang, Lawless, & Yamamoto, 1991).

The positive corona form is also known as a Hermstein's glow (Hermstein, 1960) and is similar to the low pressure discharge in a Geiger tube. It is characterized by a steady current at a fixed voltage, quiet operation, and almost no sparking. The negative corona is made up of individual electron avalanches. Thus, the current of the discharge consists of many tiny spikes. However, the total current is relatively steady.

The corona discharge is usually space-charge limited in magnitude, since the plasma emits ions of one polarity that accumulate in the inter-electrode space apart from ionization sheath (several Debye lengths thick, $d_{Debye} = \sqrt{\varepsilon_0 k_B T_e / n_e q_e^2}$, where ε_0 is permittivity of free space, k_B is the Boltzmann constant, T_e is the temperatures of the electrons, n_e is the density of electrons, q_e is the charge of an electron). Thus, the corona discharge has a positive resistance characteristic: increase in current needs

higher voltage to drive. However, when the total current keeps increase to a certain level, other charged particles will be generated to carry current. Thus arc discharges will be formed. The arc discharge is characterized by a negative resistance characteristic.

For flow jet actuation purposes, different polarity will also introduce different mechanisms. In the case of a positive corona, it is assumed that electrons are produced by photo ionization in the electrode gap. These electrons are accelerated towards the point anode, resulting in an avalanche. An ionization zone is created around the point anode, where the number of positive ions and electrons is equal. This corresponds to a plasma zone of a few tenths of a millimeter. Then ions are repulsed towards the cathode by Coulombian forces, and constitute the drift region, where one can assume that there is no recombination because the electric field is not sufficiently large. In the case of the negative corona, Goldman and Sigmond (Goldman & Sigmond, 1982) assume that positive ions created by detachment in the ionization zone go rapidly towards the cathode. Then negative ions created by attachment drift towards the grounded plane electrode.

As explained by Robinson in his famous paper (Myron Robinson, 1961), ‘the phenomenon variously known as the electric wind, corona wind and electric aura refers to the movement of gas induced by the repulsion of ions from the vicinity of a high voltage electrode’. This phenomenon was reported for the first time in 1709 by Hauksbee and the first explanation was given by Faraday in 1838. A history of the electric wind is given in (M. Robinson, 1962). Many recent works are still dealing with electric wind.

Indeed, the electric wind is due to the momentum transfer between the ions accelerated by electric field and the neutral particles in the electrode gap region. However, although the electron velocity is much higher than the ion one, one can neglect the role of electrons because their mass is very low compared with that of ions. Thus only small amount of momentum can be carried by electrons.

2.2.2 Previous Study on Corona Discharge Based Plasma Actuators

Corona discharge has been used for industrial applications for a few decades now (e.g., electrostatic precipitators). Thus, large amount of research work has been done for the development of applications using corona discharge. Among these applications, the plasma actuator is the most representative one. The investigation of the corona plasma actuator can be classified into two parts: analyzing the characteristics of flow jet generated in various electrode arrangements, and verifying its performance in various applications like cooling, active flow control and so on.

Study on the characteristics in various electrode arrangements has been performed since the 1960's, and many cases such as plate to plate (McKinney, Davidson, & Leone, 1992), parallel plates (Asano, Hishinuma, & Yatsuzuka, 2000), wire to cylinder (Zebboudj & Ikene, 2000), wire to plate (Zebboudj & Ikene, 2000), rod to plate (Toyota, Zama, Akamine, Matsuoka, & Hidaka, 2002), sphere to sphere (Toyota, et al., 2002), and needle to plate (Kalman & Sher, 2001), have been studied so far. Especially, (Drews, Cademartiri, Whitesides, & Bishop, 2013) showed that the ion cloud generated by corona discharge reduces its size when the signal frequency increases (Figure 2-6).

Study on the verification of the applications of electric wind has recently been performed widely. Kalman (Kalman & Sher, 2001), Molki (Molki & Bhamidipati, 2004),

Go (Go, et al., 2008), and Sheu (Sheu, Hsiao, & Wang, 2013), proved the cooling performance of the corona plasma actuator for wire to plate, wire to cylinder, wire to flat plate, and point to flat plate electrode arrangements. Kasayapanand used the computational fluid dynamics technique to analyze the cooling performance of electric wind for a vertical fin array, and Chen (Chen, Guo, Yang, & Wang, 2013) verified the cooling performance of the corona plasma actuator for LED devices by measuring the thermal resistivity of the LEDs.

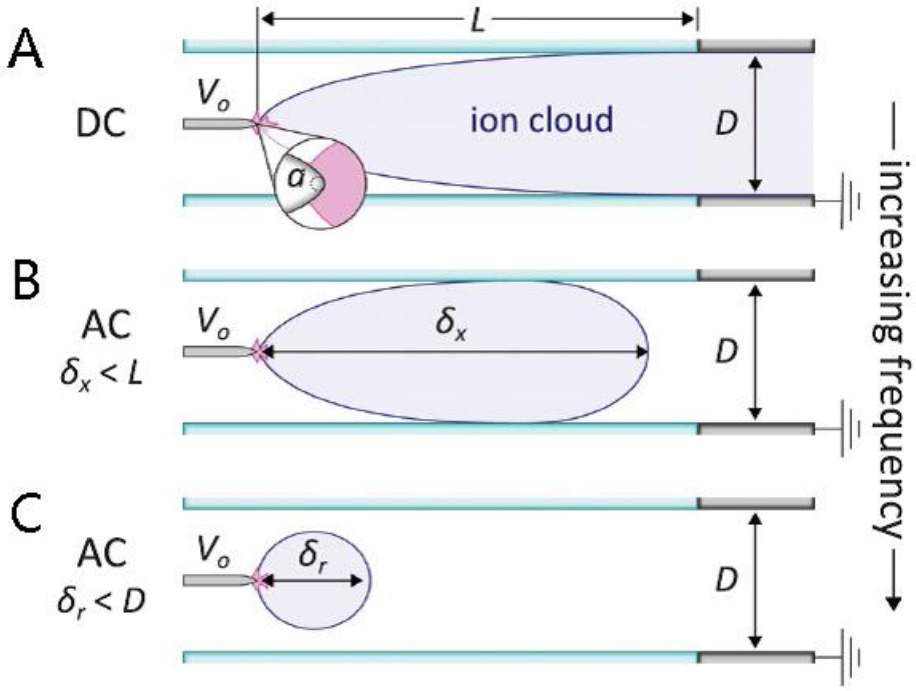

Figure 2-6. Discharge model schematic (Drews, et al., 2013). A) At DC to low frequencies, the ion cloud extends a distance L to the counter electrode where ions are consumed. B) At high frequencies, the ion cloud extends only a distance δ_x before begin consumed by ion-ion recombination. C) At even higher frequencies, the ion cloud is increasingly localized to within a distance δ_r near the tip of the point electrode.

CHAPTER 3
DESIGN AND CHARACTERIZATION OF EFFICIENT PLASMA ACTUATORS

In this section, corona discharge and volumetric geometry are chosen to design an efficient plasma actuator working under atmospheric pressure condition. Specifically, channel electrodes configuration is used to avoid viscous shear stress near the surface. Sharp needles are used as powering electrodes to enhance the volumetric corona plasma near the tip.

Corona discharge based needle actuation devices with low energy loss are tested and shown to generate airflow up to $3.4\ \mathrm{ms}^{-1}$ while consuming only milliwatts level power. In a specific configuration, the needle actuation device inside a channel show approximately 3000% and 300% increase in energy conversion efficiency as compared to conventional surface and channel dielectric barrier discharge actuators, respectively. The polarity of the needle is shown to have an effect on actuator performance, with positive polarity yielding better efficiency.

3.1 Experiment Setup

An experiment was designed to develop and test the needle actuation devices. Channel electrodes configuration was used to develop an efficient corona discharge plasma actuator. Then, PIV and electrical parameter measurement were employed to examine the performance of this type of plasma actuator.

3.1.1 Electrodes Configuration

The electrodes configuration used to inducing a channel flow is shown in Figure 3-1. Here, a steel needle powered with high voltage is placed upstream between two plate electrodes to induce a jet at the core of the channel cross-section. With this configuration, direct momentum transfer into bulk flow happens near the center of the

channel height and should be affected by significantly less wall shear in comparison to the wall jet configuration where both electrodes are at the wall.

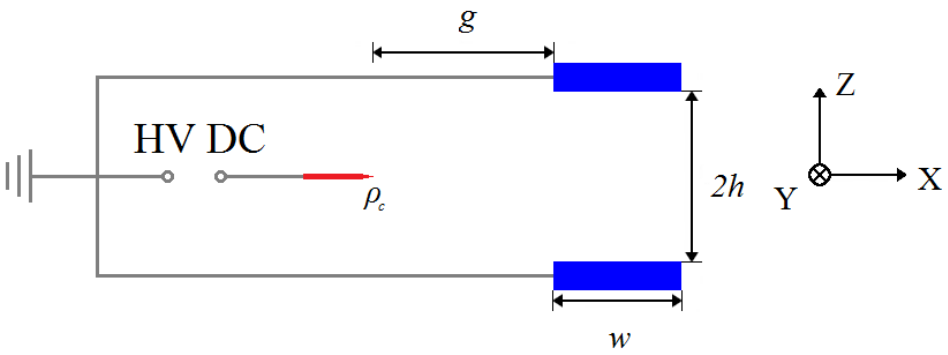

Figure 3-1. Channel electrodes configuration of needle actuation device.

Detailed description of dimensions and experiment setup are shown in Figure 3-1 and described below. Powered needles and plate electrodes are separated by gap *g* in x-direction and height *h* in z-direction. And the width of plate electrode denotes as *w* in the configuration. In all test cases, y-direction (span-wise) length of plate electrodes is set to be 10 cm. For channel configuration, only one needle is mounted in the configuration while multiple needles evenly separated in y-direction (span-wise) are employed in cooling and vortex generation setup. The needles are powered with high voltage DC supply (TREK Model 30/20A High-Voltage Power Amplifier) and the plate electrodes are grounded. The DC signal used here is continuous with constant amplitude. All needles used in this letter have a nominal radius of curvature $\rho_c = 50\ \mu\text{m}$, and all plate electrodes are 60 µm thick and $5\ \text{mm}$ wide ($w = 5\text{mm}$). Also in all cases $h = 2.5\ \text{mm}$.

3.1.2 Experimental Method

The performances of the needle actuation device are tested by measuring its electrical parameters and velocity of the airflow induced. Then, the electrical properties and aerodynamic performance of the needle actuation devices can be analyzed.

Electrical parameters were measured using an oscilloscope (Tektronix DPO2014) and a digital multi-meter (BK Precision 5491A). DC Voltage was measured using a passive probe (Tektronix Model P6015A) with an attenuation of 1000× through the oscilloscope. The oscilloscope has a maximum sampling rate of $1\ \mathrm{GSa}/s$ at a bandwidth of $100\ \mathrm{MHz}$. The range of voltages used in the power and efficiency study is from $6\ \mathrm{kV}$ to $12\ \mathrm{kV}$. The digital multi-meter of 1 mV resolution was used to measure the potential difference across a 1 MΩ resistor connected in series with the actuator. This potential difference can be converted to current with an equivalent resolution of 1 nA. Voltage and current were obtained from the measurement to calculate average electrical power using V-I method,

$$P_{elec} = \frac{1}{T}\int_0^T VIdt, \tag{3-1}$$

where V and I are voltage and current measured, respectively. The integration is performed over a T = 10 s period.

LaVision PIV system was used to collect the velocity profile due to needle actuation. Laser sheet used to illuminate Ondina oil seeding particles with diameter of 0.8 μm was created by a $532\ \mathrm{nm}$ Nd:YAG (New Wave Research Model Solo PIV II 30) laser generator fitted with a divergent cylindrical lens. Images of illuminated seeding particles were captured by a Phantom 7.3 high speed camera which has a resolution of

800×600 pixels on a $60\ \mathrm{mm} \times 45\ \mathrm{mm}$ window size. LaVision's Davis 7.2 software was used to control both laser generator and high speed camera by generating external trigger through Model PTU-9, programmable timing unit (synchronization resolution of 10 ns with <1 ns jitter). In this study, PIV system was employed to capture XY-plane and XZ-plane velocity profile for 3-D velocity visualization of the needle actuation channel and YZ-plane velocity profile to show vortex generation. According to a recent study (R. Durscher & S. Roy, 2012), statistical convergence for the plasma jet is within 300 samples (image pairs for correlation). Nonetheless, we took 1000 samples to eliminate the deviation. The uncertainty of the PIV results is less than 3.9 % without velocity gradient and is less than 13 % with maximum gradient in the experiment. Detailed uncertainty analysis is shown in Appendix.

According to the velocity profile measured from the PIV system, electro-mechanical energy conversion efficiency was obtained to evaluate the performance of the needle actuation device. In mechanical engineering, the induced mechanical power of the airflow inside a duct is given by (Moreau, 2007)

$$P_{mec} = \frac{\rho}{2} \iint u_x^3 dA, \tag{3-2}$$

where ρ is the air density, u_x is the velocity at X-direction and the 2-D integration covers all the channel cross section area A in YZ-plane. Under its definition, electro-mechanical energy conversion efficiency can be calculated as the ratio of the induced mechanical power of the airflow to the electrical power consumed in the circuit,

$$\eta = P_{mec}/P_{elec} \tag{3-3}$$

3.2 Result and Discussion

After gathering the data from the experiment, analyzing processing is demonstrated in this section. PIV results give the aerodynamic properties of the needle actuation devices. Electrical properties are obtained from the electrical parameters measured. Then a discussion on the results is performed to further understand the performance of the device.

3.2.1 PIV Study

Figure 3-2 shows the PIV data for the velocity field induced by the needle actuation channel powered with a positive 12 kV DC signal. This was the highest positive voltage that could be applied to the channel while maintaining the steady glow and generating a maximum velocity of 2.6 m/s. PIV results shown on the XZ-plane (Figure 3-2A) and the XY-plane (Figure 3-2B) demonstrate the 3-D flow structure generated by a single needle actuated channel flow. Figure 3-2A shows strong jet flow covering the entire channel exit in Z-direction with distinct entrainment effects from both sides of the channel. The induced airflow covers about 2 cm wide region at the channel exit in Y-direction. Note that a single needle was powered to create this velocity field. A uniform flow field can be generated by using an array of carefully positioned needles. Also, a strong airflow penetration effect into quiescent surroundings can be noticed in both XY- and XZ-plane. These results suggest that this DC needle channel configuration has great potential in flow control and propulsion applications.

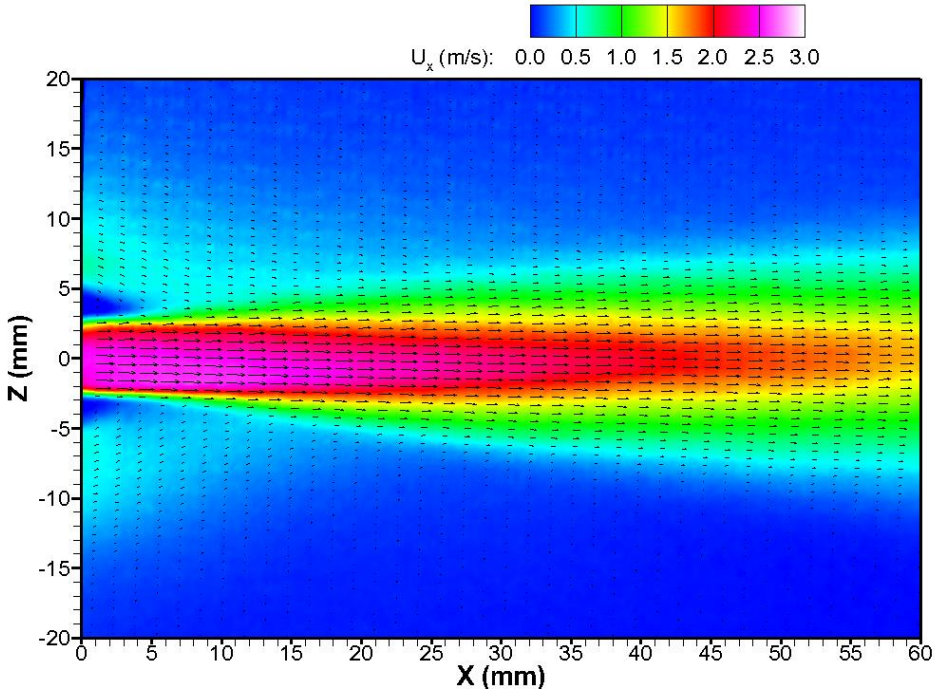

A

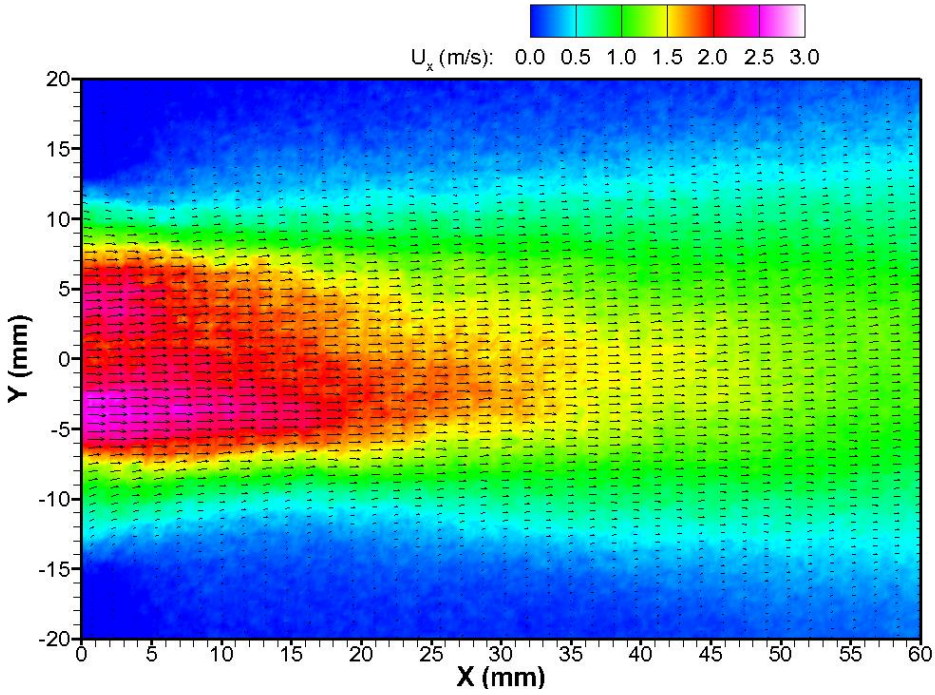

B

Figure 3-2. PIV velocity profiles. A) XZ-plane velocity field for needle actuation channel operated at positive 12kV DC. B) XY-plane velocity field for needle actuation channel operated at positive 12kV DC.

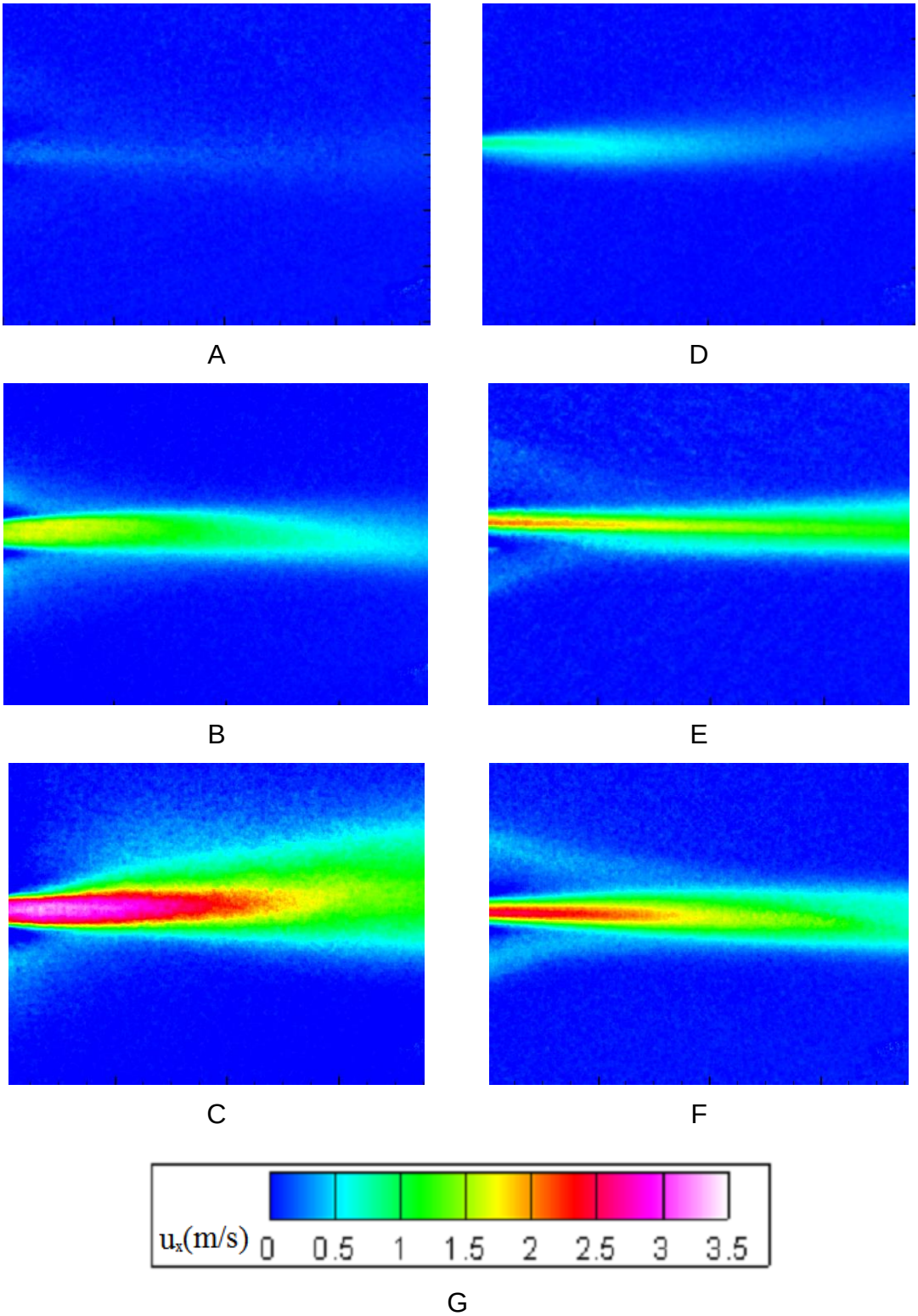

Figure 3-3. XY-plane velocity fields. A) -6 kV. B) -9 kV. C) -12 kV and positive. D) 6 kV. E) 9 kV. F) 12 kV input signal. G) Color scheme for x-component velocity.

Figure 3-3 shows the velocity field for different input signals of both polarities. Both polarities applied can induce airflow from 6 kV to 12 kV. At 6 kV and 9 kV, the maximum velocity (in the core region of the jet) induced by positive input signal is larger than that induced by negative input signal. However, Negative input signal with 12 kV create the max velocity ($3.4\ \mathrm{m}s^{-1}$) of the entire study.

Figure 3-4 displays the velocity line profile at downstream of the channel exit (X = 2 mm) under different operating signals. As shown in Figure 3-4A, B, velocity profile generated by the negative DC signal is adhering to the plate electrodes and has a nearly flat middle region. This indicates that the momentum transfer from negative ions to neutral particles mainly happens near the wall. This is evidence for electron attachment occurring outside the ionization zone and around the needle tip. On the other hand, velocity profile of positive signal shows a sharp peak at the middle of the channel as displayed in Figure 3-4A, B, which suggests the momentum transfer between positive ions and neutral particles mainly happens near the ionization zone around the needle tip. In addition, this phenomenon also suggests that applying positive signal on the channel configuration will have less wall shear in comparison to applying negative signal. For the span-wise (Y-axis) velocity distribution shown in Figure 3-5, both positive and negative signals generate similar effective region width at 9kV as the wall effects are minimal for this direction. In addition, induced mechanical power was calculated by integrating measured velocity profiles along the Y- and Z-axes.

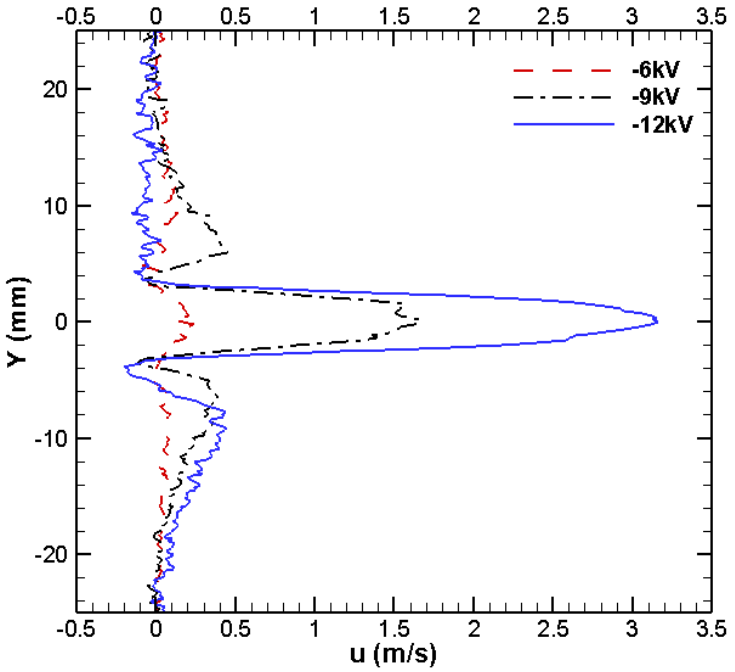

A

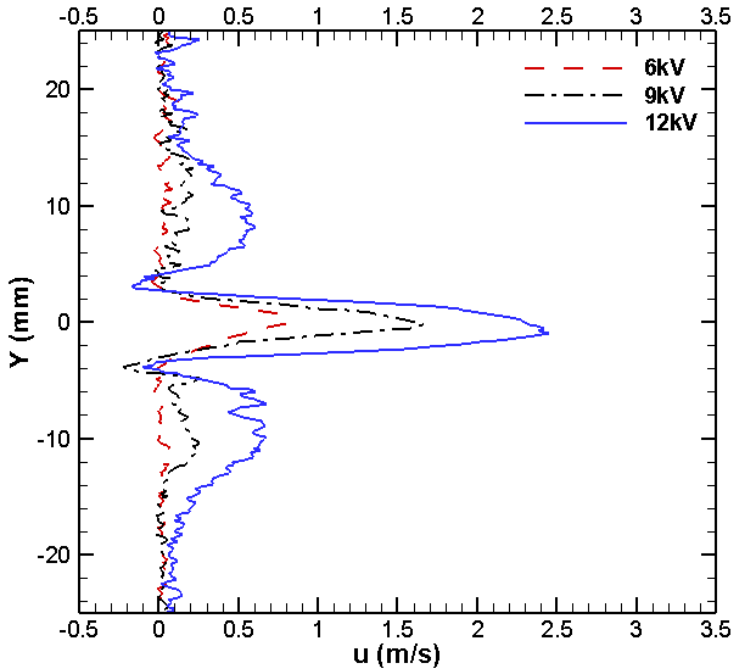

B

Figure 3-4. Y-axis velocity line profiles at downstream of the exit (X = 2 mm) of the needle actuation channel. A) Positive DC signals. B) Negative DC signals.

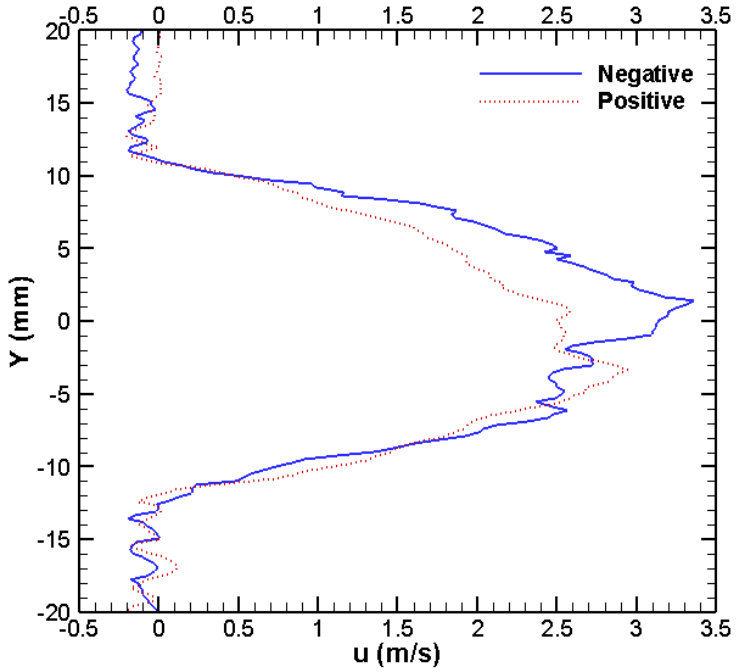

Figure 3-5. Z-axis line velocity profile at downstream of the exit (X = 2 mm) of the needle actuation channel for positive and negative 12 kV DC signal

3.2.2 Power Consumption Study

Figure 3-6 shows the channel electrical power consumptions and maximum velocities as a function of applied voltage for both positive and negative signals in log scale. Interestingly, both power profiles can be characterized by $P \propto V^{\alpha}$ using linear regression with coefficient of determination $R^2 > 0.99$. The power consumption by the negative DC signal increases faster (α = 9.4) than that by the positive DC signal (α = 5.6). This difference is mainly due to the different mechanism of generating working ions. For positive signal, majority positive ions are generated inside the ionization zone near the needle tip. Contrarily for negative signal, majority negative ions are generated by electron attachment outside the ionization zone. When absolute signal amplitude increases, positive ion generation becomes limited by the size of the ionization zone

while much more electrons can be used to generate negative ions outside the ionization zone. This manifests as a faster growth in peak velocity with voltage for the negative DC input signal. Note that the power consumed by the needle actuation channel is only several milliwatts, which is extremely low compared to other plasma actuated flows.

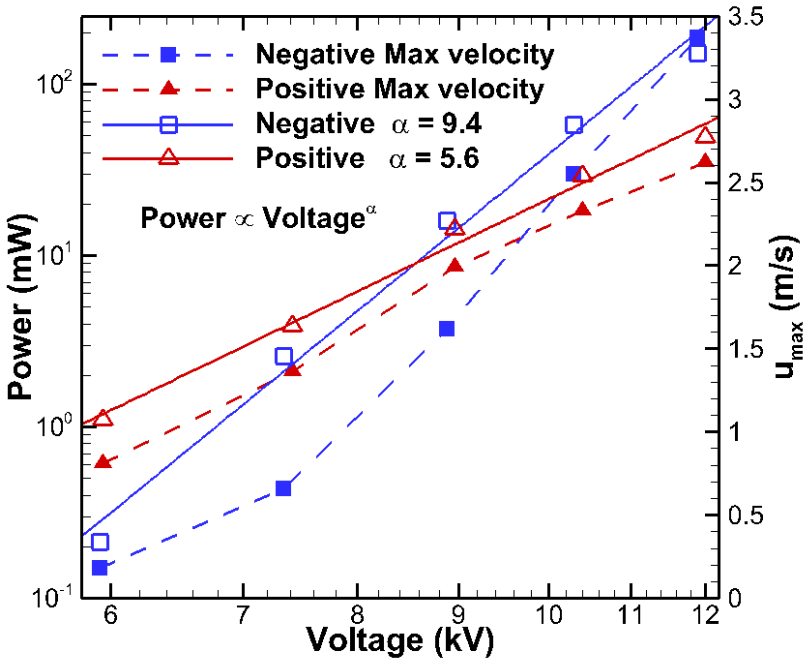

Figure 3-6. Electrical power consumption and maximum inducing velocity of the needle actuation channel for various applied positive and negative voltages.

Calculated electro-mechanical energy conversion efficiencies for both positive and negative signals are displayed in Figure 3-7. Note the maximum efficiencies for the needle actuation channel were 2.8% and 1.5% for positive and negative DC signals, respectively. These efficiencies are one order of magnitude larger than the reported efficiency of the surface corona actuator (Moreau, 2007) and are about twice of the reported efficiency of wire to cylinder configuration (Colas, et al., 2010). Interestingly, efficiencies for both polarities were attained at a magnitude of 7.5 kV DC input. For both

positive and negative input voltages, the efficiency increases rapidly from 6 kV to 7.5 kV and then gradually decreases from 7.5 kV to 12 kV. This suggests that more energy is wasted at higher voltages. One can also notice that the efficiency of positive signal is about twice that of the efficiency of the negative signal for the same voltage magnitude. This might be explained by the loss in mechanical power output from wall shear due to different flow structure mentioned above.

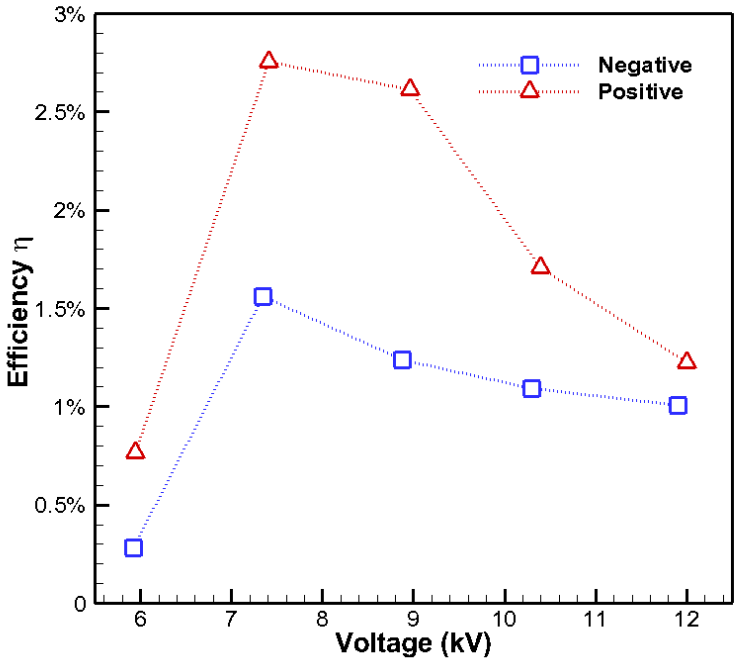

Figure 3-7. Energy conversion efficiency of the needle channel for various applied positive and negative voltages.

3.3 Conclusion

In summary, the performance and potential applications of the low power DC needle actuation devices with channel or plate configuration have been demonstrated. For the channel configuration, momentum was directly injected by the needle-to-plate electrodes configuration into the bulk airflow of the channel minimizing the viscous penalty from induced wall shear stress (as compared to a wall jet configuration of

standard DBD?). Both positive and negative high voltage DC signals were used to generate strong ionic flow in the same direction. However, positive ionic flow with a stronger peak near the center causes less viscous penalty than negative ionic flow adhering to the plate electrodes resulting in higher energy conversion efficiency for positive signal. Plasma jet from a single needle actuator can cover 2 cm range in span-wise direction (Y axis) with a strong core flow jet. In combination of these characters, the electro-mechanical energy conversion efficiency of such device can reach up to 2.8 %, almost equal to 30 times that of standard DBD channel (Riherd & Roy, 2012) or 4 times that of wire DBD channel (Campbell & Roy, 2014). Strong entrainment effect was also observed during the study.

Efficient corona discharge based plasma actuators are developed and examined. A maximum 2.8 % energy conversion efficiency is achieved. Only milliwatts level energy is consumed to generate strong channel airflow jet with maximum velocity up to $3.4\ \mathrm{m}s^{-1}$.

CHAPTER 4
SURFACE COOLING USING EFFICIENT PLASMA ACTUATORS

The use of electric winds in the presence of a wall jet flow to modulate an external boundary layer has been an area of growing interest in the aerospace community, but has received little attention for heat transfer enhancement. Soetomo (1992), and more recently, Léger et al. (2002) and Artana et al. (2002), demonstrated the ability of corona discharges to reduce drag by modulating the boundary layer on a flat plate. Using electrodes perpendicular to the flow and either flush or in contact with a flat plate, they demonstrated a near-wall electric wind that accelerates the local boundary layer, promoting drag reduction. In a similar way, electric winds can also be used to enhance convective heat transfer on a hot surface. Heat transfer enhancement by electric winds in the presence of external flows were reported by Velkoff and Godfrey (1979), who used an array of corona wires aligned with the flow and extended above a flat plate. With the flat plate acting as the collecting electrode, they demonstrated that heat transfer is enhanced in the low-velocity regime but that the ionic wind is swamped by the bulk flow, and thus ineffective, as the bulk velocity increases.

In this chapter, the performance of surface cooling using developed efficient plasma actuators is examined with variety of parameters. The results are reported along with the discussion.

4.1 Experiment Setup

In order to evaluate the cooling performance of the developed efficient plasma actuators, an experimental system was setup to simulate the normal cooling process near a CPU chip inside an electronic device. The experimental system includes a designed efficient plasma actuator for surface cooling and the DC high voltage powering

system, electrical parameter measurement devices, and a semi-insulated rubber heater simulates the hot CPU chip, a closeable transparent acrylic testing chamber, environmental condition monitor device, temperature measurement devices and the PIV analysis system. According to the function of these components, the entire system can be divided into two sections: testing section and measuring section. The testing section includes the chamber, the actuator and the monitor device. On the other hand, electrical and thermal measurement devices and the PIV system belong to the measuring section.

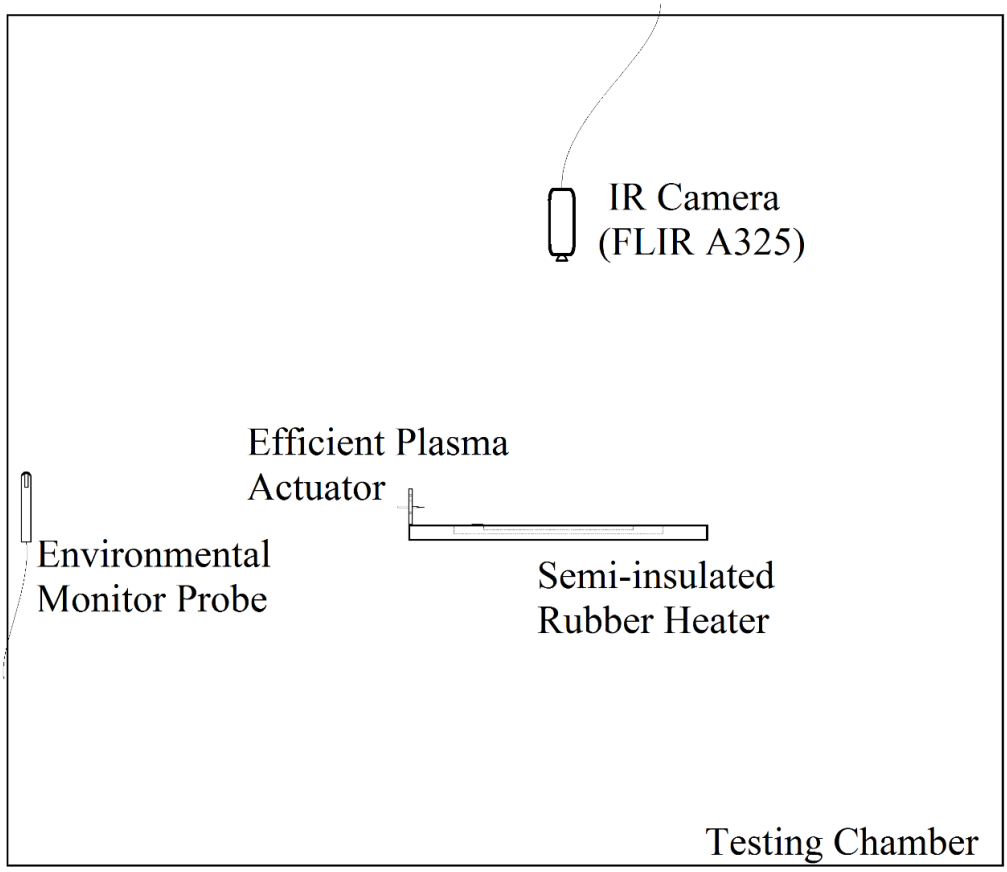

Figure 4-1. Experimental setup inside the transparent testing chamber (Not to scale).

The overview of the testing section for the experiment system is displayed in Figure 4.1. Adjacent to the semi-insulated rubber heater, the efficient plasma actuator

for surface cooling was placed in the center of the transparent testing chamber which has the dimension of $L \times W \times H = 120 \times 60 \times 120$ mm. IR camera was placed right above the actuator to measure the surface temperature. In order to measure the upstream air condition, the probe of the environmental monitor device was attached on the wall of the chamber to the upstream direct of the actuator. DC high voltage powering system and measuring section (excluding the IR camera) were located outside the chamber to avoid perturbing the flow while running the experiment.

4.1.1 Electrodes Configuration Design

For the purpose of enhancing convection cooling effect on a surface, a wall jet need to be created near the hot surface. So the channel electrodes configuration, which create the channel jet flow, is not the best solution here. A wall jet must be generated by a body force towards the target wall. Thus, only one ground electrode attached on the target surface is needed to drive the electrical field towards to that surface. After this, this kind of electrodes configuration is called single plate configuration.

The side view of the single plate configuration is shown in Figure 4-2. In the configuration, one single needle or an array of high voltage steel needles is located in the upstream side of the grounded single plate electrode on one surface. After applying with either positive or negative high voltage DC signal on the needle, such arrangement will create a corona discharge driven by an electric field from needle tip to the grounded single plate electrode on the surface. Then, this discharge should drive the airflow from upstream of the needle towards the surface after grounded electrode. This is the first time such configuration is used to explore convective cooling effects over a surface.

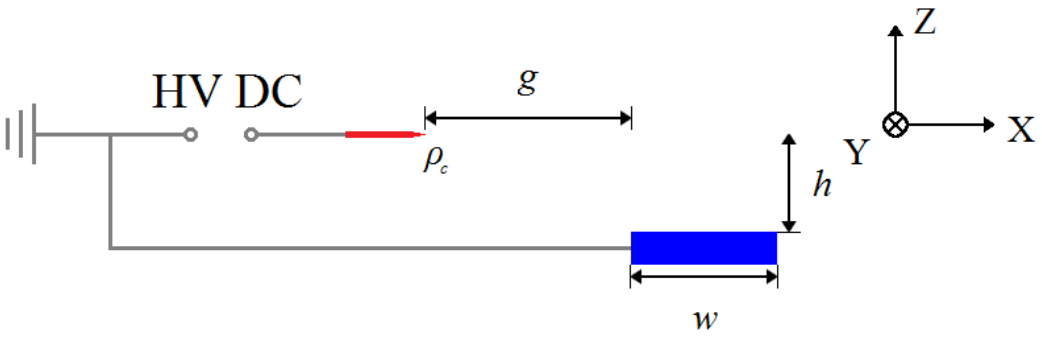

Figure 4-2. Side view of the electrodes configuration for surface cooling effect experiment with dimensions.

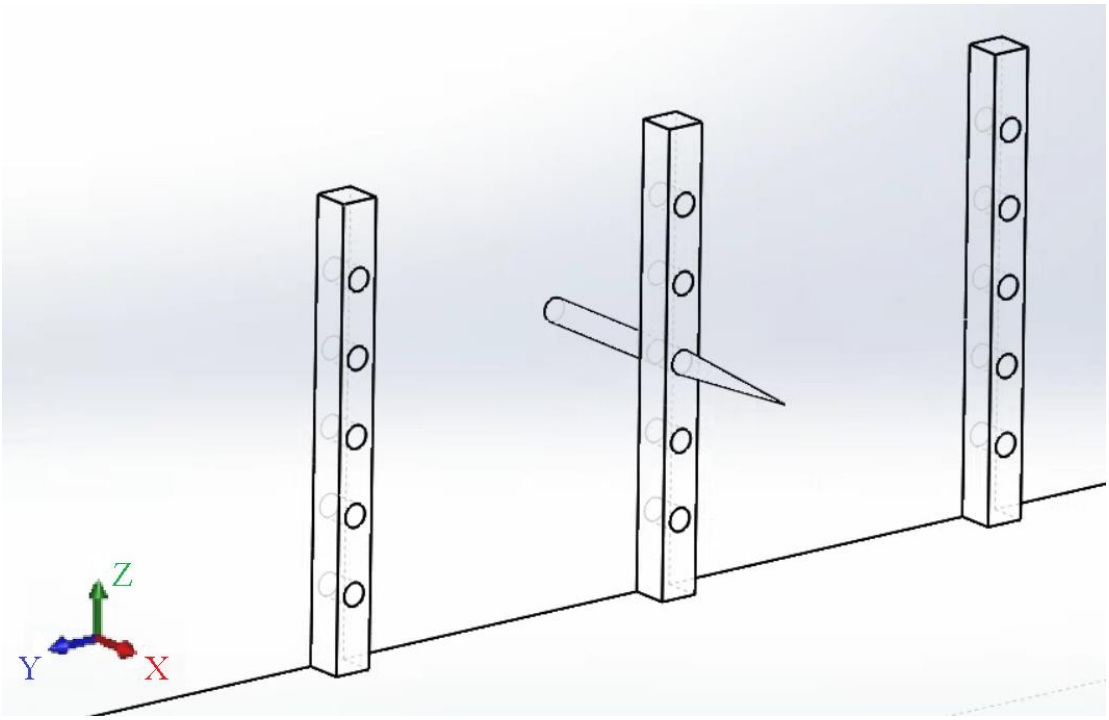

Figure 4-3. Vertical acrylic holder for needle electrodes (SolidWorks Drawing).

Detailed description of dimensions and experiment setup are shown in Figure. 4-2 and described below. Powered needle(s) and grounded plate electrode are separated by gap g in x-direction and height difference h in z-direction. And the width of plate electrode denotes as w in the configuration. In all test cases, y-direction (span-wise) length of plate electrodes is set to be 10 cm. All plate electrodes are 60 μm thick and

$5\ \mathrm{mm}$ width ($w\ =\ 5\ \mathrm{mm}$) and all gaps in the experiments of this chapter is set to be $15\ \mathrm{mm}$. However, the height difference between needle tip and ground electrodes, h, and the radius of curvature, ρ_c, will be varied during the experiment to study their effects on the cooling performance of the designed actuators.

As shown in Figure 4-3, thin straight vertical acrylic pillars were used to hold the needles during the experiment. Since the acrylic is a dielectric material and the thin design of the pillar, the influences on the electrical properties of the system and the flow field driven are considered negligible. On the acrylic pillar, 5 holes with the same diameter of the needle ($0.6\ \mathrm{mm}$) are located with different hole height from 2 mm to 10 mm with a 2 mm interval. All holes' heights were designed and measured for validation from the center of the hole to the plate surface. By placing needle in different holes, the height difference, h, can be varied to study its effects on cooling performance. The pillar was design in Solidworks and cut by a 150 W CO_2 laser cutter (UNIVERSAL laser system PLS6.150D) in the UF Infinity Fab Lab.

Steel needles were used as powered electrode in the designed corona discharge actuators. These tips of needles have varies radius of curvature, ρ_c, which is the most important property that affects performance of the actuators. As mentioned in Moreau's work (Moreau, Benard, Lan-Sun-Luk, & Chabriat, 2013), wire electrodes with smaller radius of curvature can generate stronger air flow jet. The reasons are listed below. Electrical potential is constant everyplace on the surface of a charged conductor, just like the needles used in this experiment. Also, on the surface of an irregularly-shaped conductor (non-sphere), the charge density is high in convex regions with small radius of curvature (especially, for example, at sharp points), and low in regions of large radius

of curvature, and therefore, by Gauss's Law, the field intensity must be high just above a sharp point, and relatively low just above a gently curved region.

In this test, the effects of radius of curvature on cooling performance were also examined by using needles with different radius of curvature. The radius of curvature of a single needle was determined using a high magnification microscope (Omano OM136C) with a camera (ESPA systems co. ltd D55EB digital LCD camera with maximum 10 Mega Pixel) instead of the ocular len(s). An example of how to measure the radius of curvature is displayed in Figure 4-4. Picture of the needle tip with 60X magnification was taken by the camera on the microscope. The focus plane of the picture was on the outline of the needle tip. Then a circle was fitted on the picture to match tip curve. The radius of the circle was measured according to the reference ruler as the radius of curvature of the needle tip. Three different radii of curvatures ($25\ \mu m, 50\ \mu m, 75\ \mu m$) were used during the test.

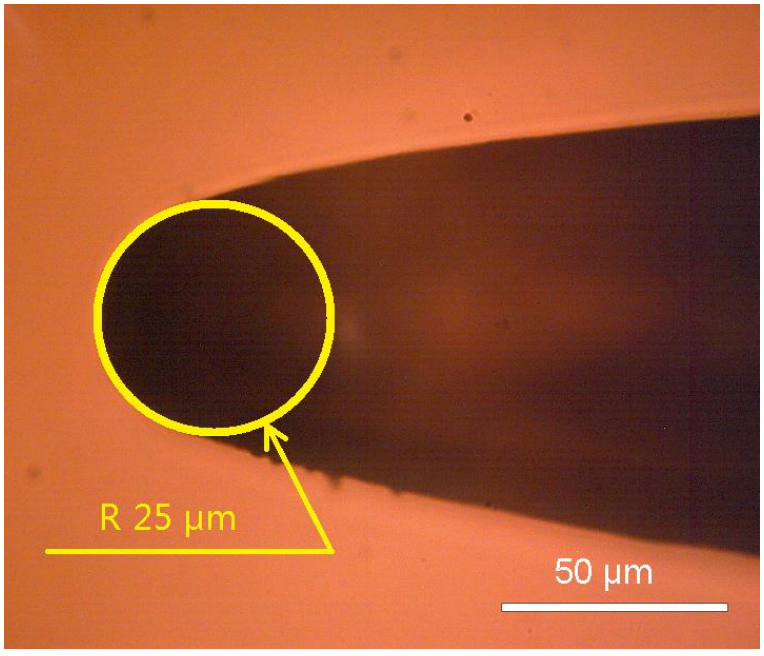

Figure 4-4. Example of the estimation process on radius of curvature of a thin needle tip.

4.1.2 Heat Source

In order to simulate a CPU chip as the heat source, a rubber heater with rated voltage 24 V and rated power 12 W was used in the experiment. The rubber heater is a resistive heater using joule heating mechanism with rubber layer coated outside the resistor array. The rubber heater has a $50\ \text{mm} \times 50\ \text{mm}$ top flat rubber surface with 2 mm in thickness. The flat surface is used as a hot surface during the test. In order to estimate the heat flux from the fat surface, all other surfaces of the rubber heater were insulated by a novel heat insulation material, Airloy™ X100 series materials. Airloy X103 with density class M is the first commercially-available mechanically robust aerogels with the strength to stand up to real-world applications. Although the Airloy is heavier and stronger than classic silica aerogels, it is still a thermally super insulating material with a heat conductivity less than $0.03\ \text{W}/(\text{m} \cdot \text{K})$ and a maximum operating temperature ~80 °C.

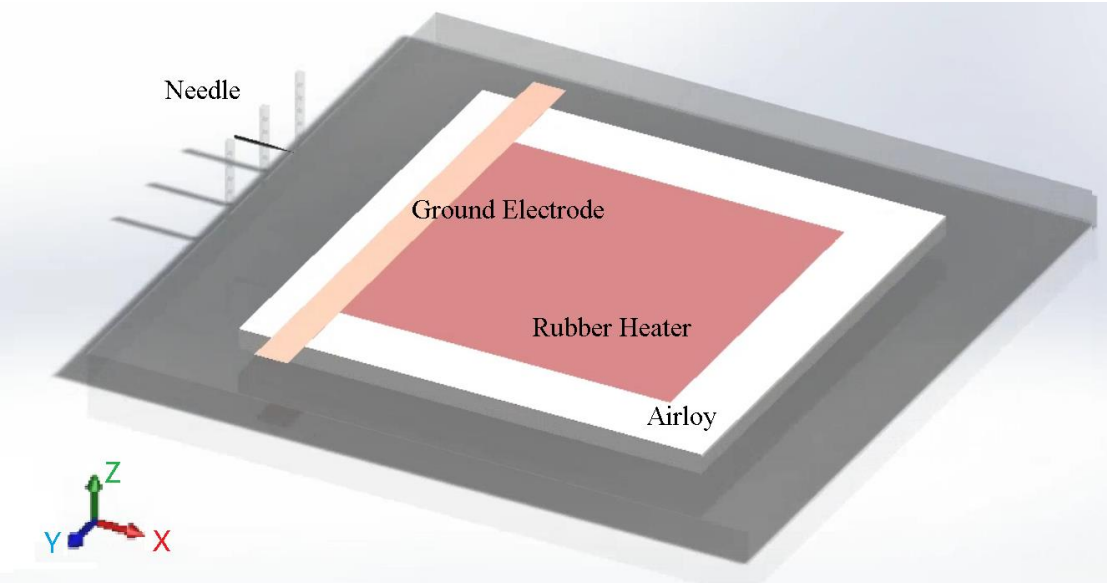

Figure 4-5. Design of the cooling performance test section including needle actuator and semi-insulated rubber heater (SolidWorks Drawing).

As displayed in Figure 4-5, rubber heater embedded in a piece of super insulating material, Airloy, was placed adjacent to the downstream of the grounded plate electrode. Such arrangement will allow wall jet airflow driven by the corona plasma actuator directly go through the hot surface of the rubber heater.

4.1.3 Electrical Supply System

The needles are powered with high voltage DC signal supply system (including a TREK Model 30/20A High-Voltage Power Amplifier and a Tektronix Model AFG3022B arbitrary waveform generator) and the plate electrodes are grounded. The DC signal used here is continuous with constant amplitude. Electrical parameters were measured using an oscilloscope (Tektronix DPO2014) and a digital multi-meter (BK Precision 5491A). DC Voltage was measured using a passive probe (Tektronix Model P6015A) with an attenuation of 1000× through the oscilloscope. The frequency response of the probe is DC to 75 MHz and this probe can be used to measure DC voltages up to 20 kV or peak AC voltages of 40 kV with a rated accuracy of ± 3%. The input impedance characteristics of the probe, as rated, are 100 MΩ and ⩽3 pF (when compensated properly). The oscilloscope has a maximum sampling rate of 1 GSa/s at a bandwidth of 100 MHz. The range of voltages used in the power and efficiency study is from 6 kV to 12 kV. The digital multi-meter of 1 mV resolution was used to measure the potential difference across a 1 MΩ resistor connected in series with the actuator. This potential difference can be converted to current with an equivalent resolution of 1 nA.

4.1.4 Thermal Measurement

Before the thermal measurements, experimental conditions, including ambient temperature and relative humidity, were monitored continuously using a humidity and temperature recorder (EXTECH Instruments RH 520). The probe of the recorder

Two kinds of methods were used to measure the surface temperature of the rubber heater. In the first method thermocouples were attached on the surface of the rubber heater to give a brief understanding of cooling performance of the designed actuators. On the other hand, the second method employs an IR camera to obtain spatial temperature data on the simulated CPU chip (rubber heater) adjacent to the grounded plate electrode.

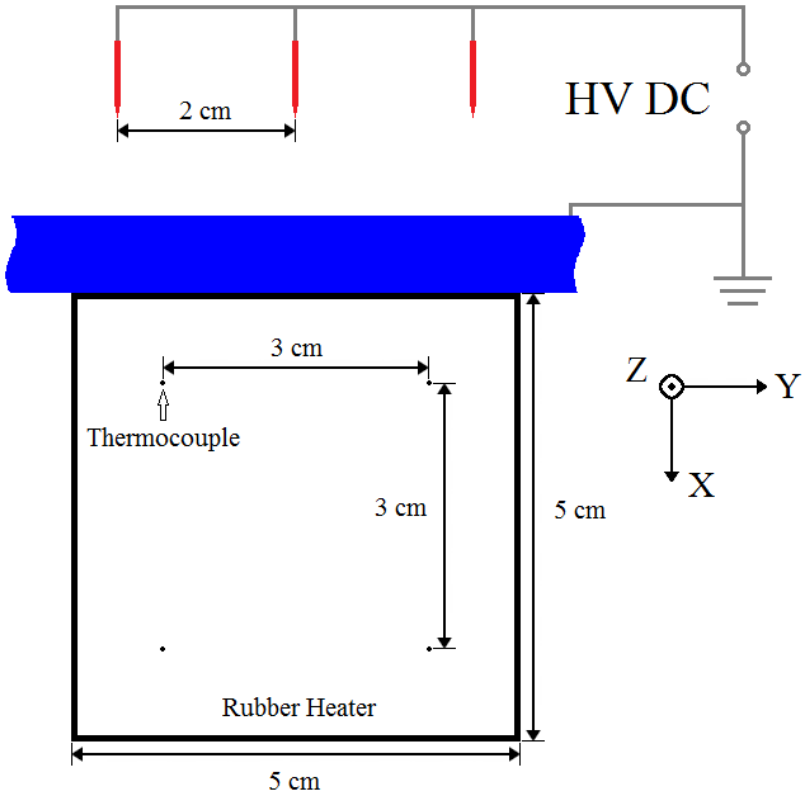

Figure 4-6. Top view of the thermocouple locations on the rubber heater for the first method of thermal measurement (not to scale).

For the first method, measurements of thermocouples were monitored by a LabVIEW code and were showed lively on the computer screen. As shown in Figure 4-6, three needles separated by a span-wise distance of $2\ \mathrm{cm}$ were placed at height $h = 2.5\ \mathrm{mm}$ with stream-wise gap $g = 15\ \mathrm{mm}$. At room temperature $21\ ℃$, one rubber coated resistant heater (24V, 12W with surface area $5 \times 5\ cm^2$) placed adjacent to the plate electrode was used as a heating source simulating an CPU chip during the test. Four T-type thermocouples were placed on the corners of a $3 \times 3\ cm^2$ inner square beginning from 1 cm downstream of the plate electrode. Time varying temperature data were obtained from the average of all four thermocouples representing the average surface temperature.

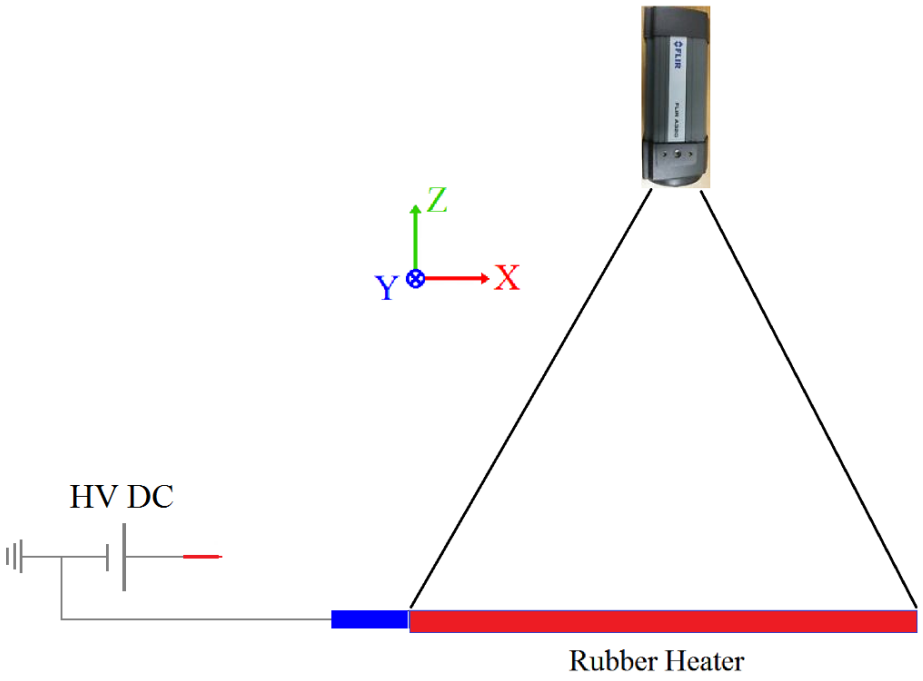

Figure 4-7. IR camera setup above the rubber heater for the second thermal measurement method of the surface cooling test (not to scale).

To further understand the cooling performance of the designed actuators, spatial temperature distribution on the simulated CPU chip (rubber heater) will be obtained from IR camera. Figure 4-7 displays the design of the IR temperature measurement setup. IR camera (FLIR A325) is located 20 cm above the rubber heater to collect the IR emission of the heater. Meanwhile, the flat surface of the rubber was painted with Krylon Ultra Flat Black Spray 1602, which has a known emissivity of 0.96 (National Aeronautics and Space Administration, 2003), to ensure accurate IR readings. Then, the accuracy of the camera was assessed to be ±1 °C over the range of 25–80 °C during calibration process using thermocouples. Thus, stabilized surface temperature distribution can be obtained from this measurement to study the cooling performance at different locations. With the surface temperature data from IR camera, the distribution of convection coefficient on the surface and the relationship between convection coefficient and velocity at the same location also can be investigated.

4.1.5 Velocity Measurement

The same PIV system used in Chapter three was also employed in the cooling performance study. PIV system was employed to examine the flow field in the cooling region over the rubber heater. By obtaining the flow velocity distribution near the hot surface, detailed study on the forced convection was performed. XY-plane and YZ-plane velocity field was captured because it can give information on the cooling area that covered by the actuator as well as whether the 2 cm needle space can sustain uniform flow in the area between two adjacent needles.

4.2 Result and Discussion

In the cooling performance test, several important parameters were chosen to study their influence. The location of the needle was adjusted to get the optimal cooling

performance. High voltage DC signals with different voltages and both polarity were applied to the needle. Various radius of curvature of the steel needle tip was also investigated on its influence on both flow velocity field and cooling performance.

Unlike other plasma based flow inducement, the needle actuated channels can generate sufficient amount of flow with very low power consumption. This suggests that much less power is wasted in heat generation. So, this makes it a perfectly suitable as a convective cooling device. We demonstrate this cooling capability using a plate-needle configuration with three needles. A rubber heater was powered by a 8 V DC signal placed adjacent to the plate electrode with a surface heat flux of $q" = 533\ \mathrm{W/m^2}$. The upstream ambient air temperature was maintained as $T_\infty = 21\ ℃$ with relative humidity of 64 % to 66 % during the and the average surface temperature under free convection was $T_s = 62\ ℃$. Then the free convection coefficient can be calculated as $h = 13\ \mathrm{W/(m^2 \cdot K)}$ by using equation:

$$q" = h(T_s - T_\infty) \tag{4-1}$$

Time varying temperature curve for cooling effects are shown in Figure 4-8. The convection coefficients under needle actuation were $15.2, 18.1 \text{ and } 20.5\ \mathrm{W/(m^2 \cdot K)}$ with the applied voltage of 6, 9, 12 kV. At positive 12 kV, needle actuation can cool a $3 \times 3\ \mathrm{cm^2}$ area from $62\ ℃$ to $47\ ℃$ within $80\ \mathrm{s}$. In the meantime, the total power of three needles for each voltage applied shown in the legend of Figure 4-8 remains at miliwatts level which demonstrate great potential of needle actuation device for cooling application.

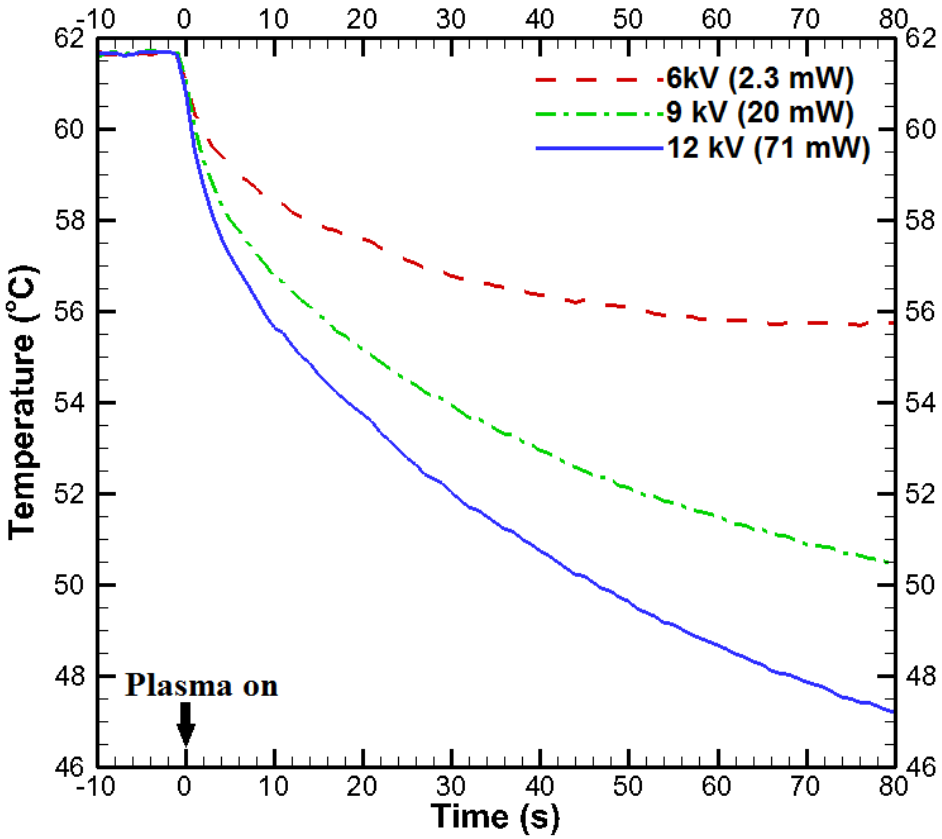

Figure 4-8. Cooling effect of needle actuation device setup (total power consumed by all three needles shown in legend).

In order to further understand the cooling performance with surface temperature images captured by IR camera, local temperature drop and local enhancement factor of heat convection coefficient between natural convection and forced convection with needle actuator were both used. Since the input power of rubber heater was maintained during the experiment, the relation between natural convection confident and forced convection confident can be write as

$$q" = h_n(T_n - T_\infty) = h_f(T_f - T_\infty). \quad (4\text{-}2)$$

Thus, one can further calculated the enhancement factor of the local heat convection coefficient from Equation 4-2,

$$\frac{h_f}{h_n} = \frac{(T_n - T_\infty)}{(T_f - T_\infty)}. \quad (4\text{-}3)$$

Similarly, average heat convection enhancement factor can be calculated to represent the overall cooling performance of the actuator for each case.

$$\frac{\overline{h_f}}{\overline{h_n}} = \frac{(\overline{T_n} - T_\infty)}{(\overline{T_f} - T_\infty)}. \quad (4\text{-}4)$$

4.2.1 Voltage and Polarity Study

In this section, effects of voltage and polarity were investigated on the cooling performance of the single needle actuators. The needle was placed in the upstream of the ground electrode with gap, g = 15 mm, and height, h = 3 mm. Inside the testing chamber, the ambient temperature was maintained as $T_\infty = 21$ ℃ with relative humidity from 64 % to 66 %. With both positive and negative polarity of the input signal, the voltages were set as 6 kV, 8kV, 10 kV and 12 kV. PIV study on the XY-plane and XZ-plane as well as the IR surface temperature study were performed.

XZ-plane PIV images on varying positive voltage magnitudes with stream-wise direction (positive X direction) velocity profiles are shown in Figure 4-9. XZ-plane PIV profiles were recorded in the center plane (Y = 0 mm) of the needle actuator. These images suggest that the needle actuator can generate higher flow velocity with higher magnitude of voltage. However, with voltage higher than 8 kV, velocity profiles show hump shape before the plate ground electrode, which starts at X = 15 mm and ends at X = 20 mm. This hump shape velocity profile lifts the wall jet driven from the needle tip and then hits the surface at the beginning of the rubber heater.

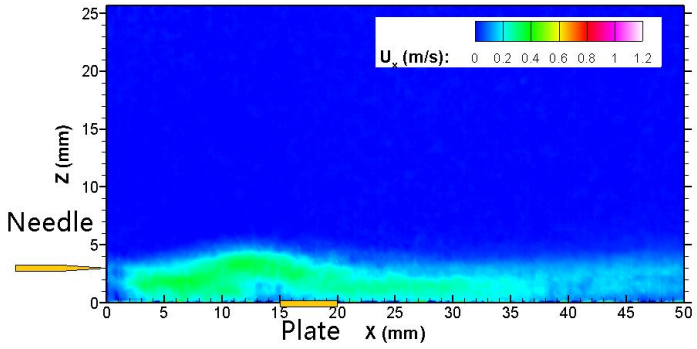

A

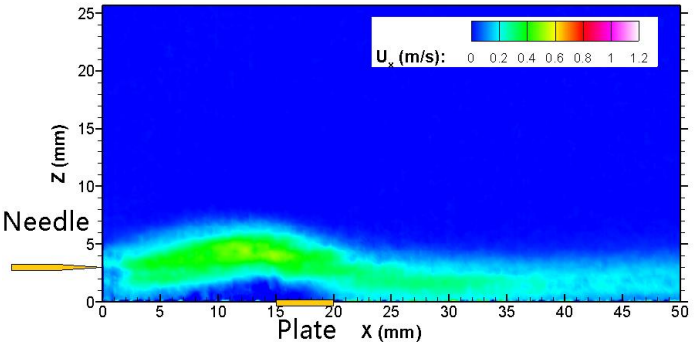

B

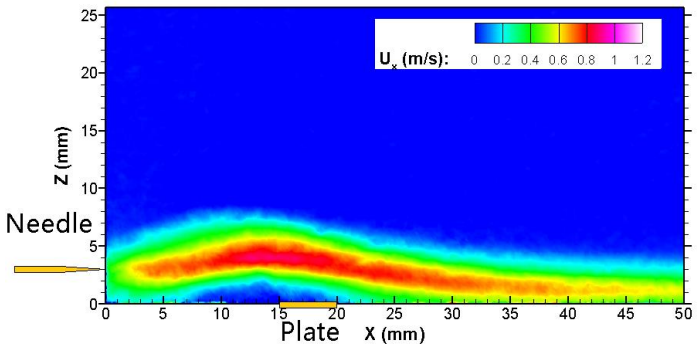

C

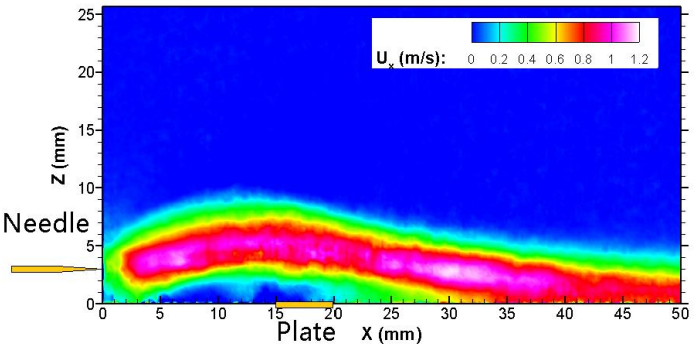

D

Figure 4-9. XZ-plane X direction velocity profile (Y = 10 mm) of a single needle actuator. A) Positive 6 kV. B) Positive 8 kV. C) Positive 10 kV. D) Positive 12 kV.

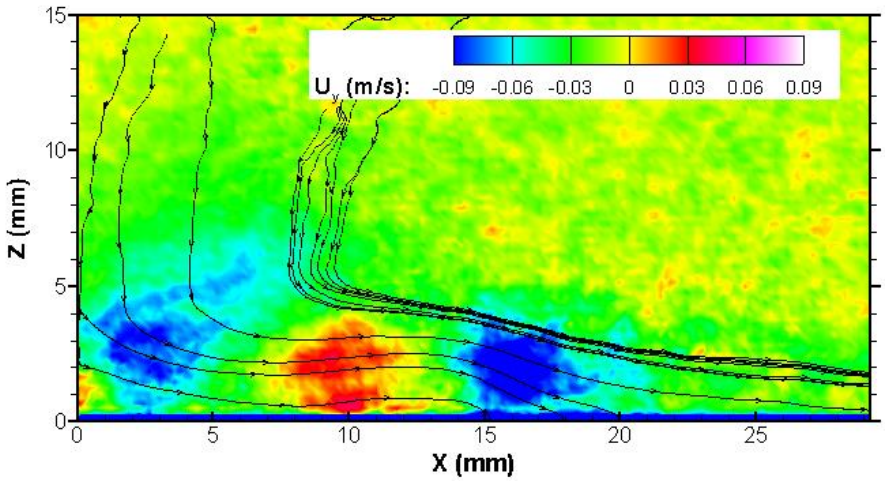

A

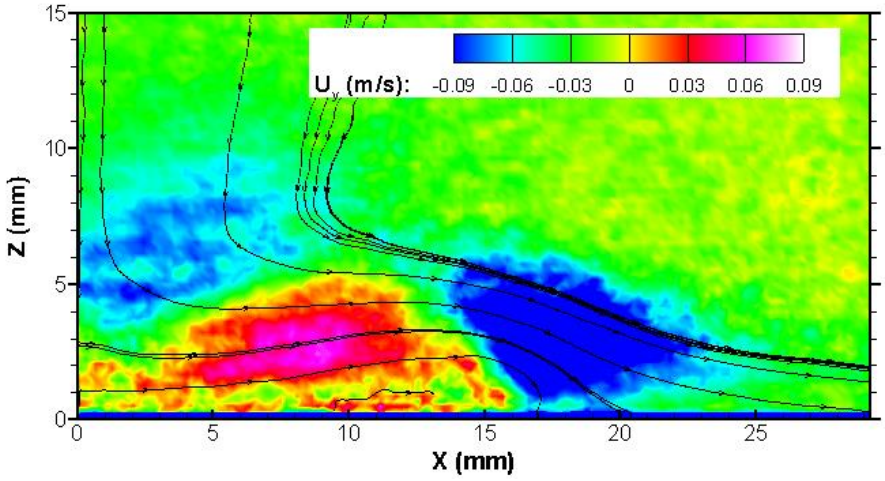

B

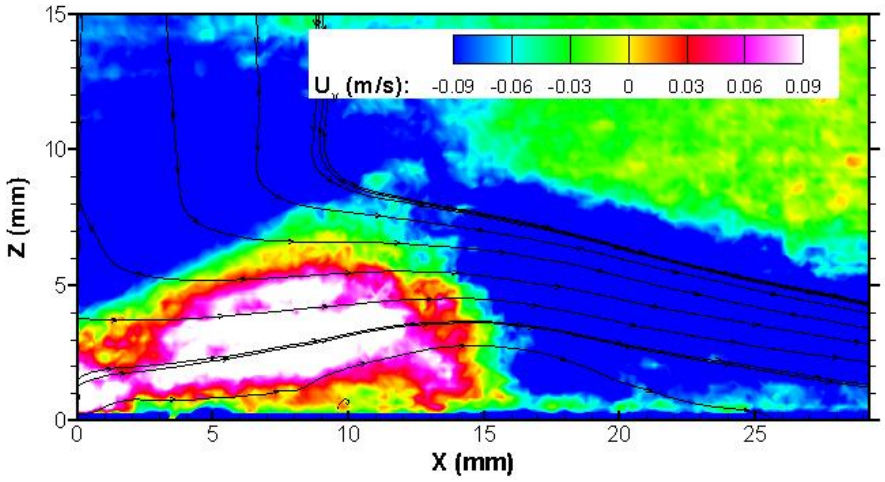

C

Figure 4-10. XZ-plane Z direction velocity profile (Y = 10 mm) of a single needle actuator. A) Positive 6 kV. B) Positive 8 kV. C) Positive 10 kV.

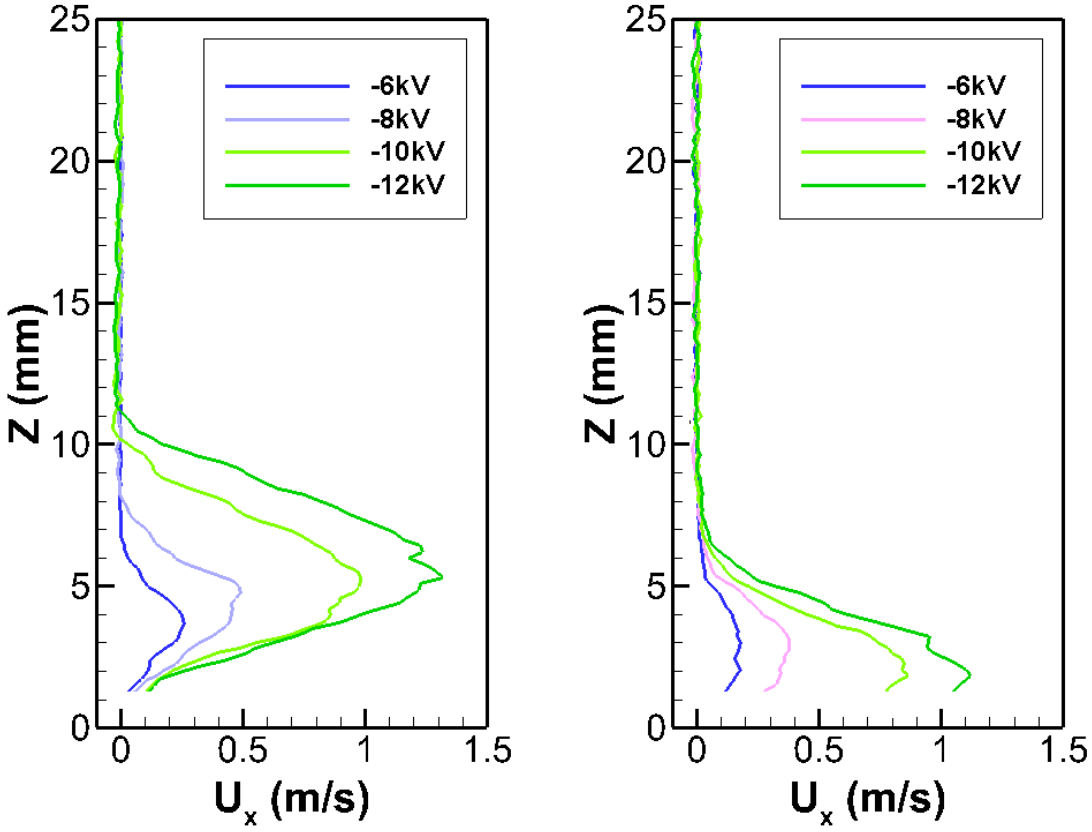

Figure 4-11. X direction Velocity profile with negative DC signal powered on needle. A) At the edge of the rubber heater (X = 20 mm). B) At middle of the rubber heater (X = 40 mm).

To further analyze the hump, Z direction velocity profiles were also shown in Figure 4-10. The red region represents upward flow and blue region represents downward flow. There were clear signs that beginning of the grounded electrode (X = -5 mm) is the separation interface of opposite direction flow. One possible reason for this phenomenon is that after the corona discharge ignites, ions are driven by the electric field between the needle tip and the grounded electrode. During this process, some ions will be accumulated on the surface the dielectric material before reach the grounded electrodes. Then, these accumulated ions will repulse the ions came from the needle to

form a hump. Meanwhile, the grounded electrode maintains at zero potential attracting ions towards its surface.

To further analyze the effect of the voltage magnitude and polarity of the high voltage DC signal, Figure 4-11 and Figure 4-12 show the X direction velocity profiles of the surface cooling system at X = 0 mm and X = 20 mm. In each individual figure, velocity profiles are driven by 4 different voltages from 6 kV to 12 kV. These velocity profiles are typical Glauert wall jet profiles.

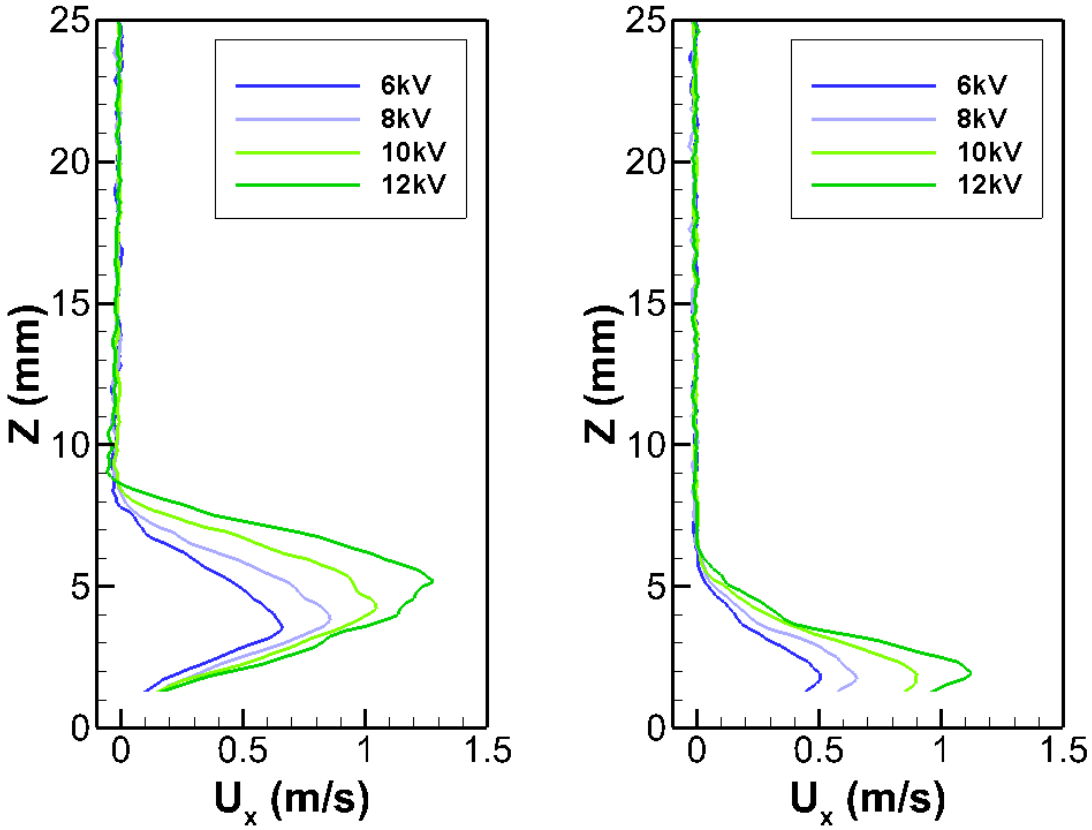

Figure 4-12. X direction Velocity profile with Positive DC signal powered on needle. A) At the edge of the rubber heater (X = 20 mm). B) At middle of the rubber heater (X = 40 mm).

Due to the existence of the hump in velocity profile, at the beginning of the rubber heater (X = 20 mm), the wall jet profile is barely attach to the surface of the heater with about 1 mm zero velocity space above the heater (Figure 4-11A, Figure 4-12A). However, after developing through the heater surface, the wall jet profiles finally attached with the heater surface at the middle of the heater (X = 40 mm) as displayed in Figure 4-11B and Figure 4-12B.

Furthermore, in both positive and negative cases, needle actuator shows increasing velocity with increasing voltage magnitude. Similar to the channel needle actuator described in chapter 3, under negative signal, the velocity profile increase faster than that under positive signal. This may be due to the different discharge mechanisms of positive or negative corona discharge. For negative signal, while voltage magnitude increases, the number of electrons emitted from the discharge region near the needle tip increase much faster than the increment of the positive ions under positive signal. This fast growth in electron emission will lead to the growth of negative ions through electron attachment process.

Comparison of the Glauert wall jet profiles between positive and negative 10 kV cases are displayed in Figure 4-13. At both locations, the profiles from two cases are almost identical. Unlike the channel needle actuator described in chapter 3, in the plate needle actuator, electric field is generated between the needle and the flat grounded electrode. Subsequentially, the ions generated under either positive signal or negative signal will be driven towards the surface of the grounded electrode. So, no difference was shown in this comparison. Thus, no polarity analyze is need in the following studies.

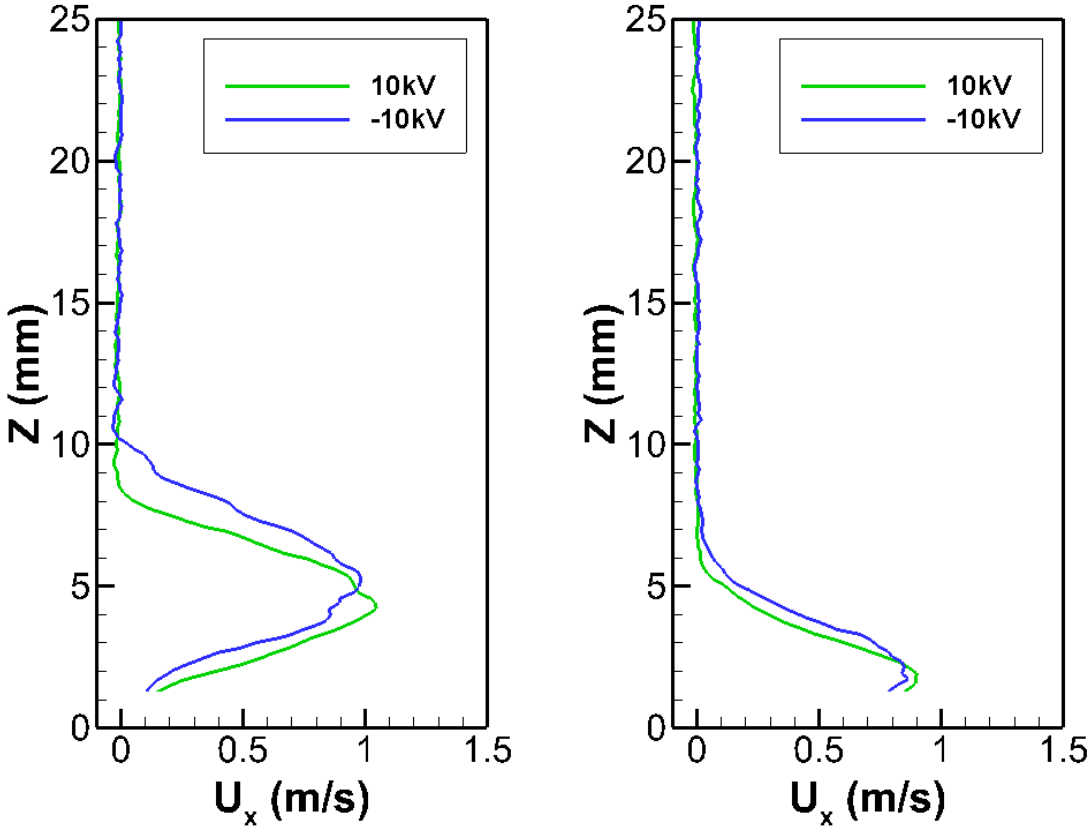

Figure 4-13. Comparison of the X direction velocity profile between positive and negative DC signal powered on the needle. A) At the edge of the rubber heater (X = 20 mm). B) At middle of the rubber heater (X = 40 mm).

While the velocity is increasing with voltage magnitude increment, the cooling performance should be better with higher magnitude of voltage. To examine this, XY-plane PIV images were also captured to analyze the velocity distribution on the heater surface. The PIV plane was set 1 to 2 mm above the heater surface. And the images were only covers the rubber heater, which is the region of interest on cooling performance test.

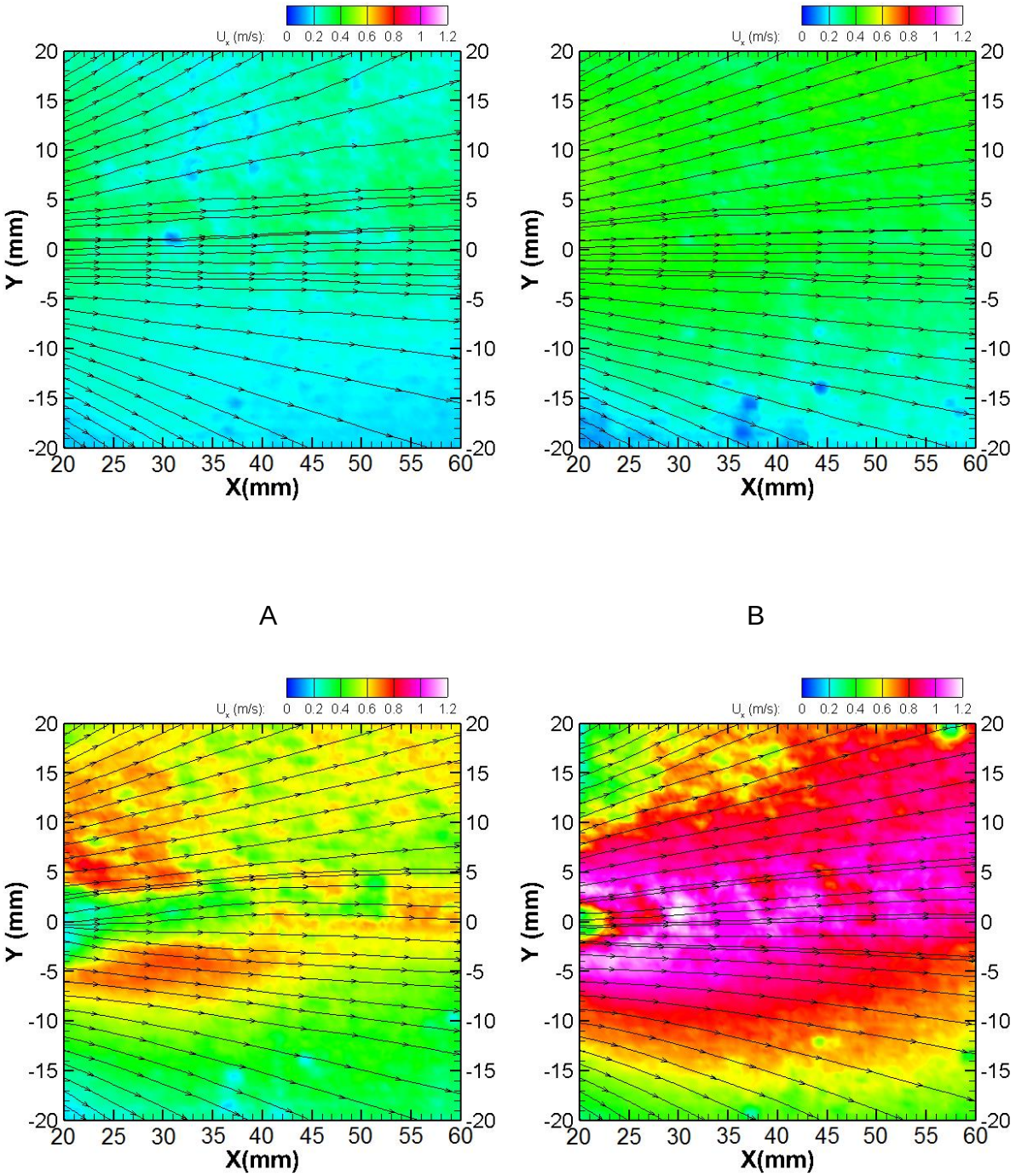

Figure 4-14. XY-plane X direction velocity profile (Z = 2 mm) of a single needle actuator. A) Positive 6 kV. B) Positive 8 kV. C) Positive 10 kV. D) Positive 12 kV.

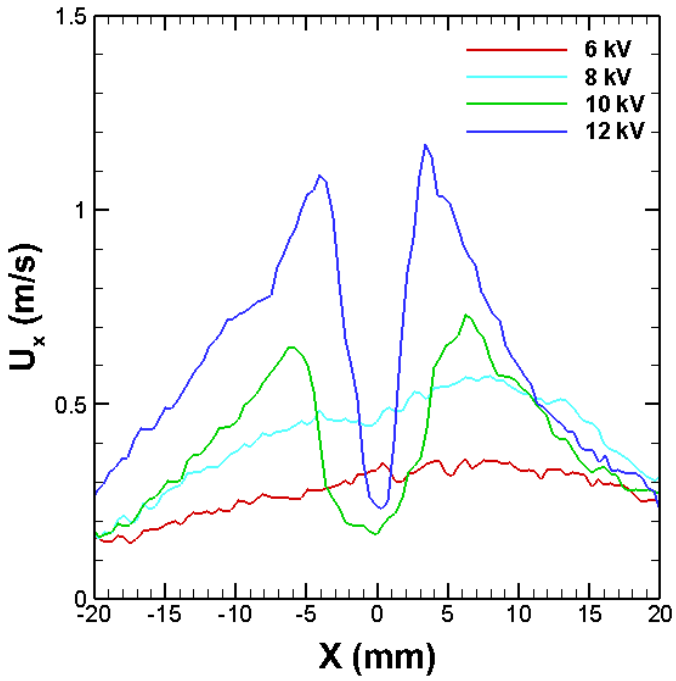

A

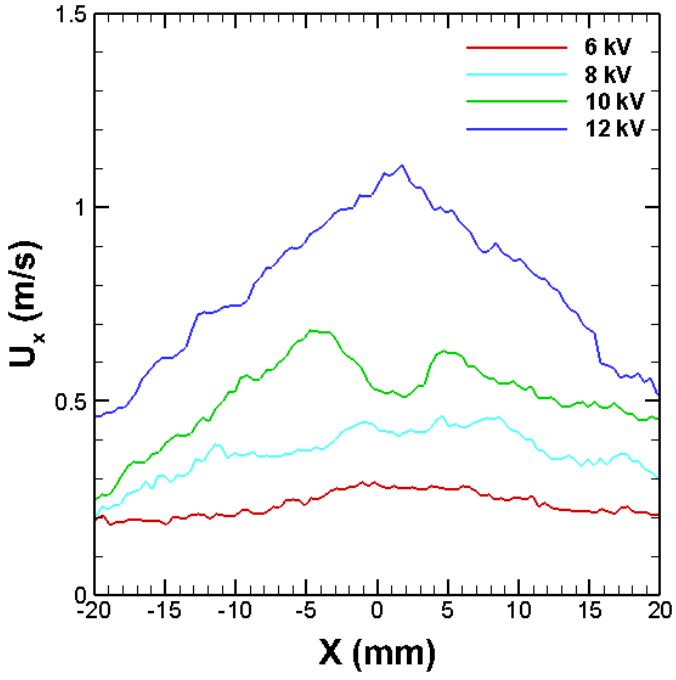

B

Figure 4-15. X direction Velocity profile with Positive DC signal powered on needle. A) At the edge of the rubber heater (X = 20 mm). B) At middle of the rubber heater (X = 40 mm).

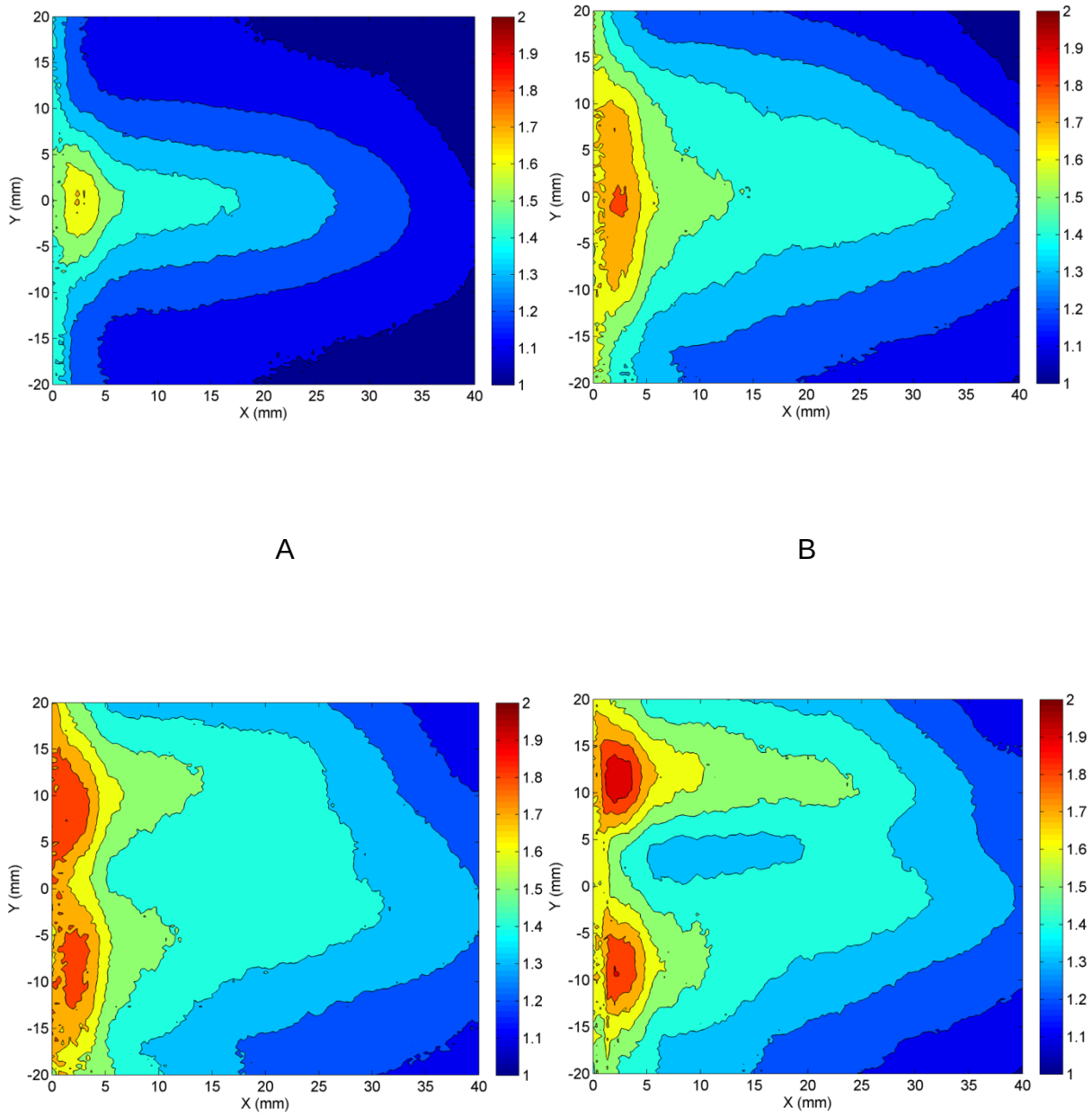

Figure 4-16. Distribution of the enhancement factor of the local heat convection coefficient over the rubber heater with different voltage magnitude. A) Positive 6 kV. B) Positive 8 kV. C) Positive 10 kV. D) Positive 12 kV.

The average heat convection enhancement factors calculated using Eq. (4.4) for different voltages and polarities are displayed in Figure 4-17. With the voltage magnitude larger than 10 kV, actuator with negative signal showed slight better cooling performance. However the power consumption of the negative corona actuator is about twice of that for positive corona actuator. In both polarity cases, the maximum speed reaches about 1.2 m/s between X = 5 mm and X = 10 mm, which indicates that the flow is keep accelerating after the grounded flat electrode.

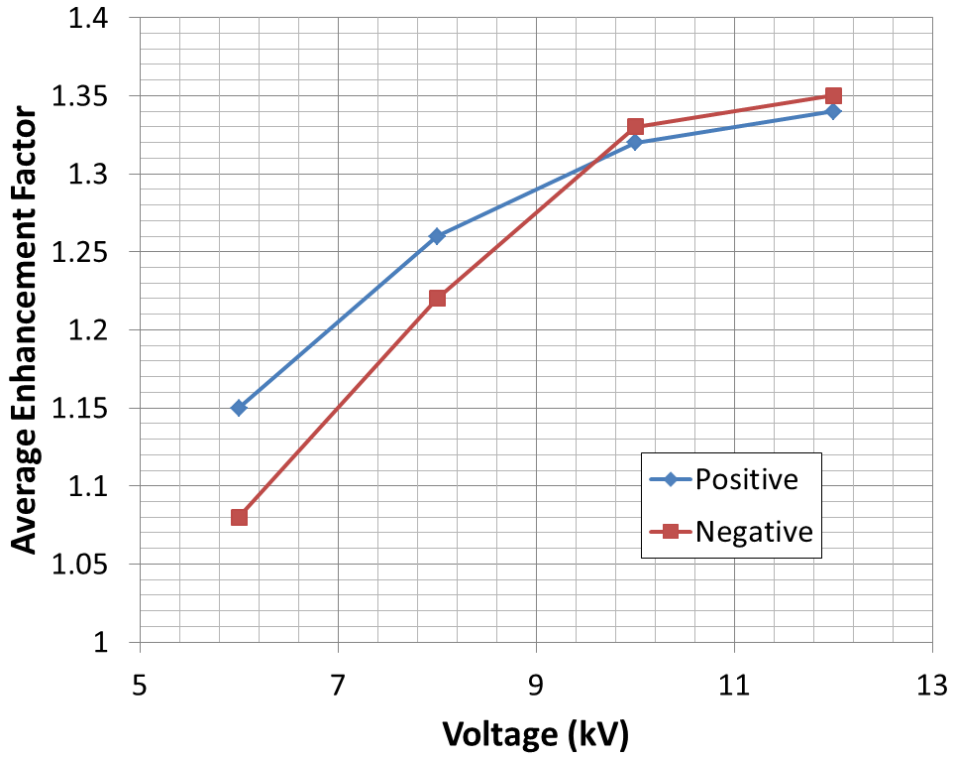

Figure 4-17. Average ehancement factor as function of applied voltage and polarity.

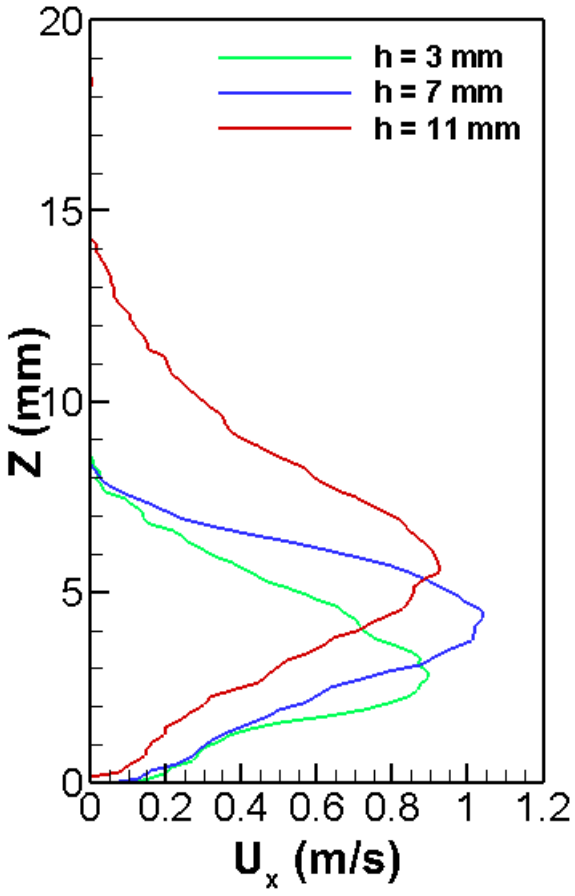

Figure 4-18. Comparison of the X direction velocity profile between different height of the needle.

4.2.2 Needle Height Study

Height of a single needle in the actuator was varied from 3 mm to 11 mm above the heated surface. Velocity profiles at the edge of the heater for selected needle height are shown in Figure 4-18. All case were operated under positive 10 kV DC input signal. The results suggest that highest velocity is generated with needle height equals to 7 mm.

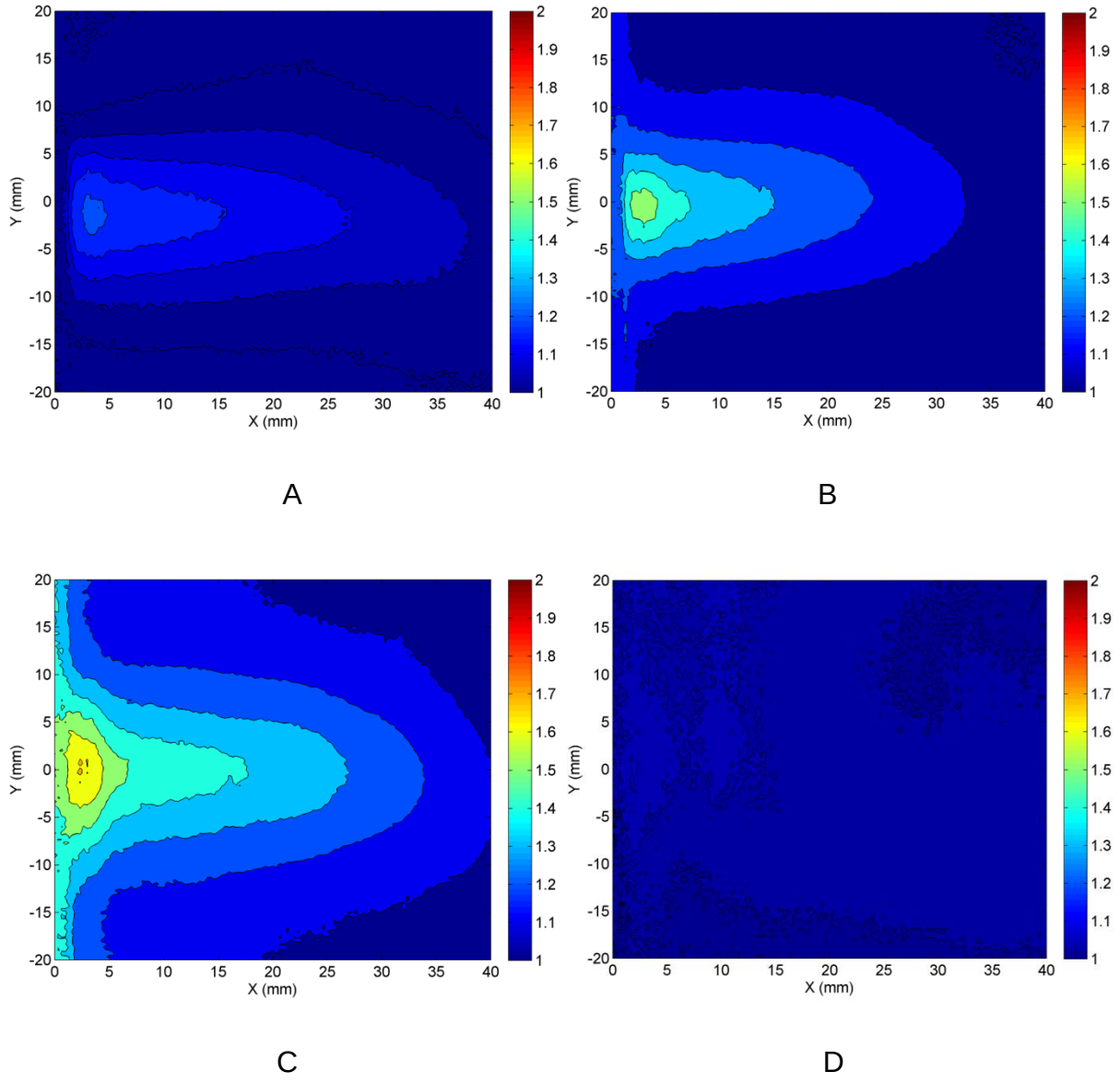

Figure 4-19. Distribution of the enhancement factor of the local heat convection coefficient over the rubber heater at 6kV with different needle height. A) h = 3mm. B) h = 5mm. C) h = 7mm. D) h = 9mm.

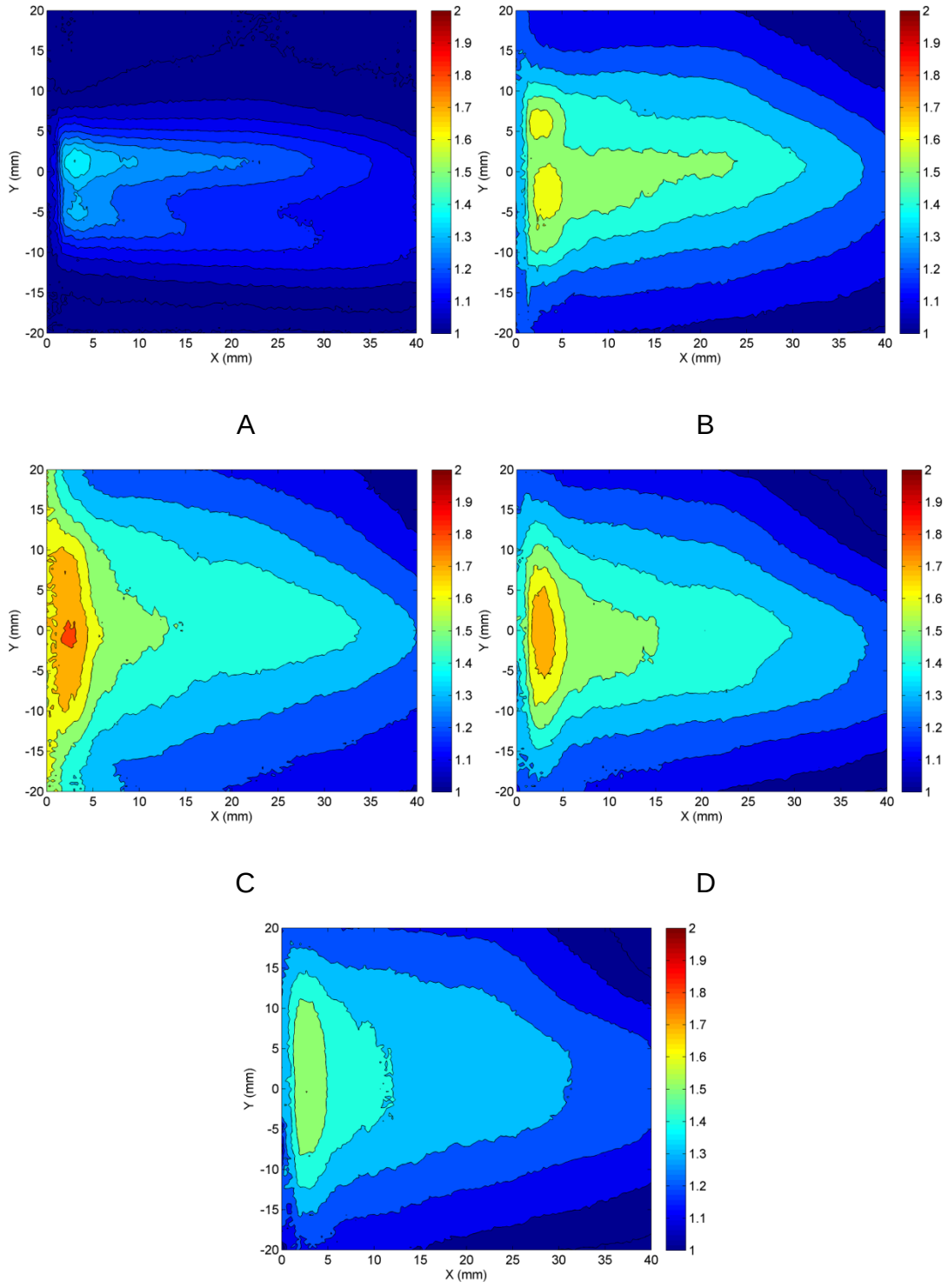

Figure 4-20. Distribution of the enhancement factor of the local heat convection coefficient over the rubber heater at 8kV with different needle height. A) h = 3mm. B) h = 5mm. C) h = 7mm. D) h = 9mm. E) h = 11 mm.

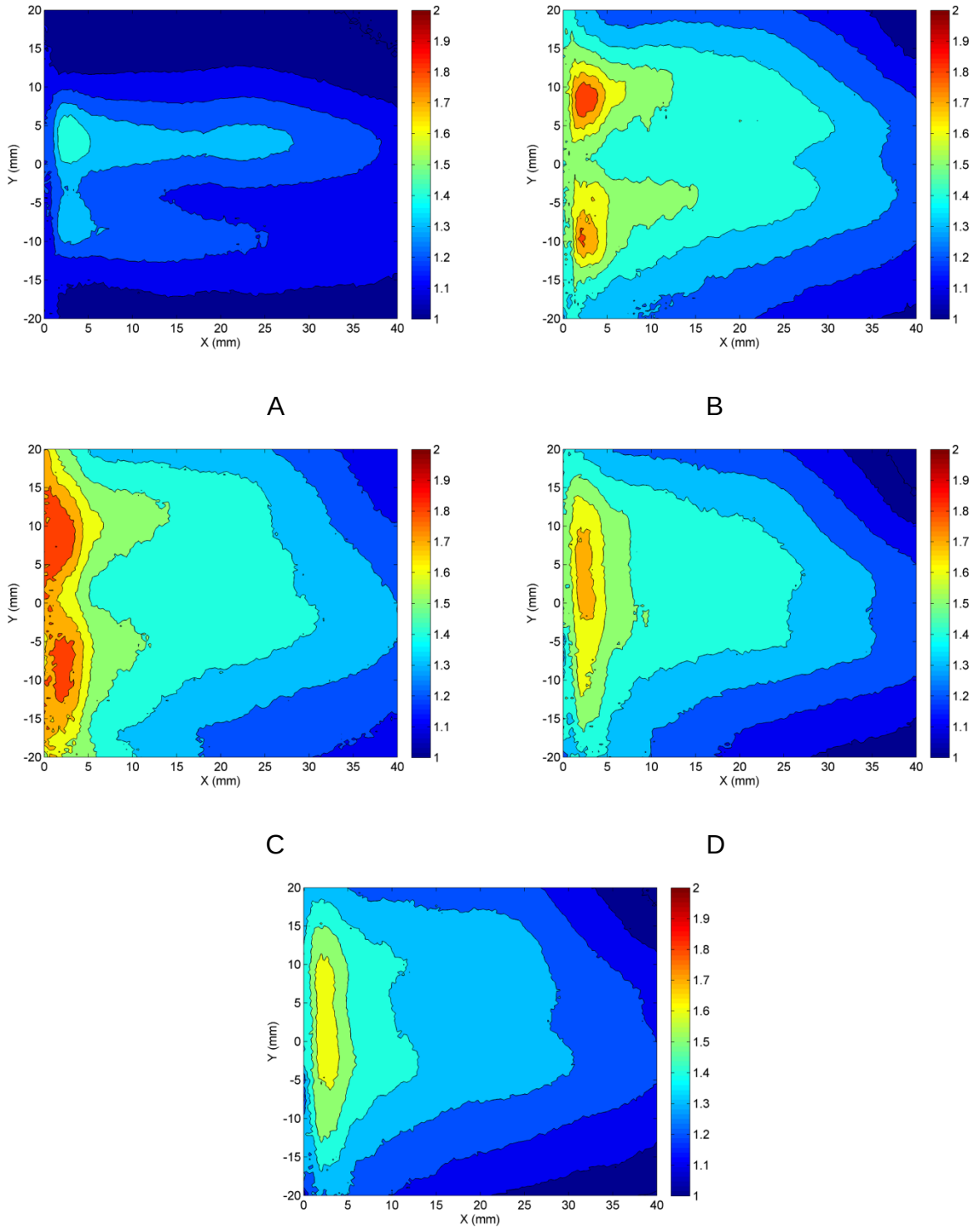

Figure 4-21. Distribution of the enhancement factor of the local heat convection coefficient over the rubber heater at 10kV with different needle height. A) h = 3mm. B) h = 5mm. C) h = 7mm. D) h = 9mm. E) h = 11 mm.

Distributions of local heat convection enhancement factor are shown in Figure 4-19 to Figure 4-21. Results suggest that when needle is placed at 7 mm, the cooling effects of the needle actuator reaches maximum for voltage from 6 kV to 10 kV. In the cases that needle placed in higher or lower locations, maximum flow velocity was limited by the geometry.

As shown in the enhancement factor distribution figures (Figure 4-19 to 4-21), the hump effect also affected the cooling performance of the actuator. With the lower needle height, the hump effect starts with lower applied voltage. The possible reason is that when the needle is closer to the dielectric surface, it is easier to accumulate the charge on the surface.

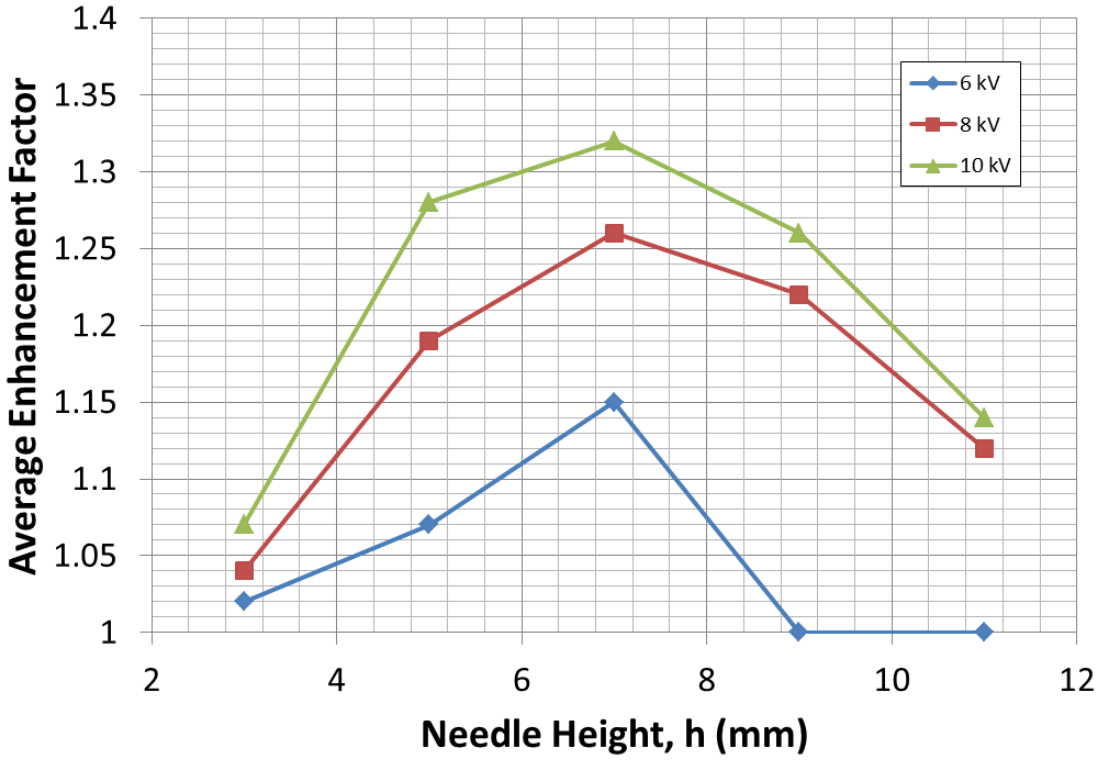

Figure 4-22. Average ehancement factor as function of needle height and applied volatge magnitude.

Figure 4-22 shows the entire average heat convection enhancement factors in the needle height study. It clearly shows that for the cases studied 7 mm is the best needle height for cooling using needle plate actuators.

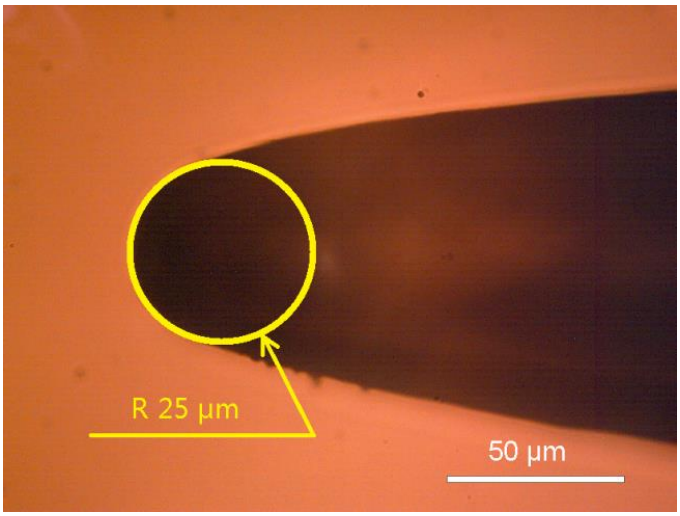

A

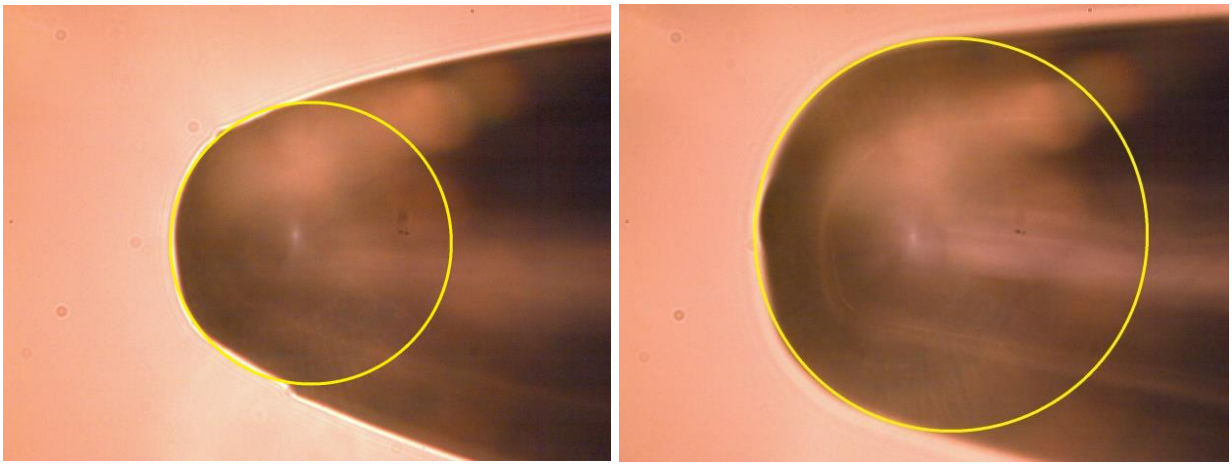

B C

Figure 4-23. Radius of curvature estimation with microscopic pictures. A) ~25 µm needle tip. B) ~45 µm needle tip. C) ~60 µm needle tip.

4.2.3 Radius of Curvature Study

Radius of curvature of needle tip was tested with three different size of the needle from 25 µm to 60 µm. As shown in Figure 4-23, radius of curvature of needle tips

were estimated using microscopic pictures and the reference length. In all three cases, the applied DC signal was maintained at 10 kV.

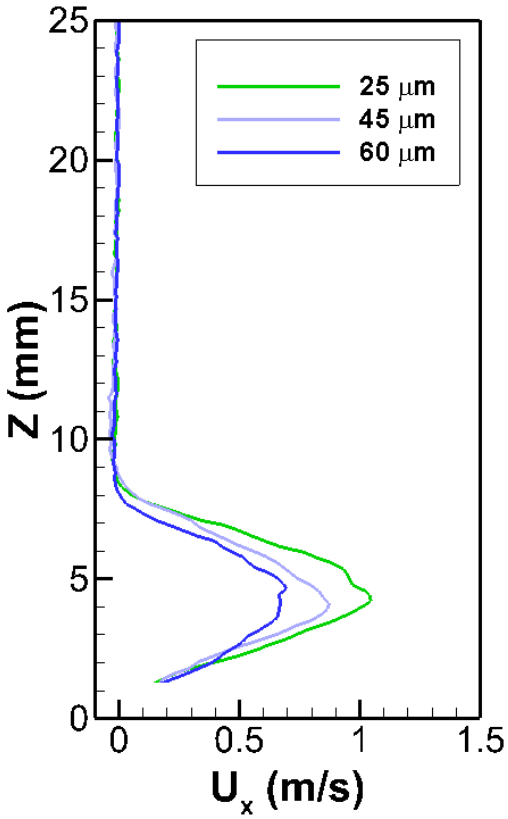

Figure 4-24. Comparison of the X direction velocity profile between different radius of curvature of the needle.

As displayed in Figure 4-25, temperature drop result indicates smaller radius of curvature leads to stronger cooling effect as well as the power consumption. Similar trend was observed by Leonov's group on electrode with small sharp tip (Leonov, Opaits, Miles, & Soloviev, 2010). This is due to the fact that high potential conductor with a smaller radius of curvature will have stronger E-field. With stronger E-field, more ions will be generated. Thus higher electric body force will be provide to the bulk ions, resulting in a faster wall jet.

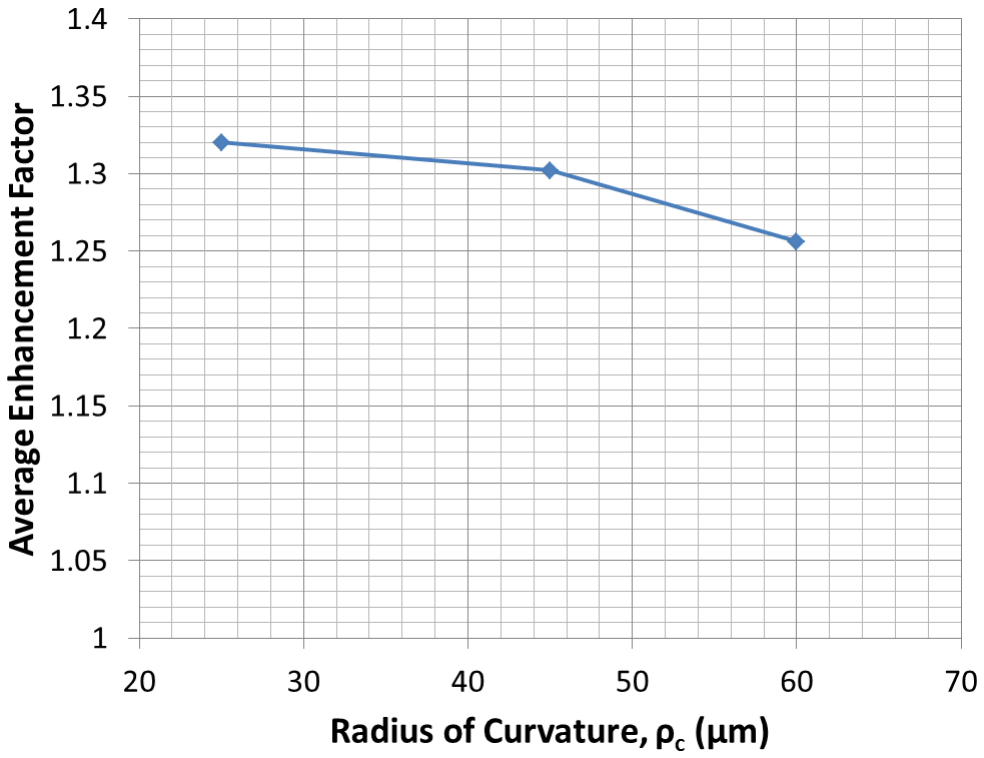

Figure 4-25. Average ehancement factor as function of radius of curvature of the needle tip.

4.3 Summary of Surface Cooling Study

The cooling effect using multi-needle plate configuration was investigated. The preliminary results on cooling effects shows that needle actuation device can reduces the temperature of a hot area by 15 ℃ using only miliwatts level energy within 80 s. This suggests that the needle actuation can efficiently enhance heat transfer near hot surface.

Voltage magnitude and polarity study suggests that the needle actuator can generates higher flow velocity with higher magnitude of voltage. Subsequently, the cooling performance is better with higher magnitude of voltage. With the same voltage magnitude, actuator with negative signal showed slight better cooling performance as well as twice of the power consumption.

Height of a single needle in the actuator was varied from 2 mm to 12 mm above the heated surface. Result suggests when needle is placed at 6 mm, the cooling effects of the actuator reaches maximum for voltage from 6 kV to 10 kV. In the cases that needle placed in higher or lower locations, flow velocity was limited by the geometry.

Radius of curvature of needle tip was tested with 3 different size of the needle from 25 μm to 60 μm. Result indicates smaller radius of curvature leads to stronger cooling effect as well as the power consumption.

CHAPTER 5
VORTICES GENERATION USING EFFICIENT PLASMA ACTUATORS

As a method of introducing perturbations for low speed flow control, plasma actuators present themselves as a useful tool (Corke, Enloe, & Wilkinson, 2010). This type of plasma actuator has shown itself to be effective for boundary layer control (J. R. Roth, Sherman, & Wilkinson, 2000; Visbal, 2010) and for flow reattachment at low to moderate Reynolds numbers (Rizzetta & Visbal, 2010; Schatzman & Thomas, 2010), especially when used in a pulsed manner.

Plasma actuators with novel geometries, including the serpentine geometry with DBD actuators, have been effective in a number of numerical studies (Rizzetta & Visbal, 2011; Wang, Durscher, & Roy, 2011) as well as some experimental work (R. J. Durscher & S. Roy, 2012; Santhanakrishnan & Jacob, 2007). Specifically, the serpentine geometry actuators are able to introduce streamwise, as well as spanwise and surface normal vorticity to and promote increased mixing in the flow. The manner that three-dimensional perturbations can be introduced to the flow allows for an additional freedom when designing and implementing control. This additional degree of freedom may allow for greater control authority.

Due to the benefit of generating vorticities on active flow control, efficient corona based plasma actuator is further developed to generate vorticies in this section. The primary goal of this study is to generate controllable vorticies using milliwatt level power.

5.1 Experiment Setup

5.1.1 Electrode Configuration Design

The configuration for the plate configuration is shown in Figure 5-1. In this, an array of high voltage steel needles is placed in the upstream side of the plate electrode.

Such arrangement should allow airflow driven by the corona discharge from the needle tip to the plate with either positive or negative DC signals. Since this configuration will generate 3D flow structures, a particular arrangement of multiple needles is then employed to generate three-dimensional vortical structures.

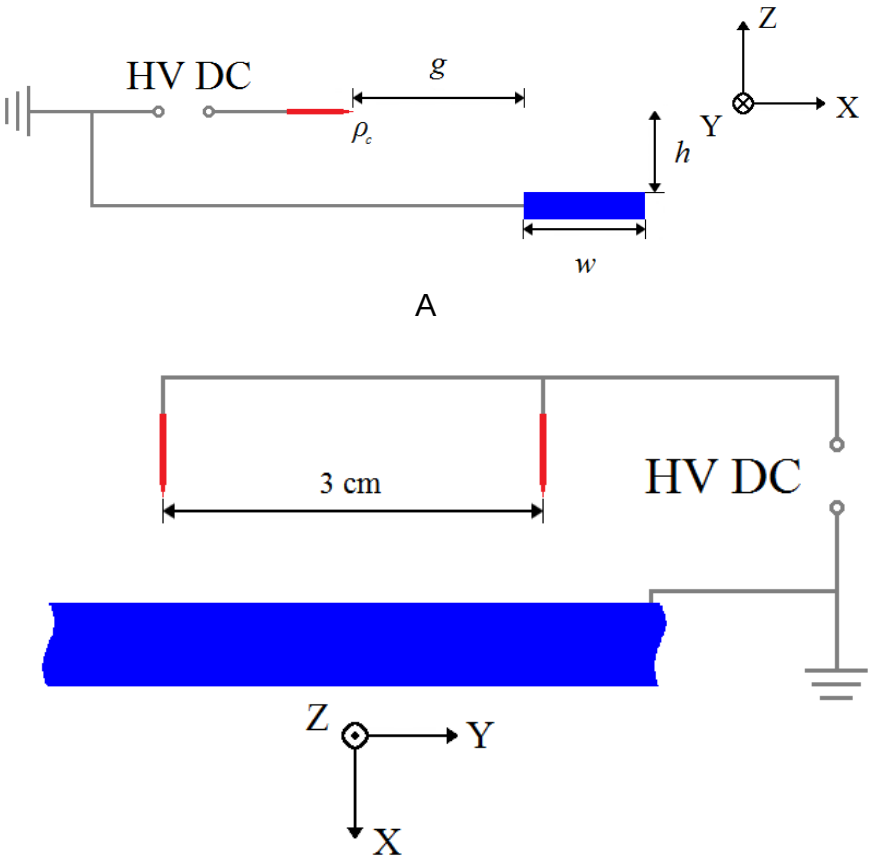

Figure 5-1. Electrodes configuration for surface cooling effect. A) Side view. B) Top view.

Detailed description of dimensions and experiment setup are shown in Figure 5-1 and described below. Powered needles and plate electrodes are separated by gap g in x-direction and height h in z-direction. And the width of plate electrode denotes as w in the configuration. In all test cases, y-direction (span-wise) length of plate electrodes is

set to be $10\ \mathrm{cm}$. All needles used in this letter have a nominal radius of curvature $\rho_c = 50\ \mu\mathrm{m}$, and all plate electrodes are 60 μm thick and $5\mathrm{mm}$ wide ($w = 5\ \mathrm{mm}$). Also in all cases *h* = 2.5 mm.

5.1.2 Testing Environment

The needles are powered with high voltage DC supply (TREK Model 30/20A High-Voltage Power Amplifier) and the plate electrodes are grounded. The DC signal used here is continuous with constant amplitude.

As previously mentioned, we used multiple configurations of needle-plate actuation to investigate their performances for various applications. Controllable vortical structure is created using plate configuration (Figure 5-1) with two needles. In vortex generation case, two needles at span-wise distance of 3 cm were placed at the same height $h = 2.5\ \mathrm{mm}$ with gap $g = 15\ \mathrm{mm}$. In order to control the direction of the vortex, the applied DC signals of these two needles are kept slightly different (described in section 5.2).

5.2 Result and Discussion

Needle actuation device may also be used to induce flow vortices near the surface. Two cases were studied by applying slightly different signals on two span0wise displaced needle electrodes. We managed to generate a counter-rotating vortex pair between the two needles for which the strength and direction of the majority vortex can be controlled. As displayed in the inlay in Figure 5-2A, needle 1 powered with 10 kV DC signal and needle 2 powered with 8 kV DC signal were separated by a distance $d = 30\ \mathrm{mm}$. After powering both needles, a counter-clockwise vortex with maximum X-vorticity greater than 300 s^{-1} was captured using PIV system at YZ-plane with X = 10 mm. Note that the airflow generated by needle 1 is stronger near the wall so that it

pushes the airflow generated by needle 2 and then forms a counter-clockwise vortex near the wall. For case 2 shown in Figure 5-2B, the needle 2 at Y = 15 mm was powered with 10kV DC signal which is higher than the 8 kV DC signal applied on needle 1 at Y = -15 mm. Stronger airflow near surface was generated near the needle 2 side. Then, the major vortex generated was clockwise under this condition. Furthermore, the power used to generate the vortex pair was only 12 mW in total. Such low power vortical flow perturbation may be quite beneficial for drag reduction, flow mixing and many other flow control applications (Riherd & Roy, 2013).

5.3 Application on Surface Cooling

As demonstrated in the previous section, vortices can be generated between two needles with different voltage. These vortices will increase the mixture of the cold air on top and hot air on the heater. Thus, it may also be used in enhancing surface cooling applications. In this section, two parameters were investigated: number of needles used in the actuation device and voltage difference between 2 needles.

5.3.1 Experiment Setup

Figure 5-3 shows the needle configuration of the needle number study. With single needle, the needle was placed in the center position. In the Double needle case, two needles were separated by 20 mm. Triple needle case were the combination of the single needle case and double needle case.

The voltage difference study was performed on double needle configuration as shown in Figure 5-3B. Three cases were tested with voltage pairs (8 kV, 8 kV), (7 kV, 9 kV) and (6 kV, 10 kV).

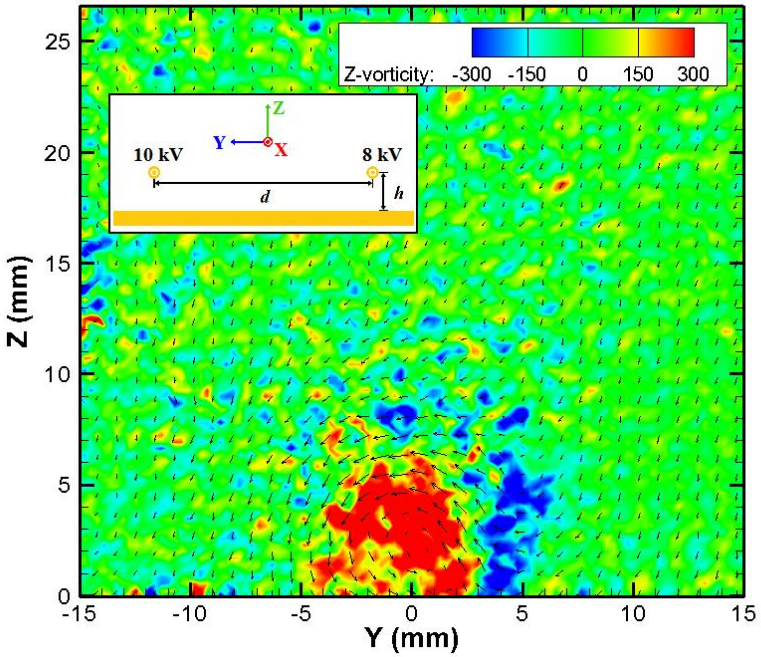

A

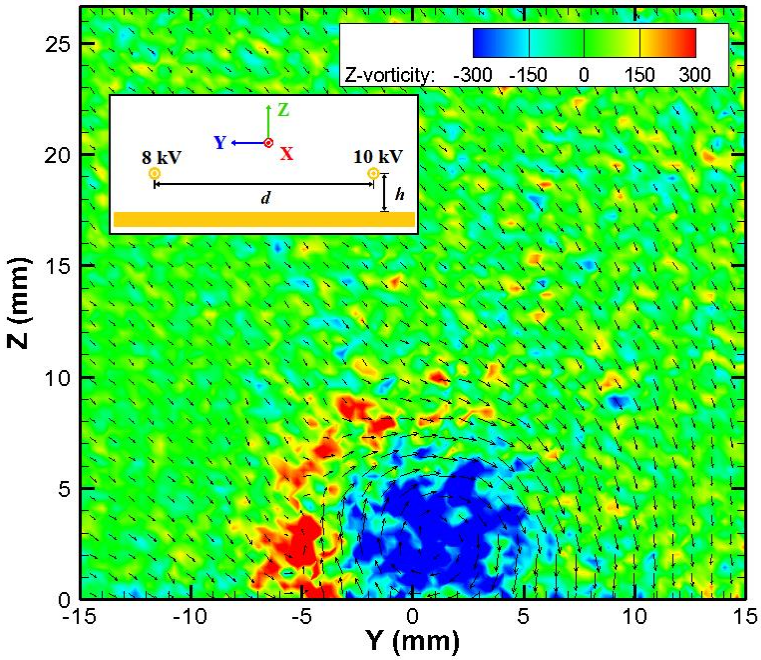

B

Figure 5-2. Controllable vortices generated by two-needle actuator at X = 10 mm. A) Anti-clockwise vortices. B) Clockwise vortices.

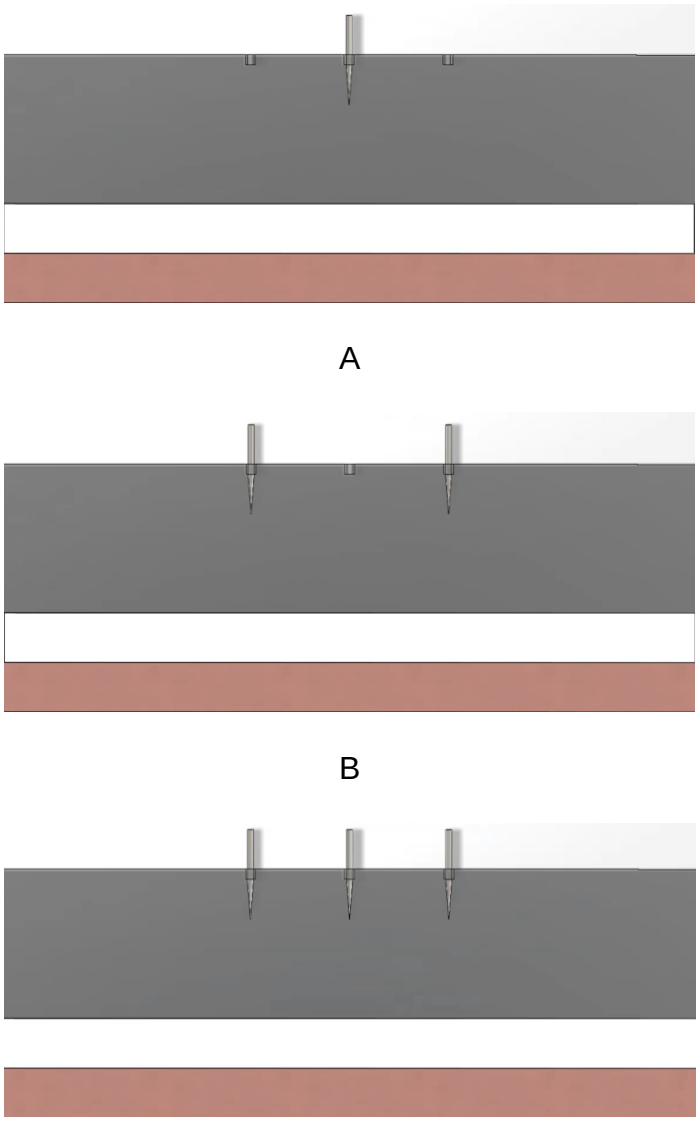

Figure 5-3. Needle configurations for number of needle test. A) Single needle case. B) Double needle case (separated by 20 mm). C) Tripe needle case (separated by 10 mm between adjacent needles).

5.3.2 Results and Discussion

Even with the same voltage magnitude, the two-needle actuator still generates vortices between the needles. The strength of the vortices is slight weaker than that generated by the different voltage actuator.

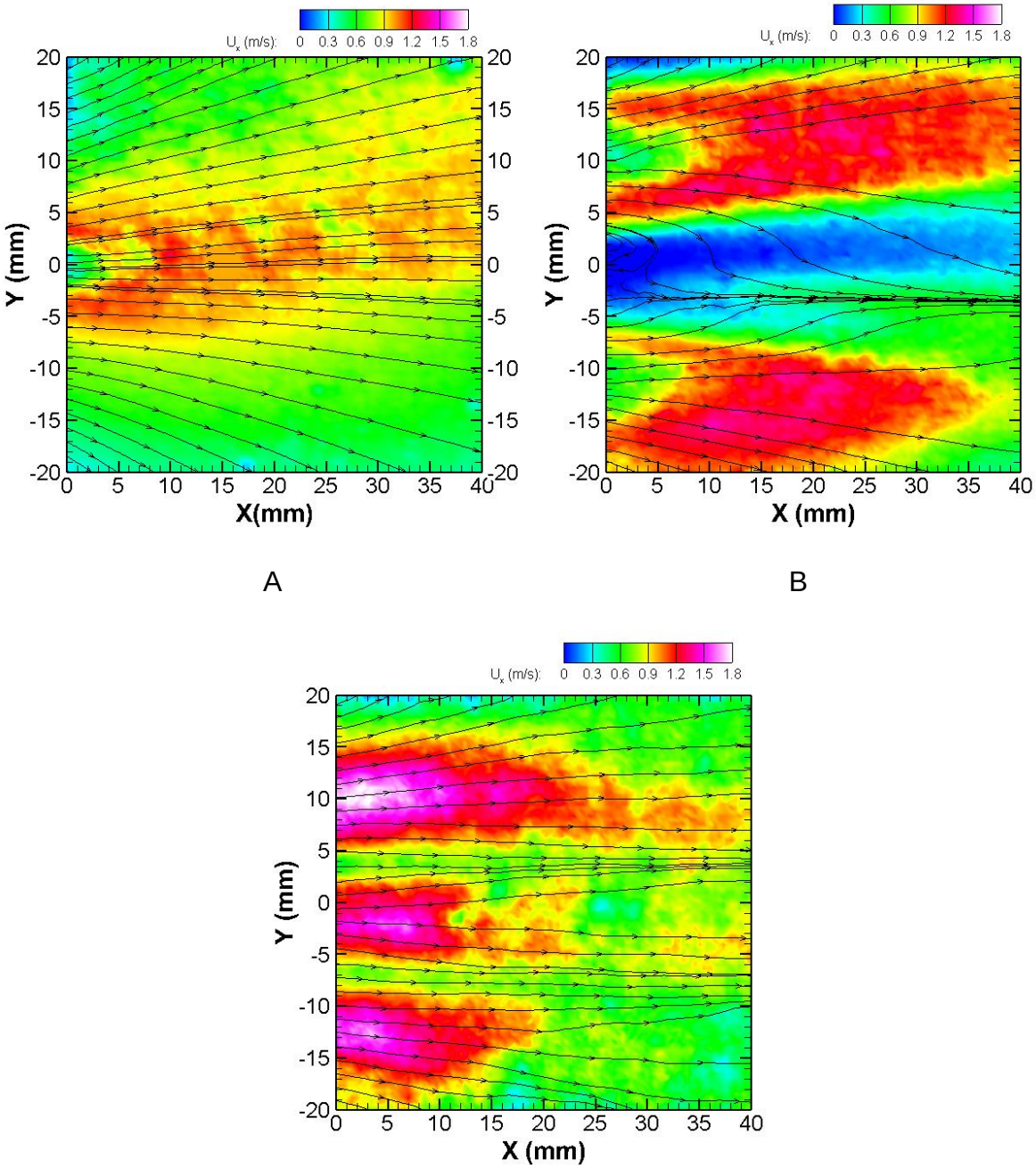

A B

C

Figure 5-4. XY-plane X direction velocity profile (Z = 2 mm) of needle actuators with different number of needles. A) Single needle. B) Double needle. C) Triple needle.

Figure 5-4 and Figure 5-5 display the X-direction velocity profile within an XY-plane 2 mm above the heater surface. In all three cases, needle actuators were operate

with positive 12 kV DC signal. The maximum velocity increases when number of needles increases. For double needle actuator, the area between two needles shows almost zero velocity, which indicates that the vortices was formed. However, without downstream velocity, air circulating in this region was heated by the heater below. Thus, no significant is observed in the area between the needles. On the other hand, triple needle actuators shows nearly uniform velocity distribution over the heater area. Hump effect can be observed on the velocity profiles of single needle and double needle actuators. Meanwhile, triple needle actuator shows strong air flow without hump effect.

As shown in Figure 5-6, cooling effects are represented by local convection enhancement factor distribution for number of needles study. Similar as the velocity profiles, with increasing number of needles, the cooling effect of the needle actuator becomes stronger. Hump effect shows negative influence on the cooling performance of single needle and double needle actuators. Meanwhile, strong uniform cooling effect was observed in triple needle case. One possible reason for this phenomenon is that with needle closer to each other, body forces generated by the needle array cannot propagate to the side direction, which allows more ambient cool air to go through the hot surface.

Average heat convection enhancement factors are also plotted in Figure 5-7. With increasing number of needles on the actuator, better cooling performance was observed.

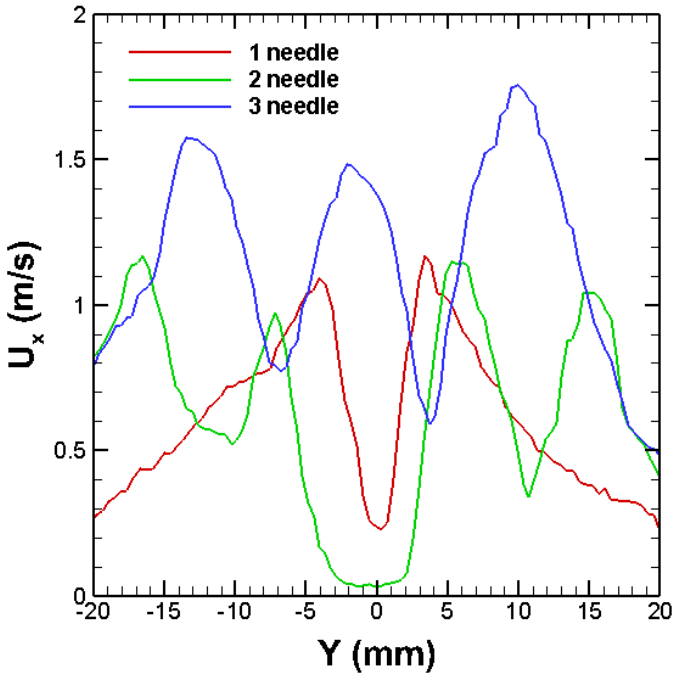

A

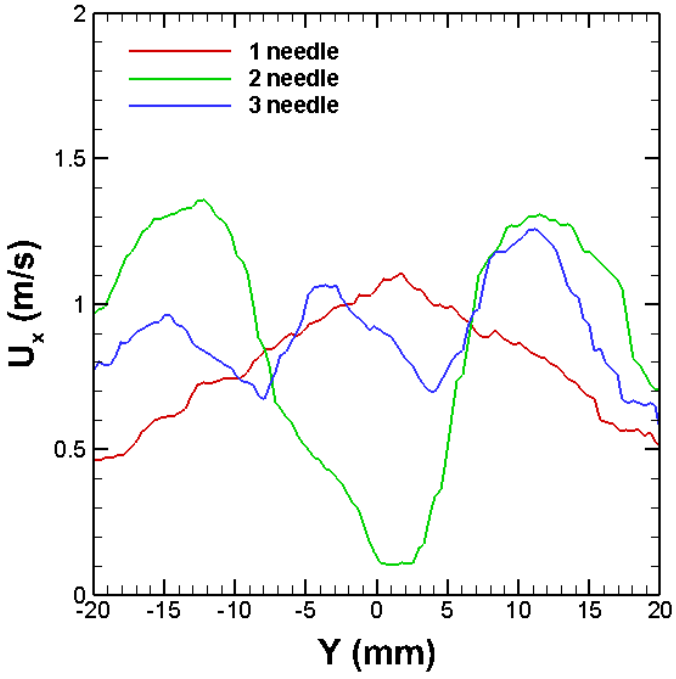

B

Figure 5-5. X direction Velocity profile with Positive DC signal powered on different number of needles. A) At the edge of the rubber heater (X = 20 mm). B) At middle of the rubber heater (X = 40 mm).

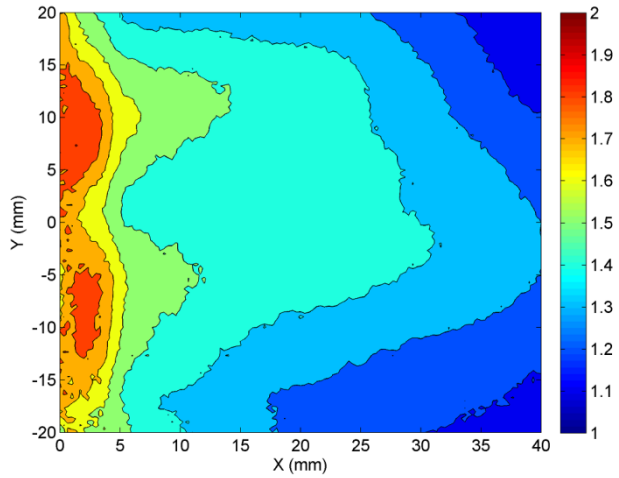

A

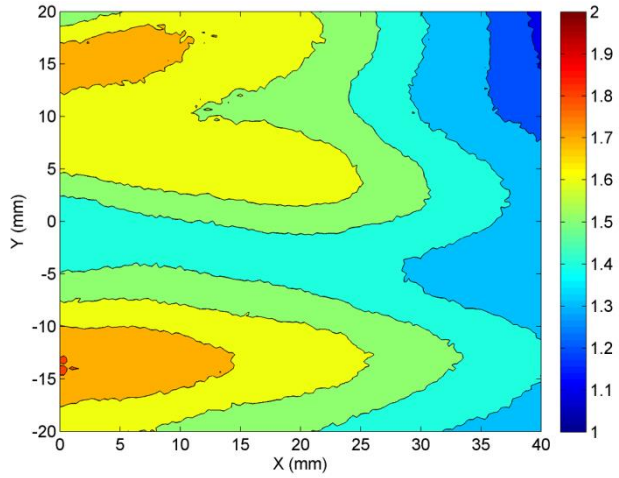

B

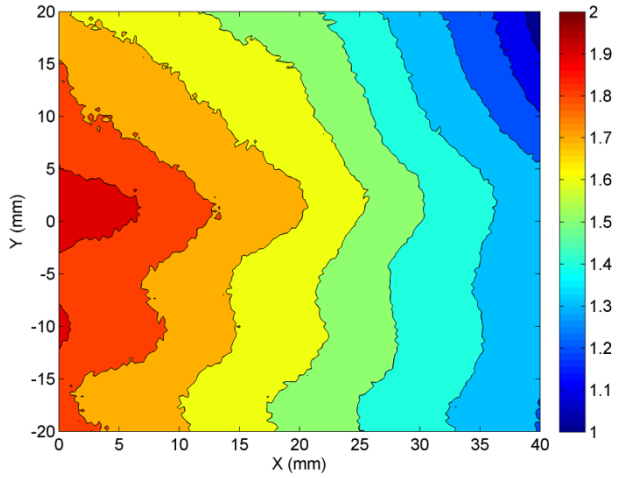

C

Figure 5-6. Distribution of the enhancement factor of the local heat convection coefficient over the rubber heater at 10kV with different number of needles. A) Single needle. B) Double needle. C) Triple needle.

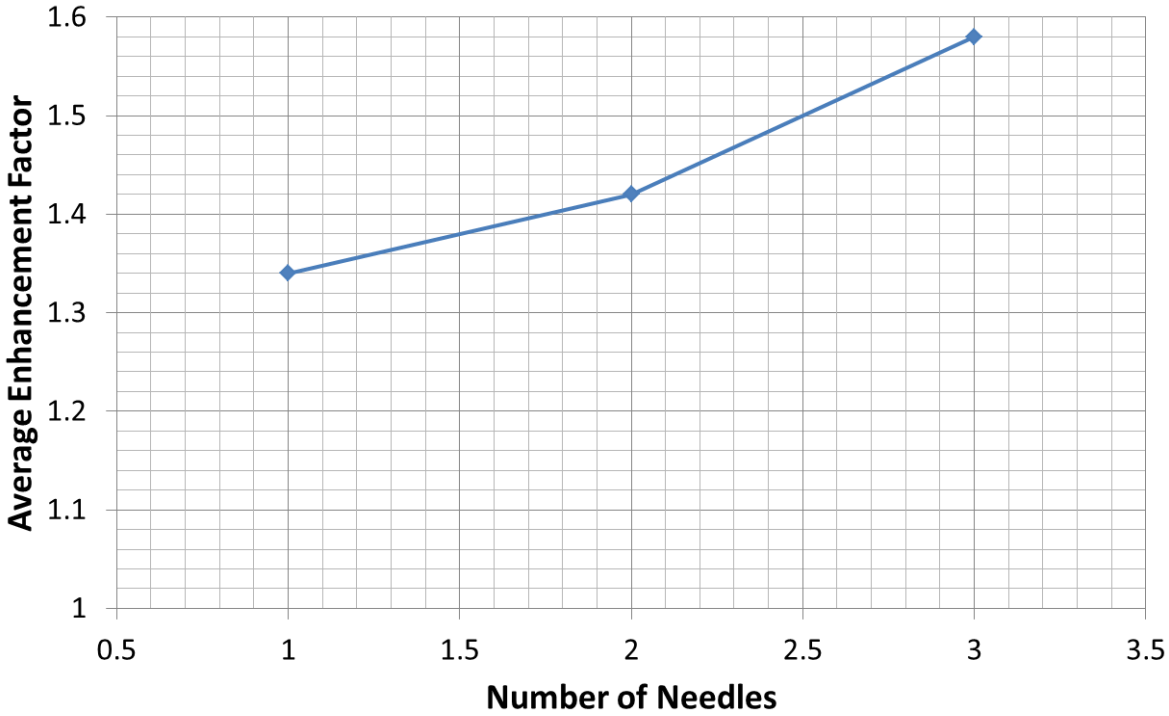

Figure 5-7. Average heat convection enhancement factor as a function of number of needles.

5.4 Summary of Vortices Generation Study

The vortex generation using multi-needle plate configuration was investigated. Controllable vortices generated between 2 needles with different voltage were demonstrated in this preliminary study. Based on these studies, this kind of low power actuation devices show great potential to be developed for many prospective applications.

Vortices with controllable rotation direction were generated by a two-needle actuator with different high voltage DC signal applied on two needles. Even with the same voltage magnitude, the two-needle actuator still generates vortices in between needles. The strength of the vortices is slight weaker than that generated by the different voltage actuator.

With increasing number of needles, the cooling effect of the needle actuator becomes stronger. Hump effect gives negative influence on the cooling performance of single needle and double needle actuators. And, the vortices generated by the double needle actuator circulate the hot air on the surface area between needles, which also reduces the cooling performance. Meanwhile, triple needle actuator generates a strong uniform flow, which achieves the best cooling performance in this work.

CHAPTER 6
SUMMARY AND FUTURE WORK

As mentioned in Chapter 2, plasma actuators have been applied to various aerodynamic and thermostatic applications and show great potential in these fields. In order to meet the needs of the “real world” applications, however, a huge increase on electro-mechanical energy conversion efficiency as well as a reduction in joule heating generation is necessary. To accomplish this, the development of plasma actuator needs a significant improvement in its performance. The objective of this work was to explore and characterize novel plasma actuators in an effort to improve the performance. Results of this work including development and characterization of the novel efficient plasma actuator, cooling performance and controllable vortex generation using the newly developed actuators were presented in the previous chapters. The following sections highlight and summarize the primary findings of these investigations, as well as provide recommendations for future work in these areas.

6.1 Development on Efficient Plasma Actuators

As shown in Chapter 3, development and characterization on novel efficient plasma actuators indicates significant improvement in energy conversion efficiency as well as reduction in heat generation. Newly designed actuator uses corona discharge with volumetric geometry. Air flow jet can be induced by the discharge and the electric field generated between the needle and grounded flat electrode. Highlights of this topic are list below.

1. Air flow jet driven by a single needle actuator can cover 2 cm range in span-wise direction (Y axis) with a strong core flow jet. Its electro-mechanical energy conversion efficiency can reach up to 2.8 %, almost equal to 30 times that of standard DBD channel or 4 times that of wire DBD channel. Strong entrainment effect was also observed during the study.

2. For the channel configuration, momentum was directly injected by the needle-to-plate electrodes configuration into the bulk airflow of the channel minimizing the viscous penalty from wall shear stress. Both positive and negative high voltage DC signals were used to generate strong ionic flow in the same direction.

3. Positive ionic flow with a stronger peak near the center causes less viscous penalty than negative ionic flow adhering to the plate electrodes resulting in higher energy conversion efficiency for positive signal.

These highlights show that this novel plasma actuator accomplish the original goal of the work. Furthermore the small size and easy implementation also indicate that this kind of actuator has great potential for wide range of applications in thermal and fluid areas. However, energy conversion efficiency of 2.8 % is not huge enough number to fully satisfy the “real world”, further research on improving the plasma actuator efficiency is advised.

6.2 Surface Cooling Performance Study

As shown in Chapter 4, newly developed plasma actuator was used for surface cooling over a semi-insulated rubber heater simulating the heat generation CPU chip. Glauert wall jet generated by the needle actuator enhances the heat convection process near the hot surface. Various parameters such as the location of needle, radius of curvature of the needle tip and voltage and polarity of the high voltage DC signal were studied. Both thermocouples and IR camera were employed to measure the surface temperature. PIV system was also used to capture the flow field over the hot surface. Flow field and surface temperature distribution were combined together to analyze the cooling performance of the actuator. Highlights of this topic are listed below.

4. The study on cooling effects shows that needle actuation device can reduce the temperature of a hot surface area by 15 ℃ using only mW energy within 80 s.

5. Voltage magnitude and polarity study suggests that the needle actuator can generates higher flow velocity with higher magnitude of voltage. Subsequently, the cooling performance is better with higher magnitude of voltage. With the

same voltage magnitude, actuator with negative signal showed slight better cooling performance as well as twice of the power consumption.

6. Height of a single needle in the actuator was varied from 2 mm to 12 mm above the heated surface. Result suggests when needle is placed at 6 mm, the cooling effects of the actuator reaches maximum for voltage from 6 kV to 10 kV. In the cases that needle placed in higher or lower locations, flow velocity was limited by the geometry.

7. Radius of curvature of needle tip was tested with 3 different size of the needle from 25 μm to 60 μm. Result indicates smaller radius of curvature leads to stronger cooling effect as well as the power consumption.

These highlights give us a brief understanding of how the needle actuators perform when applying them on surface cooling. With appropriate location and smaller radius of curvature of the needle electrode, the actuator can reach optimal condition for surface cooling.

6.3 Vortices Generation and Applications

As shown in Chapter 5, controllable vortices generated between 2 needles with different voltage were also demonstrated in the study. Due to the asymmetric assigned high voltage DC signal, body forces generated by two needles stir the flow in between and then create controllable vortices along with the streamline. With the controllable vortices, this technology can be applied to many aerodynamic problems. Furthermore, these vortices will increase the mixture of the flow. Thus, it may also be used in surface cooling applications. In this section, two parameters were investigated: number of needles used in the actuation device and voltage difference between 2 needles. Highlights with this topic are listed below.

8. Vortices with controllable rotation direction were generated by a two-needle actuator with different high voltage DC signal applied on two needles.

9. Even with the same voltage magnitude, the two-needle actuator still generates vortices in between needles. The strength of the vortices is slight weaker than that generated by the different voltage actuator.

10. With increasing number of needles, the cooling effect of the needle actuator becomes stronger.

11. The vertices generated by two-needle actuator don't move downstream as fast as the air jet. Thus, the heat convection enhancement is weaker between the needles in this case. However, three-needle actuator shows uniform heat convection enhancement over the hot surface.

6.4 Future Work

In this study, efficient needle corona plasma actuators have been designed and tested. Such actuators have great potential for many applications such as active flow control, gas mixture, enhanced surface cooling and so on. Potential future work after this study includes:

1. Parameter of plasma can be measured to further understand the status of the plasma. Thus, this information can be used to optimize the performance of actuators.

2. Applying this kind of actuator on applications such as flow control or gas mixture.

3. A compact high voltage low power DC supply can be designed to develop useful products with the actuators.

APPENDIX
PIV UNCERTAINTY ANALYSIS

In recent years, PIV is a noninvasive quantitative flow visualization tool that can give researchers spatiotemporal velocity field associated with complex flows. Through the use of a high speed camera, micro-sized flow seeding can be captured in a series of images. Generally, these images are captured in pairs. Since the time gap between each pair is set by the researcher, only the displacement of the flow seeding is calculated from the image pairs. To find the displacement of the seeding, standard cross-correlation or auto-correlation method is employed. According the method of PIV described above, the main error sources of PIV comes from the seeding in the flow and the algorism in PIV software.

The main concern with flow seeding is whether the seeding particle can accurately capture the fluid dynamics without altering the fluid properties. The non-dimensional Stokes number can be used to estimate the accuracy in which a seeding particle follows the flow. The Stokes number is defined as

$$\mathrm{St} = \frac{\tau_{part} u_{ref}}{L_{ref}}, \tag{A-1}$$

where τ_{part} is the relaxation time of the particle in the flow, u_{ref} is the characteristic reference velocity (typically the freestream velocity), and L_{ref} is the characteristic reference length. A Stokes number $\geqslant 1$ indicates the particle will not fellow the flow accurately or even change the flow. Meanwhile a Stokes number approaching zero ($\mathrm{St} \ll 1$) implies a perfect seeding for tracking the flow. For a constant accelerating Stokes flow, the seeding particle relaxation time is defined as

$$\tau_{part} = \frac{\rho_{part} d_{part}^2}{18 \mu_{fluid}}, \quad \text{(A-2)}$$

where ρ_{part} is the particle density, d_{part} is the particle's diameter and μ_{fluid} is the the dynamic viscosity of the fluid. Generally, the dynamics of a suspended particle in a flow are much more complicated (see Adrian, (1997)). But, Equation A-2 provides a reasonable estimation of the particles' response.

For the experiment setup used in this work, vaporized Ondina oil (Shell 917) was used as the sending particles to fill the test chamber. The oil was vaporized using a TSI atomizer (Model 9302). When the atomizer is pressurized at 25 psi, it can produce a droplet with a mean diameter of ~0.8 μm ($d_{part} \approx$ 0.8 μm) (TSI, 2000). Since air was the working fluid, the particle's diameter was substituted into Equation A-2 (along with ρ_{part} = 854 kg/m^3, and μ_{fluid} = 1.846E-5 kg/m-s) gives a relaxation time of 1.64E-6 s. Substituting the characteristic velocity of 3 m/s and a reference length of 1 mm into Equation A-2 gives Stokes number of 4.9E-3. This Stokes number can be treated as St $\ll$ 1. Thus, the error from seeding in the flow can be neglected under such a small Stokes number.

The other major error source comes from the algorism in the software used. In this experiment, DaVis 7.2 software was used to capture the image pairs from high speed camera and to post-process the acquired data. To resolve the error from the PIV algorism, an uncertainty analysis is proposed by (Timmins, Wilson, Smith, & Vlachos, 2012) and (Wilson & Smith, 2013b). They estimated the PIV algorism uncertainties by examining the distribution of errors from many measurements that have identical inputs. In keeping with ASME recommendations, 95 % confidence intervals were used on all uncertainties (ASME 2009).

For simplicity and clarity, a 1D equation for calculating the velocity in PIV measurements is used to begin the analysis. The velocity is calculated from the approximation that

$$u = \frac{dx}{dt} \approx \frac{\Delta x}{\Delta t}. \tag{A-3}$$

Thus, the uncertainty of *u* will come from both the displacement *Δx* and the time gap *Δt*. Assuming that the uncertainty of *Δx* and *Δt* is not correlated, the Taylor series method can be used for uncertainty propagation. Then, the total uncertainty for the velocity can be estimated as

$$U_u = \sqrt{\left(\frac{\partial u}{\partial \Delta x} U_{\Delta x}\right)^2 + \left(\frac{\partial u}{\partial \Delta t} U_{\Delta t}\right)^2}, \tag{A-4}$$

where $U_{\Delta x}$ and $U_{\Delta t}$ are the uncertainty estimates of *Δx* and *Δt*. Since the time gap Δt, which is in the range of several hundred micro-second, is controlled by hardware with nano-second accuracy (2.6 GHz CPU). The uncertainty of *Δt* can be assumed negligible. Thus the uncertainty of *u* becomes proportional to the computed displacement uncertainty, $U_{\Delta t}$. Equation A-4 simplifies to

$$U_u = \left(\frac{1}{\Delta t}\right) U_{\Delta x}. \tag{A-5}$$

Thus, for all the calculation below, velocity can be replaced by displacement for simplicity.

There are several major parameters that influence the accuracy of PIV, including particle image density, particle image diameter, particle displacement, and velocity gradient (also can be called shear). Thus, for every experimental set up, the uncertainty of *Δx* needs to be estimated with the specific parameters mentioned above.

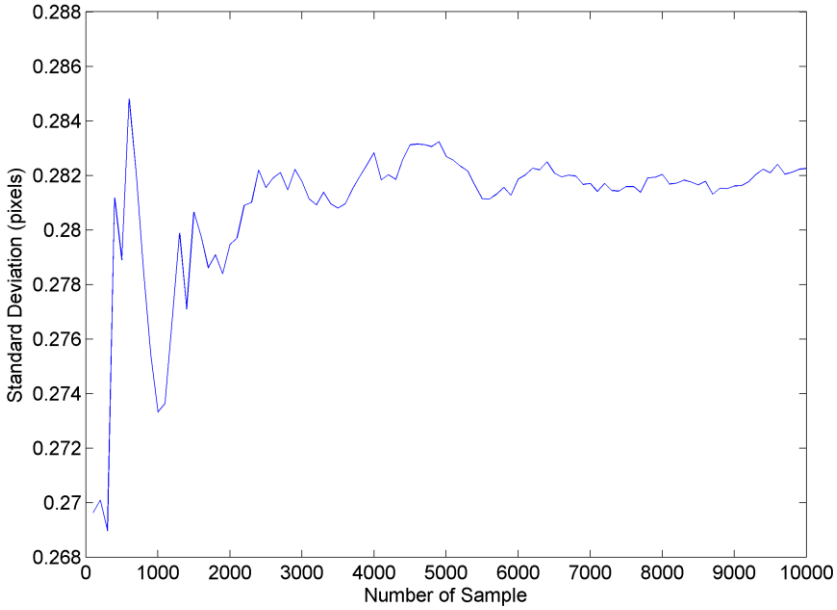

Figure A-1. Standard deviation as a function of the number of samples used.

In order to accurately estimate the uncertainty of the PIV setup used in this work, a pressurized air flow was measured by both the PIV setup and an OMEGA HH-USD hot wire anemometer. The uncertainty of this anemometer is 5 %. The time varying velocity obtained from hot wire anemometer is used to estimate the instantaneous bias, b_{ui}, of the mean velocity measured from PIV. Then the uncertainty on the mean velocity measured by PIV is (Wilson & Smith, 2013a)

$$U_{\bar{u}} = \sqrt{\left[\frac{1}{N}\sum_{i=1}^{N} b_{ui}\right]^2 + p_{\bar{u}^2}}, \tag{A-6}$$

where $p_{\bar{u}^2}$ is the precision uncertainty on the mean value calculated from sample standard deviation, N is total number of measurement obtained in each cases. Sample standard deviation was calculated from the measured data for the specific parameters

mentioned above. The number of data to be used was determined after a convergence study was performed. Figure A-1 displays the results. It suggests that 10000 samples for each case were sufficient for statistical convergence on standard deviation, s_u. Then the precision uncertainty on the mean value can be expressed as

$$p_{\bar{u}^2} = \frac{t^2_{95\,\%,\ N} s_u^2}{N}. \tag{A-7}$$

Table A-1 shows the calculated uncertainty with the same parameters used in this experimental work. For different velocity, time gap, Δt, was changed to maintained to render the same particle displacement. And 0.1 pixels/pixel is the maximum gradient found in the results. Thus, Table A-1 covers all the possible regions of the uncertainty surface defined by particle image density, particle image diameter, particle displacement, and velocity gradient. Total uncertainty shown in percentage including the hot wire anemometer uncertainty and PIV uncertainty.

Table A-1. Mean PIV velocity uncertainty for specific parameters used in this work.

Particle Diameter (pixels)	Particle Density (part/pixel^2)	Displacement (pixels)	Gradient (pixels/pixel)	Time Gap (μs)	Total Uncertainty
2.1	0.048	3.2	0.0	250	6.1 %
2.1	0.048	2.5	0.1	250	13.5 %
2.1	0.052	3.0	0.0	80	5.5 %
2.1	0.052	2.4	0.1	80	12.7 %

LIST OF REFERENCES

Adrian, R. J. (1997). Dynamic ranges of velocity and spatial resolution of particle image velocimetry. [Article]. *Measurement Science & Technology, 8*(12), 1393-1398.

Artana, G., D'Adamo, J., Leger, L., Moreau, E., & Touchard, G. (2002). Flow control with electrohydrodynamic actuators. [Article]. *Aiaa Journal, 40*(9), 1773-1779.

Asano, K., Hishinuma, R., & Yatsuzuka, K. (2000, 2000). *Bipolar corona discharge from a floating filamentary particle between parallel plate electrodes.* Paper presented at the Industry Applications Conference, 2000. Conference Record of the 2000 IEEE.

Braithwaite, N. S. J. (2000). Introduction to gas discharges. [Article]. *Plasma Sources Science & Technology, 9*(4), 517-527.

Campbell, N. S., & Roy, S. (2014). Plasma channel flows: Electro-fluid dynamic jets. [Article]. *Applied Physics Letters, 105*(13), 4.

Chang, J. S., Lawless, P. A., & Yamamoto, T. (1991). CORONA DISCHARGE PROCESSES. [Article]. *Ieee Transactions on Plasma Science, 19*(6), 1152-1166.

Chen, I. Y., Guo, M. Z., Yang, K. S., & Wang, C. C. (2013). Enhanced cooling for LED lighting using ionic wind. [Article]. *International Journal of Heat and Mass Transfer, 57*(1), 285-291.

Colas, D. F., Ferret, A., Pai, D. Z., Lacoste, D. A., & Laux, C. O. (2010). Ionic wind generation by a wire-cylinder-plate corona discharge in air at atmospheric pressure. [Article]. *Journal of Applied Physics, 108*(10), 6.

Conrads, H., & Schmidt, M. (2000). Plasma generation and plasma sources. [Article]. *Plasma Sources Science & Technology, 9*(4), 441-454.

Corke, T. C., Enloe, C. L., & Wilkinson, S. P. (2010). Dielectric Barrier Discharge Plasma Actuators for Flow Control *Annual Review of Fluid Mechanics* (Vol. 42, pp. 505-529). Palo Alto: Annual Reviews.

Drews, A. M., Cademartiri, L., Whitesides, G. M., & Bishop, K. J. M. (2013). Electric winds driven by time oscillating corona discharges. [Article]. *Journal of Applied Physics, 114*(14), 7.

Durscher, R., & Roy, S. (2012). Evaluation of thrust measurement techniques for dielectric barrier discharge actuators. [Article]. *Experiments in Fluids, 53*(4), 1165-1176.

Durscher, R., Stanfield, S., & Roy, S. (2012). Characterization and manipulation of the "saturation" effect by changing the surface temperature of a dielectric barrier discharge actuator. [Article]. *Applied Physics Letters, 101*(25), 4.

Durscher, R. J., & Roy, S. (2012). Three-dimensional flow measurements induced from serpentine plasma actuators in quiescent air. [Article]. *Journal of Physics D-Applied Physics, 45*(3), 9.

Fridman, A., Chirokov, A., & Gutsol, A. (2005). Non-thermal atmospheric pressure discharges. [Review]. *Journal of Physics D-Applied Physics, 38*(2), R1-R24.

Fridman, A. A. (2008). *Plasma chemistry*. Cambridge: New York.

Go, D. B., Maturana, R. A., Fisher, T. S., & Garimella, S. V. (2008). Enhancement of external forced convection by ionic wind. [Article]. *International Journal of Heat and Mass Transfer, 51*(25-26), 6047-6053.

Goldman, M., & Sigmond, R. S. (1982). CORONA AND INSULATION. [Article]. *Ieee Transactions on Electrical Insulation, 17*(2), 90-105.

Griem, H. R. (1962). HIGH-DENSITY CORRECTIONS IN PLASMA SPECTROSCOPY. [Article]. *Physical Review, 128*(3), 997-&.

Hermstein, W. (1960). Die Stromfaden-Entladung und ihr Übergang in das Glimmen. *Archiv für Elektrotechnik, 45*(3), 209-224.

Howatson, A. M. (1976). *An Introduction to gas discharges* (2d ed.). Oxford: New York.

Jukes, T. N. (2007). *Turbulent drag reduction using surface plasma.* Unpublished Ph.D.; University of Nottingham.

Kalman, H., & Sher, E. (2001). Enhancement of heat transfer by means of a corona wind created by a wire electrode and confined wings assembly. [Article]. *Applied Thermal Engineering, 21*(3), 265-282.

Leger, L., Moreau, E., & Touchard, G. G. (2002). Effect of a DC corona electrical discharge on the airflow along a flat plate. [Article; Proceedings Paper]. *Ieee Transactions on Industry Applications, 38*(6), 1478-1485.

Leonov, S., Opaits, D., Miles, R., & Soloviev, V. (2010). Time-resolved measurements of plasma-induced momentum in air and nitrogen under dielectric barrier discharge actuation. [Article]. *Physics of Plasmas, 17*(11), 8.

McKinney, P. J., Davidson, J. H., & Leone, D. M. (1992). CURRENT DISTRIBUTIONS FOR BARBED PLATE-TO-PLANE CORONAS. [Article]. *Ieee Transactions on Industry Applications, 28*(6), 1424-1431.

Molki, M., & Bhamidipati, K. L. (2004). Enhancement of convective heat transfer in the developing region of circular tubes using corona wind. [Article]. *International Journal of Heat and Mass Transfer, 47*(19-20), 4301-4314.

Moreau, E. (2007). Airflow control by non-thermal plasma actuators. [Review]. *Journal of Physics D-Applied Physics, 40*(3), 605-636.

Moreau, E., Benard, N., Lan-Sun-Luk, J. D., & Chabriat, J. P. (2013). Electrohydrodynamic force produced by a wire-to-cylinder dc corona discharge in air at atmospheric pressure. [Article]. *Journal of Physics D-Applied Physics, 46*(47), 14.

National Aeronautics and Space Administration. (2003). Paints. Retrieved August 3, 2015, from http://masterweb.jpl.nasa.gov/reference/paints.htm

Raizer, I. P. (1991). Gas discharge physics Retrieved from WorldCat database Available from http://www.gbv.de/dms/bowker/toc/9780387534459.pdf Available from Materials specified: Table of contentshttp://www.gbv.de/dms/bowker/toc/9780387534459.pdf

Riherd, M., & Roy, S. (2012). Measurements and simulations of a channel flow powered by plasma actuators. [Article]. *Journal of Applied Physics, 112*(5), 9.

Riherd, M., & Roy, S. (2013). Serpentine geometry plasma actuators for flow control. [Article]. *Journal of Applied Physics, 114*(8), 13.

Rizzetta, D. P., & Visbal, M. R. (2010). Large-Eddy Simulation of Plasma-Based Turbulent Boundary-Layer Separation Control. [Article; Proceedings Paper]. *Aiaa Journal, 48*(12), 2793-2810.

Rizzetta, D. P., & Visbal, M. R. (2011). Numerical Investigation of Plasma-Based Control for Low-Reynolds-Number Airfoil Flows. [Article; Proceedings Paper]. *Aiaa Journal, 49*(2), 411-425.

Robinson, M. (1961). Movement of air in the electric wind of the corona discharge. *American Institute of Electrical Engineers, Part I: Communication and Electronics, Transactions of the, 80*(2), 143-150.

Robinson, M. (1962). A HISTORY OF ELECTRIC WIND. [Article]. *American Journal of Physics, 30*(5), 366-&.

Roth, J. R. (1995). *Industrial plasma engineering. Vol. 1*. Bristol: Institute of Physics Pub.

Roth, J. R. (2003). Aerodynamic flow acceleration using paraelectric and peristaltic electrohydrodynamic effects of a One Atmosphere Uniform Glow Discharge Plasma. [Article; Proceedings Paper]. *Physics of Plasmas, 10*(5), 2117-2126.

Roth, J. R., Sherman, D. M., & Wilkinson, S. P. (2000). Electrohydrodynamic flow control with a glow-discharge surface plasma. [Article; Proceedings Paper]. *Aiaa Journal, 38*(7), 1166-1172.

Santhanakrishnan, A., & Jacob, J. D. (2007). Flow control with plasma synthetic jet actuators. [Article]. *Journal of Physics D-Applied Physics, 40*(3), 637-651.

Schatzman, D. M., & Thomas, F. O. (2010). Turbulent Boundary-Layer Separation Control with Single Dielectric Barrier Discharge Plasma Actuators. [Article; Proceedings Paper]. *Aiaa Journal, 48*(8), 1620-1634.

Schutze, A., Jeong, J. Y., Babayan, S. E., Park, J., Selwyn, G. S., & Hicks, R. F. (1998). The atmospheric-pressure plasma jet: A review and comparison to other plasma sources. [Article]. *Ieee Transactions on Plasma Science, 26*(6), 1685-1694.

Sheu, W. J., Hsiao, J. J., & Wang, C. C. (2013). Effect of oscillatory EHD on the heat transfer performance of a flat plate. [Article]. *International Journal of Heat and Mass Transfer, 61*, 419-424.

Soetomo, F. (1992). *The influence of high voltage discharge on flat plate drag at low Reynolds number air flow.* Unpublished M.S.; Iowa State University.

Timmins, B. H., Wilson, B. W., Smith, B. L., & Vlachos, P. P. (2012). A method for automatic estimation of instantaneous local uncertainty in particle image velocimetry measurements. *Experiments in Fluids, 53*(4), 1133-1147.

Tirumala, R., Benard, N., Moreau, E., Fenot, M., Lalizel, G., & Dorignac, E. (2014). Temperature characterization of dielectric barrier discharge actuators: influence of electrical and geometric parameters. [Article]. *Journal of Physics D-Applied Physics, 47*(25), 12.

Toyota, H., Zama, S., Akamine, Y., Matsuoka, S., & Hidaka, K. (2002). Gaseous electrical discharge characteristics in air and nitrogen at cryogenic temperature. [Article]. *Ieee Transactions on Dielectrics and Electrical Insulation, 9*(6), 891-898.

Velkoff, H. R., & Godfrey, R. (1979). LOW-VELOCITY HEAT-TRANSFER TO A FLAT-PLATE IN THE PRESENCE OF A CORONA DISCHARGE IN AIR. [Article]. *Journal of Heat Transfer-Transactions of the Asme, 101*(1), 157-163.

Velkoff, H. R., & Ketcham, J. (1968). EFFECT OF AN ELECTROSTATIC FIELD ON BOUNDARY-LAYER TRANSITION. [Note]. *Aiaa Journal, 6*(7), 1381-&.

Visbal, M. R. (2010). Strategies for control of transitional and turbulent flows using plasma-based actuators. [Article]. *International Journal of Computational Fluid Dynamics, 24*(7), 237-258.

Wang, C. C., Durscher, R., & Roy, S. (2011). Three-dimensional effects of curved plasma actuators in quiescent air. [Article]. *Journal of Applied Physics, 109*(8), 9.

Wilson, B. M., & Smith, B. L. (2013a). Taylor-series and Monte-Carlo-method uncertainty estimation of the width of a probability distribution based on varying bias and random error. [Article]. *Measurement Science & Technology, 24*(3), 11.

Wilson, B. M., & Smith, B. L. (2013b). Uncertainty on PIV mean and fluctuating velocity due to bias and random errors. [Article]. *Measurement Science & Technology, 24*(3), 15.

Zebboudj, Y., & Ikene, R. (2000). Positive corona inception in HVDC configurations under variable air density and humidity conditions. [Article]. *European Physical Journal-Applied Physics, 10*(3), 211-218.

Zouzou, N., Moreau, E., & Touchard, G. (2006). Electrostatic precipitation in a point-plan configuration. [Article; Proceedings Paper]. *Journal of Electrostatics, 64*(7-9), 537-542.

BIOGRAPHICAL SKETCH

Pengfei Zhao was born in 1988 in the city of Xi'an, China. In 2010, he received his B.S. degree of applied physics from University of Science and Technology of China, Hefei, China. Then, he joined Applied Physics Research Group (APRG) in the Department of Mechanical and Aerospace Engineering at the University of Florida. His research interests include plasma physics, plasma actuator and flow control. He received his M.S. of aerospace engineering from the University of Florida in the spring of 2014. He also received his Ph.D. of aerospace engineering with a minor in statistics in the fall of 2015.